RUHR
UNIVERSITÄT
BOCHUM

RUB

Modellierung von Plasma–Wand–Wechselwirkungen

in einem quasineutralen Hybrid Modell zur Simulation von magnetisierten Plasmaentladungen

Modeling of plasma–wall interactions

in a quasi–neutral hybrid model for the simulation of magnetized plasma discharges

Masterarbeit

zur Erlangung des Grades eines
„Master of Science“
im Fach Phsyik

an der Fakultät für Physik und Astronomie
der Ruhr-Universität Bochum

von
Marc Fehling

geboren in
Lübbecke

Bochum, Sommersemester 2015

Zusammenfassung

Laborexperimente mit Plasmen sind zwangsläufig durch Wände begrenzt, die für das Verständnis des Verhaltens der erzeugten Plasmen eine große Rolle spielen. Eine übliche Methode zur Beschreibung des Plasma–Wand–Übergangs ist das Bohm Kriterium, welches in dieser Abschlussarbeit nachvollzogen und diskutiert wurde. Zur Simulation von Plasmen muss ein besonderer Schwerpunkt auf die Modellierung von Wänden gelegt werden, genauer gesagt auf den Bereich des Plasma–Wand–Übergangs. In diesem Sinne wurden verschiedene Algorithmen zur Forderung des Bohm Kriteriums vorgestellt. Hierbei wurde eine neue Möglichkeit zur Interpretation von Wänden als Ursache für stationäre Schocks dargelegt, welche aus Simulationen in einem quasineutralen Hybrid Modell motiviert war.

Das Hybrid Modell nimmt Elektronen als Fluid an, während es Ionen mit einer Particle–in–cell Methode behandelt und somit kinetische Effekte berücksichtigt. Zusätzlich wurden Stöße zwischen beiden Teilchensorten sowie konstante magnetische Felder einbezogen. Simulationen wurden in einem eindimensionalen Modell durchgeführt, in dem das Gebiet durch zwei vollständig absorbierende Wände begrenzt war. Es wurden stationäre Zustände betrachtet, in denen Ionisationsquellen die Verluste an den Wänden ausglichen. Hierbei wurde das elektrische Feld als wirbelfrei festgesetzt.

Die Ergebnisse aus der Simulation wurden mit jenen aus einem entsprechenden Zwei–Fluid Modell verglichen. Dabei waren Unterschiede erkennbar, besonders wenn Ionisation aus einem ruhenden Neutralgas oder schwach magnetisierte Plasmen angenommen wurden, die für einen Anstieg der Ionentemperatur beziehungsweise Anisotropie–Effekte verantwortlich waren. Daher müssen kinetische Effekte für diese speziellen Fälle berücksichtigt werden.

Abstract

Laboratory experiments with plasmas are inevitably limited by walls, which play a major role in the comprehension of the plasma's characteristics. A common way to describe the plasma–wall transition is the Bohm criterion, which was recalled and discussed in this thesis. To simulate plasmas, special emphasis needs to be placed on the modeling of walls, or, to be more precise, on the plasma–wall transition. In this context, different algorithms assuring the fulfillment of the Bohm criterion were presented. Here, a new interpretation of walls as the cause for stationary shocks was introduced, motivated by simulations in a quasi–neutral hybrid model.

The hybrid model assumes the electrons as a fluid while treating the ions with a particle–in–cell method, thus respecting kinetic effects. Additionally, collisions between the two species as well as constant magnetic fields were taken into account. Simulations were carried out in a one–dimensional model, in which the domain was limited by totally absorbing walls on each side. Stationary states were considered, in which ionization sources balance wall losses. Here, the electric field was enforced to be irrotational.

The simulation results were compared with those of a corresponding two–fluid model. Differences between them were observable, especially when ionization from a resting neutral gas or weakly magnetized plasmas were considered, causing an increase of ion temperature and anisotropy effects, respectively. Hence kinetic effects need to be considered in these particular cases.

Contents

List of Tables

List of Figures

Chapter 1

Introduction

The plasma state is the most wide–spread naturally occurring state of visible matter in the universe. Artificially produced plasmas also find broad application in human activities, which are most commonly produced in spatially limited vessels so that the understanding of plasma–wall–interactions and the build–up of sheaths due to the plasma's shielding capability is crucial for the comprehension of the whole system. To investigate this topic in the electrostatic case, the pioneer work of Bohm [Boh49], which is reviewed in detail by Riemann [Rie91], is still the reference today, which will be retraced and discussed in the following chapter.

Considering magnetic fields, various approaches concerning plasma–wall-interactions have been elaborated. Such models are presented for example by Behnel [Beh84], Chodura [Cho82] [Cho85] [Cho88], Holland et al. [HFM93], and Riemann [Rie94]. Behnel provided a kinetic model, where ion transport across a magnetic field parallel to the wall is considered by charge exchange collisions with neutrals. He supplemented his investigations with an ion fluid model, in which the ion flux on the wall is set constant and the densities of ions and electrons are assumed to be in a Boltzmann equilibrium, respectively. Chodura investigated the plasma–wall transition layer with a particle–in–cell method for both ions and electrons without collisions in an arbitrary magnetic field. He found that the resulting profiles are only starting smoothly if the instreaming plasma exceeds a certain limit, leading to a generalization of the Bohm criterion in this specific case. Riemann also considered an arbitrary magnetic field. He treated ions as a fluid with ion–neutral collisions while assuming the electrons to be in a Boltzmann equilibrium. Riemann stated that the previous work of Behnel and Chodura are both special cases of his considerations: A magnetic field parallel to the wall resembles Behnel's model, whereas the absence of collisions mirrors the one of Chodura. Holland et al. assumed ions with a

Maxwell–Boltzmann velocity distribution, considered electrons as a fluid with electron-neutral collisions and carried out investigations on solving Poisson's equation at a constant magnetic field in arbitrary direction. They came to the conclusion that the transition properties are determined by the relation of the impact angle α of the magnetic field on the wall and the ratio of electron–neutral collision frequency and the electron gyro frequency ν_{e0}/Ω_e. If $\alpha \lesssim \nu_{e0}/\Omega_e$ applies, it additionally depends on the ratio of the convective and the diffusive electron flow. In this thesis, an alternative interpretation of the plasma–wall transition with jump conditions will be presented, which is applicable to both cases with and without magnetic fields.

To examine plasma–wall interactions in this thesis, basic investigations are carried out employing a one–dimensional model, in which the domain is limited by totally absorbing walls. It additionally accounts for electron–ion collisions and is supplemented by an ionization model, so that a stationary state is reachable.

To investigate plasma–wall–interactions in this thesis, simulations will be performed in a quasi–neutral hybrid model that treats ions with a particle–in–cell (PIC) method and electrons as a background fluid, so that kinetic effects caused by the ions will be represented as well. The hybrid model has been validated in the PlaCeBo (**Pla**sma **C**od**e** **Bo**chum) framework in the foregoing Bachelor thesis [Feh13]. To review the simulation results, a two–fluid model based on the work of Alterkop et al. [AGB05] is pursued, who considered electron–ion collisions and a constant magnetic field parallel to both walls. They came to the conclusion that the ions are accelerated to sound velocity in a layer of thickness $\sim r_i/\beta$ right before the walls, where r_i is the ion gyro radius at sound velocity and β the Hall parameter.

The original motivation of this thesis lies in the PSI–2 experiment and its plasma generator, which is similar to the so–called hollow cathode discharge that has been investigated in detail by Ferreira & Delcroix [FD78]. The experiment will be presented in more detail in the end of this chapter.

1.1 PlaCeBo code

For further interpretation of the FlareLab–experiment, the PlaCeBo framework has been developed at the local institute for theoretical physics I (TP1). PlaCeBo currently contains implementations of a PIC method as well as ideal magnetohydrodynamics (MHD) and hybrid models. FlareLab is designed to generate magnetic flux tubes with the aim to gain further knowledge about the magnetic activity on solar surfaces [FL].

Each of the three submodules (PIC, Hybrid and MHD) was initially developed with the motivation of simulating one specific phase of the FlareLab experiment. The PIC method is dedicated to the inital phase of the experiment, in which particle densities of ions and electrons are small enough to expect kinetic effects. On the other hand, the MHD part describes the stage where both particle species can be considered as a fluid. The hybrid model is used to close the gap between both phases, namely when electrons already behave like a fluid, but ion Larmor radii are still large enough to expect kinetic effects.

The PIC code is based on the one presented by Birdsall & Langdon in which particle evolution is handled with the algortihm of Boris [BL85]. The MHD part utilizes a finite–volume method with central weighted essentially nonoscillatory (CWENO) reconstruction as elaborated by Kurganov & Levy [KL00]. For the hybrid code, the current advance method (CAM) by Matthews [Mat94] is the inspiration for the time evolution of quantities. Here, the ions are treated by the above mentioned PIC method.

1.2 PSI–2 experiment

The linear plasma device PSI–2 has been established to investigate low temperature plasmas like those occurring in the divertor region of tokamak experiments. A drawing of its setup is provided in Fig. 1.2. In the experiment a plasma is generated by a low–pressure high–current arc discharge between a heated cathode and an anode, both cylindrical in shape. In the following, this region is referred to as the anode–cathode space. The generated plasma then propagates to the target chamber in which it strikes the eponymous, yet optional, target, so that material investigations can be carried out. On the way to the target, the plasma is confined by an axial magnetic field and passes several pumping stages. [NFM98] [PSI]

The original PSI–1 experiment was operated firstly in 1991 at the Humboldt university of Berlin by the Max Planck institute for plasma physics in Garching. In 1998, the target chamber has been enlarged and was provided with additional coils, which is why it was called PSI–2 after these enhancements. The whole experiment was transfered to the Forschungszentrum Jülich in October 2009 and is operated there until today. [Kre11]

In Tab. 1.1, 1.2 and 1.3, various plasma parameters for the PSI–1 experiment are provided for different working gases and regions of the experiment. Since the anode–cathode space has not been changed at all during the upgrade, the parameters corresponding to this specific region are roughly the same for PSI–2. A detailed drawing of the anode–cathode space with an accurate representation of length, magnetic flux and its density is provided in Fig. 1.1. Since

ion Larmor radii are rather large compared to the radius of the plasma (H: $r_\mathrm{i}/R \approx 0.117$, Ar: $r_\mathrm{i}/R \approx 0.3$), kinetic effects induced by the ion gyro motion are supposed, which is why the hybrid model is predestined for the investigation of plasma–wall–interactions in this particular experiment.

A new experiment called JULE–PSI is scheduled to start working in Jülich in late 2016. The setup will base upon the experiences made with the PSI–2 device. It will be embedded in a hot cell, so that investigations can be extended on radioactive materials. The cathode of the plasma generator also will be changed from cylindrically shaped to planar. [PSI]

Table 1.1: Characteristics of the PSI–1 experiment. [NFM98]

Description	Value
External axial magnetic field	$B_0 = 0.1\,\mathrm{T}$
Maximal discharge current	$I_\mathrm{max} = 1\,000\,\mathrm{A}$
Plasma radius	$R = 0.03\,\mathrm{m}$

Table 1.2: Plasma parameters in the target exposition region of the PSI–1 experiment. [Mey98, Tab. 1.1]

Gas	n_e / m^{-3}	T_e / eV	T_i / eV
H2	$1.0 \cdot 10^{17}$ ... $4.0 \cdot 10^{18}$	2 ... 20	1 ... 10
D2	$1.0 \cdot 10^{17}$ ... $4.0 \cdot 10^{18}$	2 ... 20	1 ... 10
He	$2.0 \cdot 10^{17}$ ... $8.0 \cdot 10^{18}$	2 ... 25	2 ... 14
Ar	$1.0 \cdot 10^{18}$ ... $2.5 \cdot 10^{19}$	1 ... 5	0.4 ... 4

Table 1.3: Typical time and length scales in the anode–cathode region of the PSI–1 experiment. Here, τ are collision times between different species, λ_D is the Debye–length, λ_ion is the ion mean free path and r_i is the ion gyro radius. [Mey98, Tab. 1.5]

Gas	τ_ei / s	τ_0e / s	τ_0i / s	λ_D / m	λ_ion / m	r_i / m
H	$3.1 \cdot 10^{-7}$	$1.5 \cdot 10^{-7}$	$1.0 \cdot 10^{-5}$	$6.9 \cdot 10^{-6}$	0.12	0.0035
Ar	$4.2 \cdot 10^{-9}$	$3.1 \cdot 10^{-7}$	$1.9 \cdot 10^{-4}$	$6.8 \cdot 10^{-7}$	0.002	0.01

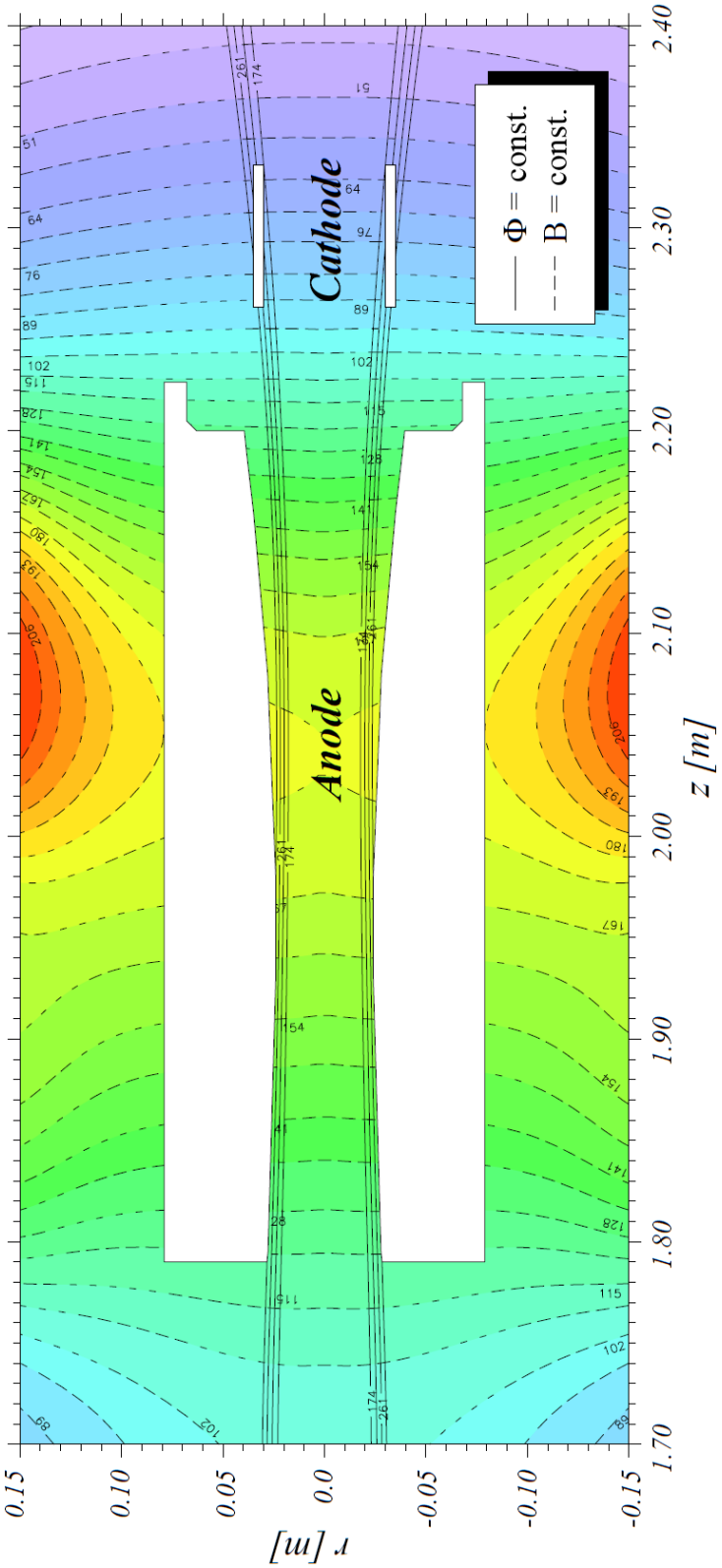

Figure 1.1: Contour plot of the magnetic flux density B in mT in the cathode–anode region of the PSI–1 experiment. Φ denotes the magnetic flux. [Mey98, Fig. 1.4, modified]

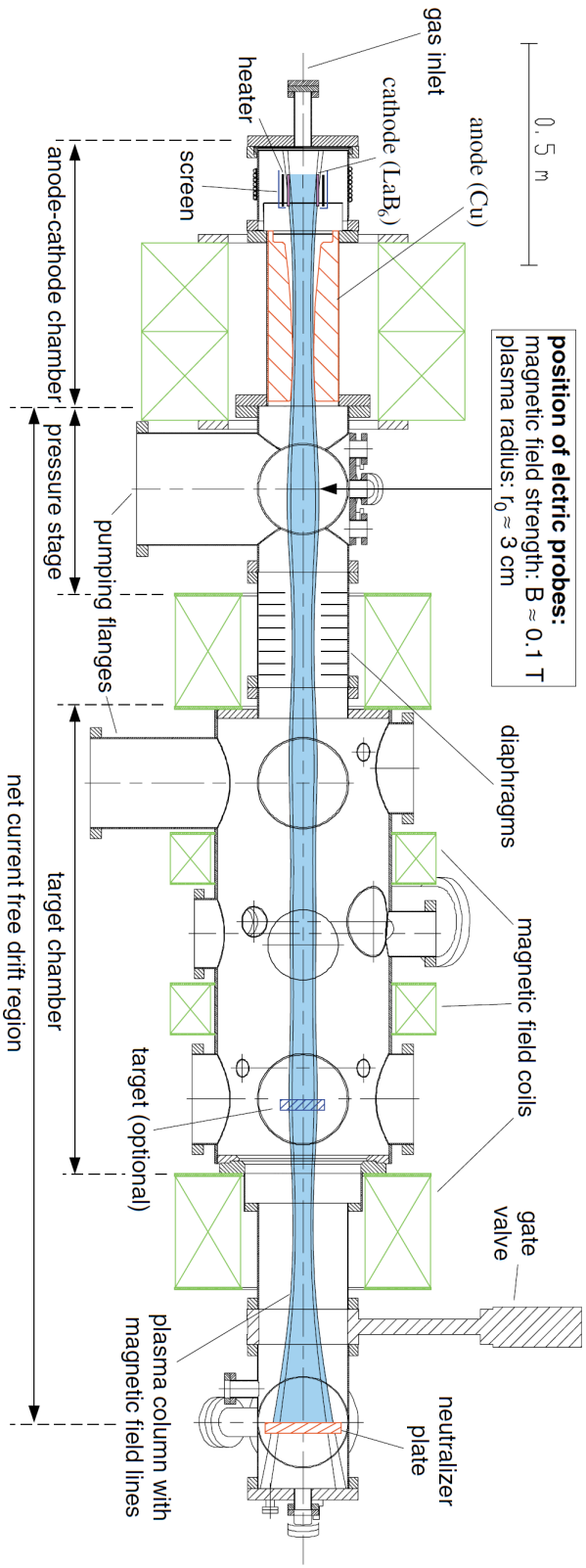

Figure 1.2: Sketch of the PSI–2 experiment. [KBL+01, Fig. 1]

Chapter 2

Basics of plasma sheaths

Plasmas tend to preserve a neutral and field–free state even under external influences. If an electrode or, more generally speaking, a wall is exposed to such a plasma, the plasma screens this disturbance by enveloping it in a sheath. The transition between plasma and wall is characterized by violation of the quasi–neutrality and occurs on a length scale of several Debye lengths λ_D [LL05]. Bohm provides an attempt to explain the sheath occurrence theoretically. He states that the ions passing this sheath border need to exceed *Bohm velocity* $\mathbf{v}_\mathrm{B}$, thus fulfilling the so–called *Bohm criterion*. [Boh49]

This criterion will be derived in this chapter while following the argumentation from the original publication, but for the better understanding, some variables were changed. Further interpretation of the criterion involves the requirement of a so–called presheath, whose possible processes will be outlined. Afterwards, different methods for implementation of the criterion in PIC–simulations are introduced. Finally, a different and new interpretation of sheath edges with jump conditions will be given, on which the simulations in this thesis will rely.

2.1 Bohm criterion

2.1.1 Derivation and discussion

To investigate the topic of the plasma–sheath transition, a one–dimensional model is considered. The plasma is assumed to be in contact with a wall at $x = x_\mathrm{w}$, in front of which a sheath begins at $x = x_\mathrm{s} < x_\mathrm{w}$. This position is later referred to as the sheath edge. An overview over the geometry along with sketches of particle densities and the potential is given in Fig. 2.1. [Boh49]

The plasma is assumed to be quasi–neutral

$$Zen_\mathrm{i} - en_\mathrm{e} = 0 \qquad \Rightarrow \qquad n_\mathrm{e} = Zn_\mathrm{i} \tag{2.1}$$

where e is the elementary charge, Z is the charge number of the ions and n refers to the particle number density of each species, respectively. The sheath edge $x = x_\mathrm{s}$ is defined as the spatial border up to which quasi–neutrality is fulfilled, thus $n_\mathrm{es} = Zn_\mathrm{is}$ is valid at this specific position behind which this characteristic is violated. [Boh49]

The following assumptions are provided in context of laboratory experiments. Here, a plasma is created by ionization which yields secondary electrons with much higher kinetic energy than ions receive in this process. Due to high mobility, electrons will accumulate at walls and charge them negatively, resulting in an electric field that accelerates the ions to the wall. As a result of frequent collisions according to their high mobility, electrons are assumed to acquire a Maxwell–Boltzmann equilibrium

$$n_\mathrm{e}(x) = n_\mathrm{es} \exp\left(\frac{e(\Phi(x) - \Phi_\mathrm{s})}{k_\mathrm{B} T_\mathrm{e}}\right) \tag{2.2}$$

with T_e the electron temperature and Φ_s the potential at the sheath edge. For the treatment of ions, the conservation of energy of this particular species is considered, which connects the average velocity of an ion v_i with the potential Φ

$$\begin{aligned} &\frac{1}{2} m_\mathrm{i} v_\mathrm{i}(x)^2 + Ze\Phi(x) = \frac{1}{2} m_\mathrm{i} v_\mathrm{is}^2 + Ze\Phi_\mathrm{s} \\ \Rightarrow \quad &v_\mathrm{i}(x) = v_\mathrm{is} \sqrt{1 - \frac{2Ze}{m_\mathrm{i} v_\mathrm{is}^2}(\Phi(x) - \Phi_\mathrm{s})} \end{aligned} \tag{2.3}$$

where m_i is the ion mass and v_is is the velocity of the ions at the sheath edge. Additionally considering the mass transport equation yields an expression for the ion density n_i in dependence of the potential Φ

$$n_\mathrm{i} v_\mathrm{i} = n_\mathrm{is} v_\mathrm{is} \qquad \Rightarrow \qquad n_\mathrm{i}(x) = n_\mathrm{is} \frac{v_\mathrm{is}}{v_\mathrm{i}(x)} = n_\mathrm{is} \left(1 - \frac{2Ze}{m_\mathrm{i} v_\mathrm{is}^2}(\Phi(x) - \Phi_\mathrm{s})\right)^{-\frac{1}{2}}$$

where n_is is the ion density at the sheath edge. [Boh49]

Inserting the above introduced expressions for each particle density separately into Poisson's equation for electrostatics yields the so–called *plasma–sheath equation*

$$\frac{\partial^2 \Phi}{\partial x^2} = \frac{e}{\epsilon_0}(n_\mathrm{e} - Zn_\mathrm{i}) = \frac{Zen_\mathrm{is}}{\epsilon_0} \left\{ \exp\left(\frac{e\Delta\Phi}{k_\mathrm{B} T_\mathrm{e}}\right) - \left(1 - \frac{Ze\Delta\Phi}{T_\mathrm{is}}\right)^{-\frac{1}{2}} \right\} \tag{2.4}$$

where the newly occurring abbreviations are introduced for convenience.

$$\Delta\Phi(x) = \Phi(x) - \Phi_\mathrm{s} \qquad\qquad T_\mathrm{is} = \frac{1}{2} m_\mathrm{i} v_\mathrm{is}^2$$

This differential equation gets integrable after multiplying it by $\partial\Phi/\partial x$, so that applying integration from the sheath edge $x = x_\mathrm{s}$ up to an arbitrary position in the sheath $x_\mathrm{s} < x < x_\mathrm{w}$ yields the following expression. [Boh49]

$$\begin{aligned}\int_{x_\mathrm{s}}^{x} \frac{\partial^2\Phi}{\partial x'^2}\frac{\partial\Phi}{\partial x'}\,\mathrm{d}x' &= \frac{1}{2}\left[\left(\frac{\partial\Phi}{\partial x}\right)^2 - \left(\frac{\partial\Phi}{\partial x}\right)^2\bigg|_{x=x_\mathrm{s}}\right] \\ &= \frac{Zen_\mathrm{is}}{\epsilon_0}\left\{\frac{k_\mathrm{B}T_\mathrm{e}}{e}\left[\exp\left(\frac{e\Delta\Phi}{k_\mathrm{B}T_\mathrm{e}}\right) - 1\right] + \frac{2T_\mathrm{is}}{Ze}\left[\sqrt{1 - \frac{Ze\Delta\Phi}{T_\mathrm{is}}} - 1\right]\right\}\end{aligned}$$

In order to derive a condition that characterizes the ion motion at the sheath edge, the investigation of the behavior of each side of the equation is crucial. To be more precise, their respective signs need to be identified. For large potential drops in the sheath region due to electrons charging the wall, the right–hand side is obviously positive. To examine its behavior for small deviations around $\Delta\Phi \approx 0$, expansion up to the second order is considered

$$\exp(x) \approx 1 + x + \frac{x^2}{2} + O(x^3) \qquad \sqrt{1-x} \approx 1 - \frac{x}{2} - \frac{x^2}{8} + O(x^3)$$

in which the terms of zeroth and first order vanish.

$$\frac{1}{2}\left[\left(\frac{\partial\Phi}{\partial x}\right)^2 - \left(\frac{\partial\Phi}{\partial x}\right)^2\bigg|_{x=x_\mathrm{s}}\right] \approx \frac{Ze^2 n_\mathrm{is}}{2\epsilon_0}\left(\frac{1}{k_\mathrm{B}T_\mathrm{e}} - \frac{Z}{2T_\mathrm{is}}\right)(\Delta\Phi)^2 + O\left((\Delta\Phi)^3\right) \tag{2.5}$$

On the basis of general observations in experiments, the left–hand side is considered to be positive. Bohm claims that, near sheath edges, the electric field is vanishingly small and proposes a simple boundary condition.

$$\left(\frac{\partial\Phi}{\partial x}\right)\bigg|_{x=x_\mathrm{s}} = 0$$

Apparently with this boundary condition, solutions are only possible if the right–hand side of the equation is positive as well. For large potential drops this is fulfilled as remarked shortly before expansion has been applied. For small devi-

ation of the potential $\Delta\Phi$ however, the equation is only fulfilled it the following condition holds:

$$\frac{1}{k_\mathrm{B}T_\mathrm{e}} \geq \frac{Z}{2T_\mathrm{is}} \qquad \Leftrightarrow \qquad T_\mathrm{is} \geq \frac{Zk_\mathrm{B}T_\mathrm{e}}{2} \qquad \Leftrightarrow \qquad v_\mathrm{is} \geq \sqrt{\frac{Zk_\mathrm{B}T_\mathrm{e}}{m_\mathrm{i}}} =: v_\mathrm{B}$$

This is known as the *Bohm criterion* with *Bohm velocity* v_B. [Boh49]

To investigate the effect of this criterion on the plasma at the sheath border, an expansion of the original plasma–sheath equation (2.4) up to the first order is considered

$$\exp(x) \approx 1 + x + O(x^2) \qquad\qquad \sqrt{\frac{1}{1-x}} \approx 1 + \frac{x}{2} + O(x^2)$$

in which the terms of zeroth order vanish.

$$\frac{\partial^2\Phi}{\partial x^2} \approx \frac{Ze^2 n_\mathrm{is}}{\epsilon_0}\left(\frac{1}{k_\mathrm{B}T_\mathrm{e}} - \frac{Z}{2T_\mathrm{is}}\right)\Delta\Phi + O\left((\Delta\Phi)^2\right)$$

If the Bohm criterion is applied, the term inside the brackets is positive, thus leading to an exponential behavior of the potential and a stable sheath if the expanded equation is considered to be solved. If it is in the contrary violated, the potential becomes oscillatory, since the term gets negative. A further look on Poisson's equation provides a physical interpretation of this particular case. When its right–hand side gets negative, the ion density is dropping more than the electron density so that an excess of negative charge is occurring in the sheath. This excess of negative charge reverses the initially accelerating forces of the ions on the wall, thus resulting in an oscillatory potential. [Boh49]

In recent history of plasma–sheath theory, several approaches have been made to derive the Bohm criterion from a different perspective. The review article of Riemann [Rie91] provides a good summary on such contributions from which a short survey is outlined here. Permitting a pressure contribution of the ions on the plasma, the Bohm velocity can be generalized to the ion sound velocity

$$v_\mathrm{B} \to c_\mathrm{s} = \sqrt{\frac{\gamma k_\mathrm{B}T_\mathrm{i} + Zk_\mathrm{B}T_\mathrm{e}}{m_\mathrm{i}}}$$

with T_i the ion temperature and γ the adiabatic coefficient of a fluid element in this consideration. Respecting the full distribution of ions provides another way of generalization and yields the so–called *kinetic Bohm criterion*.

$$\left\langle \frac{1}{v^2} \right\rangle = \frac{m_\mathrm{i}}{Zk_\mathrm{B}T_\mathrm{e}}$$

Its derivation, however, has major flaws and is discussed in Riemann's review article in detail. [Rie91].

Although the Bohm criterion has become a common way to treat the ion motion at the sheath edge, there are still inconsistencies in its derivation. For example, the only difference Bohm takes into account between both particle species is that the electrons are treated Maxwell–Boltzmann distributed while for the ions only energy conservation is considered. This is not necessarily valid for every laboratory plasma. Especially when magnetized plasmas are taken into account, the Maxwell–Boltzmann assumption needs to be discarded. Additionally the boundary condition applied on the potential at the sheath edge is just based on experimental observation and needs further specification for a more accurate formulation, since this condition clearly has an impact on the Bohm velocity as seen in equation (2.5). Interestingly, no specification about the wall occurs in the derivation of the criterion at all, neither its position nor its potential. Nevertheless it leads to a universal result. Bohm claims that this criterion is not exact though, being applicable "[...] within 20 or 30 per cent [...] in practically all cases[]" [Boh49], for which the previous remarks are most likely the reason.

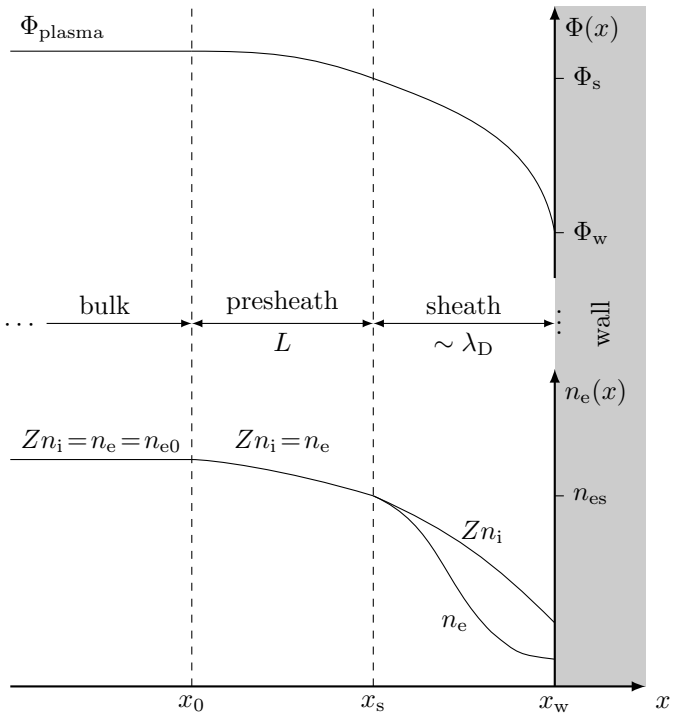

Figure 2.1: Qualitative behavior of potential and particle densities in contact with a wall. [LL05, based on Fig. 6.1]

2.1.2 Necessity of a presheath

The Bohm criterion states that ions passing the sheath edge have to exceed the Bohm velocity v_B. Thus ions need to be accelerated to this velocity, if they are too slow, which happens in the so–called *presheath* on a specific length L.

For the following explanations, the logarithmic derivative of the quasi–neutrality (2.1) in the region right before the presheath is considered.

$$\frac{1}{n_\mathrm{i}}\frac{\mathrm{d}n_\mathrm{i}}{\mathrm{d}x} = \frac{1}{n_\mathrm{i}}\frac{\mathrm{d}n_\mathrm{e}}{\mathrm{d}x}$$

Expressing the ion density in terms of $j_\mathrm{i} = Zen_\mathrm{i}v_\mathrm{i}$ and assuming Maxwell–Boltzmann distributed electrons (2.2) in this specific region, the equation becomes

$$\frac{e}{k_\mathrm{B}T_\mathrm{e}}\frac{\mathrm{d}\Phi}{\mathrm{d}x} = \frac{1}{j_\mathrm{i}}\frac{\mathrm{d}j_\mathrm{i}}{\mathrm{d}x} - \frac{1}{v_\mathrm{i}}\frac{\mathrm{d}v_\mathrm{i}}{\mathrm{d}x}.$$

For ions slower than Bohm velocity $v_\mathrm{i} < v_\mathrm{B}$ meaning that the Bohm criterion is not yet fulfilled, the above expression can be rewritten in an inequality.

$$\frac{e}{k_\mathrm{B}T_\mathrm{e}}\frac{\mathrm{d}\Phi}{\mathrm{d}x} + \frac{1}{v_\mathrm{B}}\frac{\mathrm{d}v_\mathrm{i}}{\mathrm{d}x} < \frac{1}{j_\mathrm{i}}\frac{\mathrm{d}j_\mathrm{i}}{\mathrm{d}x}$$

Remembering the dependency of the ion velocity on the potential from equation (2.3), one or both of the following conditions need to be fulfilled.

$$\text{(i)}\quad \frac{\mathrm{d}j_\mathrm{i}}{\mathrm{d}x} > 0 \qquad\qquad \text{(ii)}\quad \frac{1}{v_\mathrm{B}}\frac{\mathrm{d}v_\mathrm{i}}{\mathrm{d}x} < -\frac{e}{k_\mathrm{B}T_\mathrm{e}}\frac{\mathrm{d}\Phi}{\mathrm{d}x}$$

The right–hand side of the second condition is positive, since the potential is assumed to decrease monotonically. [Rie91]

These conditions are valid for different processes from which each one characterizes a specific type of presheath. The *geometric presheath* requires current concentration due to the wall's geometry, for example for spherical probes, and is thus applying to condition (i). The length scale L for this case is the curvature radius of the wall. When collisions are taken into account along with ion friction fulfilling condition (ii), the collisional presheath is built–up. Here, the presheath has a length L of the order of the ion mean free path. With ionization appearing together with mean ion retardation, thus conforming to both conditions (i) and (ii), the *ionizing presheath* occurs. Its length L is of the order of the ionization length. A special case of the presented processes is the *magnetic presheath* that does not require either of the above conditions. Here, the velocity of the ions perpendicular to the wall is converted by magnetic fields into the parallel direction, thus the presheath extends in several ion Larmor radii. [Rie91]

Since lengths of both sheath and presheath generally differ in many orders of magnitude, the analysis of the plasma–wall transition region leads to a two–scale problem in which the decision whether the sheath or the presheath shall be investigated is fundamental for the intended examination [Rie91]. Since the title of this thesis suggests the application of quasi–neutral models in the following, only the presheath is able to get resolved anyway. Thus a specific way to imply the Bohm criterion as a boundary condition right at each wall needs to be found.

2.2 Bohm forcing algorithms

Since the Bohm criterion has become a popular way to describe the plasma–wall transition, several PIC codes implement this condition in different manners. The algorithms presented in the following have been developed for the simulation of Hall–thrusters.

Lampe et al. propose a method for their simulation program applying the Bohm criterion as a boundary condition, which they refer to as the *Bohm logical sheath* procedure. In their algorithm, a sufficiently wide layer in front of the expected sheath edge is called out in which all ions are set to Bohm velocity. This type of imposition dynamically influences the quasi–neutral region of the plasma, resulting in an imitation of the presheath. [LJMS98]

Ahedo et al. resign from increasing the particles' velocities and increase their kinetic energy instead, which they refer to as *simple Bohm forcing*. They also propose an implementation for the kinetic Bohm criterion, resulting in their *kinetic Bohm forcing* algorithm in which the ion velocity distribution in the specified area is taken into account to calculate the increment for the kinetic energy that is applied on the ions. [ASP10]

Chapter 3

Modeling plasma–wall–interactions in one dimension

3.1 Formulation of the investigated problem

Since this thesis is motivated by plasma–wall interactions, an elaborated model is required to investigate this topic. Particular interest lies in the plasma source of the PSI–2 experiment so that its characteristics, as introduced in section 1.2, must be adopted properly in the formulation of the model. On the other hand, this model shall be kept as simple as possible to achieve elementary results. In this spirit the geometry and the basic processes of the PSI–2 plasma source shall be reduced to a fundamental model which will be the basis for further investigations.

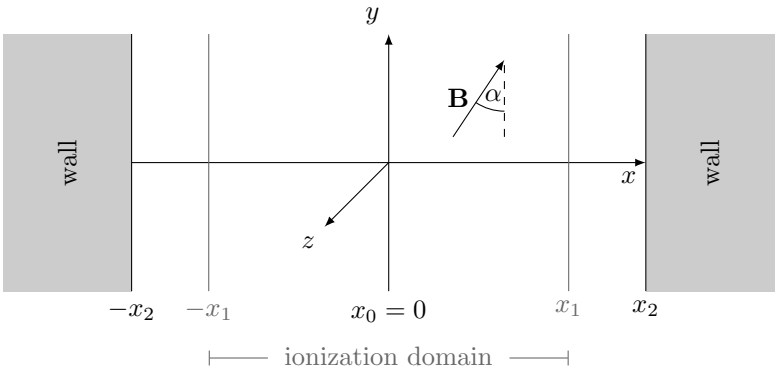

Figure 3.1: Sketch of the domain of the introduced model.

Any laboratory plasma experiment is bounded by surrounding walls. In the PSI–2 plasma source a hollow cathode discharge is used, which provides cathode and anode as additional walls directly exposed to the plasma (see Fig. 1.1). To investigate the effects caused by walls on a plasma, a one–dimensional model ($\partial_\mathrm{y} = 0$, $\partial_\mathrm{z} = 0$) is supplied. As shown in Fig. 3.1, two planar walls confine the domain in which plasma is ionized in an area between $-x_1$ and x_1 symmetric to $x_0 = 0$. For simplicity in this consideration, totally absorbing walls are assumed.

A magnetic field is imposed externally. The cartesian coordinate system of the model is chosen so that $\mathbf{B} = B_\mathrm{x}\mathbf{e}_\mathrm{x} + B_\mathrm{y}\mathbf{e}_\mathrm{y}$ where B_x is the component perpendicular to the wall and B_y the one parallel to it. The external magnetic field is assumed to be sufficiently large so that it exceeds the magnetic field induced by the electric current which is thus neglected. This assumption is valid for the PSI–2 experiment as shown in the following estimation of the absolute values of the induced field B_1 and the external one B_0 by considering Ampère's law and the PSI–2 parameters from Tab. 1.1. Hereby an axially symmetric, circular path C around the plasma of radius R is chosen through which the applied current on the electrodes I flows. For a rough estimation both path and magnetic field $\mathbf{B}_1$ are assumed to have an identical shape. The displacement current vanishes in a stationary state.

$$\oint_C \mathbf{B}_1 \cdot \mathrm{d}\mathbf{s} = 2\pi R B_1 = \mu_0 I_\mathrm{max} \qquad \Leftrightarrow \qquad \frac{B_1}{B_0} = \frac{\mu_0 I_\mathrm{max}}{2\pi R B_0} = \frac{1}{15}$$

The plasma is expected to reach a time–independent ($\partial_\mathrm{t} = 0$) stationary state at which sheaths are built up, so that the plasma quantities form spatial profiles. Thus the electric field needs to be irrotational due to Faraday's induction law, which yields to the following conditions in the one–dimensional model.

$$\nabla \times \mathbf{E} = -\partial_\mathrm{t}\mathbf{B} = 0 \qquad \Rightarrow \qquad \partial_\mathrm{x} E_\mathrm{y} = 0 \qquad \text{and} \qquad \partial_\mathrm{x} E_\mathrm{z} = 0 \tag{3.1}$$

This would also motivate defining a potential ϕ with $\mathbf{E} = -\nabla\phi$ which is nonessential in the following considerations.

In this model, only ion–electron collisions are taken into account. Although other collision types are also relevant for the PSI–2 experiment (see Tab. 1.3) this is the only one considered to keep the investigation as basic as possible. Others can be added easily by following the calculations straightforwardly in this thesis. In this context ion density n_i and ion–electron collision frequency ν_ie are correlated

$$\frac{\nu_\mathrm{ie}}{n_\mathrm{i}} \coloneqq \hat{\nu}_\mathrm{ie} = \text{const.} \tag{3.2}$$

so that the collision frequency is proportional to the ion density with the constant $\hat{\nu}_{\mathrm{ie}}$. [AGB05]

Referring to temperatures, electrons are treated isothermally. One possible justification for this assumption is, that the electrons are heated by the electrodes and distribute their energy fast in the whole domain because of high thermal conductivity. On the other hand they are radiating thermally until an equilibrium with a constant temperature is reached.

No specification for the ions about their temperature is necessary in hybrid simulations, since they are treated as particles here. Later on, a two–fluid formulation as comparison with the hybrid results is provided, though for which the ion temperature needs to be specified. For simplicity, the ions are assumed to stay cold, which may be justified by their high inertia.

3.2 Modeling totally absorbing walls and ionization

One condition for a stationary state is, that particle losses by wall absorption balance their ionization sources. In the hybrid simulations, which will be introduced later, this is implemented in the PIC–treatment of the ion species by removing those particles impeding the wall and resupplying them in the ionization domain. Thus losses are directly related to sources rather than prescribing ionization rate constants which makes the implementation of the PIC–model easier, because the number of particles throughout the simulation is preserved.

Position and momentum of the recently ionized particles are handled with probability density functions (pdf) that are symmetric to $x_0 = 0$ and vanish outside the ionization domain of width $2x_1$. Here, two different pdfs are introduced, which satisfy these conditions, namely a constant distribution

$$f_{\mathrm{cd}}(x) = \begin{cases} \frac{1}{2x_1} & \text{for } |x| \leq x_1 \\ 0 & \text{for } |x| > x_1 \end{cases} \tag{3.3}$$

and a raised cosine distribution [Rin10]

$$f_{\mathrm{rcd}}(x) = \begin{cases} \frac{1}{2x_1}\left[1 + \cos\left(\pi \frac{x}{x_1}\right)\right] & \text{for } |x| \leq x_1 \\ 0 & \text{for } |x| > x_1 \end{cases} \tag{3.4}$$

where x_1 is half the width of both pdfs. The benefit of the cosine distribution over the constant one is, that it is smooth and falls down to zero at the borders of the ionization domain, however it makes a later analysis more complex.

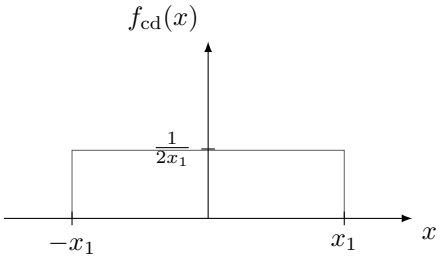

(a) Probability density function.

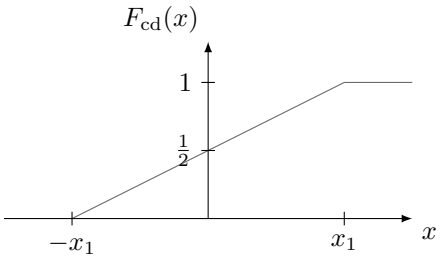

(b) Cumulative distribution function.

Figure 3.2: Constant distribution.

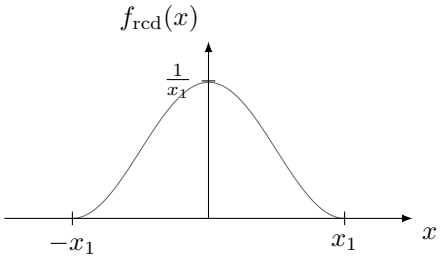

(a) Probability density function.

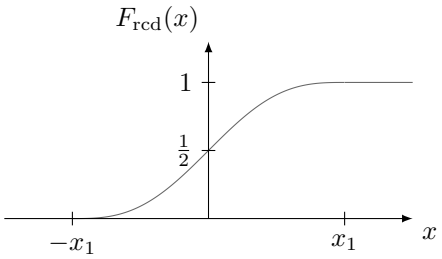

(b) Cumulative distribution function.

Figure 3.3: Raised cosine distribution.

The corresponding cumulative distribution functions (cdf) are provided in the following.

$$F_{\mathrm{cd}}(x) = \int_{-\infty}^{x} f_{\mathrm{cd}}(x')\,\mathrm{d}x' = \begin{cases} 0 & \text{for } x < -x_1 \\ \frac{1}{2}\left[1 + \frac{x}{x_1}\right] & \text{for } |x| \le x_1 \\ 1 & \text{for } x > x_1 \end{cases} \tag{3.5}$$

$$F_{\mathrm{rcd}}(x) = \int_{-\infty}^{x} f_{\mathrm{rcd}}(x')\,\mathrm{d}x' = \begin{cases} 0 & \text{for } x < -x_1 \\ \frac{1}{2}\left[1 + \frac{x}{x_1} + \frac{1}{\pi}\sin\left(\pi\frac{x}{x_1}\right)\right] & \text{for } |x| \le x_1 \\ 1 & \text{for } x > x_1 \end{cases} \tag{3.6}$$

For the later two–fluid analysis it is necessary to introduce and specify source densities for both mass s_{n} and momentum $\mathbf{s}_{\mathrm{p}}$ for the ion species. The ionization as presented above yields an analytical term for s_{n}

$$s_{\mathrm{n}}(x) = A\ f(x) \tag{3.7}$$

with A a constant factor and f a probability density function. Two different models for treating the momentum of newly ionized particles are realized. Firstly ions are inserted with zero velocity which is interpreted as they are ionized from a resting gas background, so that no additional momentum is provided.

This sets the momentum source density to zero.

$$\mathbf{s}_\mathrm{p}(x) = 0 \tag{3.8}$$

Secondly, assuming they are ionized from a comoving background gas, ions adopt the fluid velocity at the point of reinsertion so that $\mathbf{s}_\mathrm{p}$ becomes

$$\mathbf{s}_\mathrm{p}(x) = s_\mathrm{n}(x)\mathbf{u}_\mathrm{i}(x) \tag{3.9}$$

where $\mathbf{u}_\mathrm{i}$ is the average ion velocity.

The constant A from equation (3.7) is determined by particle number conservation. Considering the ion mass transport equation

$$\partial_\mathrm{x}(n_\mathrm{i}u_\mathrm{ix}) = s_\mathrm{n} = A\ f(x)$$

the constant A can be obtained by integration and is thus correlated with both mass fluxes $(n_\mathrm{i}u_\mathrm{ix})_1$ and $(n_\mathrm{i}u_\mathrm{ix})_0$ at the boundaries of the integration domain x_1 and $x_0 = 0$.

$$\begin{aligned}
\int_0^{x_1} \partial_\mathrm{x}(n_\mathrm{i}u_\mathrm{ix})\,\mathrm{d}x &= A\int_0^{x_1} f(x)\,\mathrm{d}x \\
\Leftrightarrow \qquad (n_\mathrm{i}u_\mathrm{ix})_1 - (n_\mathrm{i}u_\mathrm{ix})_0 &= A\ [\ \underbrace{F(x_1)}_{=1} - \underbrace{F(0)}_{=\frac{1}{2}}\ ] = \frac{A}{2} \\
\Leftrightarrow \qquad A &= 2\ [\ (n_\mathrm{i}u_\mathrm{ix})_1 - (n_\mathrm{i}u_\mathrm{ix})_0\ ]
\end{aligned} \tag{3.10}$$

Here, $F(x)$ describes the cumulative distribution function to the respective probability density function $f(x)$. Since the domain is symmetric, the integration domain is chosen to be from $x_0 = 0$ to x_1, so that later equations will be more easy to be read.

In this context the integrated form of the mass source density S_n is introduced for later purposes.

$$\begin{aligned}
S_\mathrm{n}(x) &\coloneqq \int_0^{x} s_\mathrm{n}(x')\,\mathrm{d}x' = A\left(F(x) - \frac{1}{2}\right) \\
&= 2\ [\ (n_\mathrm{i}u_\mathrm{ix})_1 - (n_\mathrm{i}u_\mathrm{ix})_0\ ]\left(F(x) - \frac{1}{2}\right)
\end{aligned} \tag{3.11}$$

To achieve mass conservation everything moving out of the ionization domain must be replenished inside. This statement can also be expressed with an equation for S_n.

$$S_\mathrm{n}(x > x_1) = (n_\mathrm{i}u_\mathrm{ix})_1 - (n_\mathrm{i}u_\mathrm{ix})_0 \tag{3.12}$$

Chapter 4

Physical plasma models

Since the model for plasma–wall–interactions is now explained, models to describe the plasma itself need to be introduced, namely a two–fluid and a hybrid model. The hybrid model is the basis for simulations in this thesis, whilst the two–fluid model is provided as a reference for comparison of the results.

4.1 Two–fluid model

In this section a three–dimensional formulation of the two–fluid model will be presented, which will be reduced later to one dimension.

This model is motivated by the work of Alterkop et al. The basis of their examination are stationary ($\partial_\mathrm{t} = 0$) equations for mass transport and momentum balance for electrons and ions separately, while collisions between them are taken into account. For the electrons in equation (4.2) it is assumed, that their thermal velocity exceeds their directed velocity, so that the inertia term is neglected. [AGB05]

These equations are extended by the ionization model as described in chapter 3. For this purpose additional source densities for mass s_n and momentum $\mathbf{s}_\mathrm{p}$ are provided. The latter is relevant only for the ions since electron inertia is negligibly small.

$$\nabla \cdot (n_\mathrm{i} \mathbf{u}_\mathrm{i}) = s_\mathrm{n} \tag{4.1}$$

$$0 = -en_\mathrm{e} (\mathbf{E} + \mathbf{u}_\mathrm{e} \times \mathbf{B}) - \nabla p_\mathrm{e} - m_\mathrm{e} n_\mathrm{e} \nu_\mathrm{ei} (\mathbf{u}_\mathrm{e} - \mathbf{u}_\mathrm{i}) \tag{4.2}$$

$$m_\mathrm{i} \nabla \cdot (n_\mathrm{i} \mathbf{u}_\mathrm{i} \mathbf{u}_\mathrm{i}) = Zen_\mathrm{i} (\mathbf{E} + \mathbf{u}_\mathrm{i} \times \mathbf{B}) - \nabla p_\mathrm{i} - m_\mathrm{i} n_\mathrm{i} \nu_\mathrm{ie} (\mathbf{u}_\mathrm{i} - \mathbf{u}_\mathrm{e}) + m_\mathrm{i} \mathbf{s}_\mathrm{p} \tag{4.3}$$

Since charge is conserved in the ionization process, the electron mass transport equation can be derived from the equivalent one for the ions (4.1) and the

continuity equation.

$$\nabla \cdot \mathbf{j} = \nabla \cdot (Zen_\mathrm{i}\mathbf{u}_\mathrm{i} - en_\mathrm{e}\mathbf{u}_\mathrm{e}) = 0 \qquad \Leftrightarrow \qquad \nabla \cdot (n_\mathrm{e}\mathbf{u}_\mathrm{e}) = Zs_\mathrm{n}$$

As described in section 3, ions and electrons are treated isothermally, so that their respective pressure gradients can be written as

$$\nabla p_\mathrm{i} = k_\mathrm{B}T_\mathrm{i}\nabla n_\mathrm{i}, \qquad \nabla p_\mathrm{e} = k_\mathrm{B}T_\mathrm{e}\nabla n_\mathrm{e} = Zk_\mathrm{B}T_\mathrm{e}\nabla n_\mathrm{i}.$$

Due to momentum conservation the contribution of collisions between particles to the momentum balance must vanish in total. This yields the following relationship between both collision terms and the collision frequencies while taking into account quasi–neutrality (2.1).

$$m_\mathrm{e}n_\mathrm{e}\nu_\mathrm{ei} = m_\mathrm{i}n_\mathrm{i}\nu_\mathrm{ie} \qquad \Leftrightarrow \qquad Zm_\mathrm{e}\nu_\mathrm{ei} = m_\mathrm{i}\nu_\mathrm{ie} \tag{4.4}$$

The electric field is derived from the electron momentum balance (4.2).

$$\mathbf{E} = -\mathbf{u}_\mathrm{e} \times \mathbf{B} - \frac{\nabla p_\mathrm{e}}{en_\mathrm{e}} - \frac{m_\mathrm{e}\nu_\mathrm{ei}}{e}\left(\mathbf{u}_\mathrm{e} - \mathbf{u}_\mathrm{i}\right)$$

Assuming quasi–neutrality (2.1) and substituting the collision frequency (4.4), all electron quantities except for the fluid velocities are replaced by ion equivalents which will be useful for later purposes.

$$\mathbf{E} = -\mathbf{u}_\mathrm{e} \times \mathbf{B} - \frac{k_\mathrm{B}T_\mathrm{e}}{e}\frac{\nabla n_\mathrm{i}}{n_\mathrm{i}} - \frac{m_\mathrm{i}\nu_\mathrm{ie}}{Ze}\left(\mathbf{u}_\mathrm{e} - \mathbf{u}_\mathrm{i}\right) \tag{4.5}$$

Again considering quasi–neutrality (2.1) both momentum balance equations can be summed up to the total momentum balance equation.

$$m_\mathrm{i}\nabla \cdot (n_\mathrm{i}\mathbf{u}_\mathrm{i}\mathbf{u}_\mathrm{i}) = Zen_\mathrm{i}\left(\mathbf{u}_\mathrm{i} - \mathbf{u}_\mathrm{e}\right) \times \mathbf{B} - \nabla(p_\mathrm{e} + p_\mathrm{i}) + m_\mathrm{i}\mathbf{s}_\mathrm{p} \tag{4.6}$$

Using the product rule on the left hand side of the total momentum equation and recognizing the mass transport equation (4.1)

$$\nabla \cdot (n_\mathrm{i}\mathbf{u}_\mathrm{i}\mathbf{u}_\mathrm{i}) = \mathbf{u}_\mathrm{i}(\nabla \cdot (n_\mathrm{i}\mathbf{u}_\mathrm{i})) + (n_\mathrm{i}\mathbf{u}_\mathrm{i} \cdot \nabla)\mathbf{u}_\mathrm{i} = s_\mathrm{n}\mathbf{u}_\mathrm{i} + n_\mathrm{i}(\mathbf{u}_\mathrm{i} \cdot \nabla)\mathbf{u}_\mathrm{i}$$

the total momentum balance equation finally becomes

$$n_\mathrm{i}(\mathbf{u}_\mathrm{i} \cdot \nabla)\mathbf{u}_\mathrm{i} = n_\mathrm{i}\left(\mathbf{u}_\mathrm{i} - \mathbf{u}_\mathrm{e}\right) \times \boldsymbol{\Omega}_\mathrm{i} - c_\mathrm{s}^2(\nabla n_\mathrm{i}) - s_\mathrm{n}\mathbf{u}_\mathrm{i} + \mathbf{s}_\mathrm{p} \tag{4.7}$$

with $\mathbf{\Omega}_\mathrm{i}$ the ion gyro frequency and c_s the ion sound velocity.

$$\mathbf{\Omega}_\mathrm{i} = \frac{Ze}{m_\mathrm{i}}\mathbf{B} \qquad\qquad c_\mathrm{s} = \sqrt{\frac{Zk_\mathrm{B}T_\mathrm{e} + k_\mathrm{B}T_\mathrm{i}}{m_\mathrm{i}}}$$

4.1.1 One–dimensional formulation

The one–dimensional formulation ($\partial_\mathrm{y} = 0, \partial_\mathrm{z} = 0$) of the foregoing equations with a magnetic field $\mathbf{B} = B_\mathrm{x}\mathbf{e}_\mathrm{x} + B_\mathrm{y}\mathbf{e}_\mathrm{y}$ is needed for the comparison with the hybrid simulations (see section 3). Since the domain is symmetric, it is sufficient to consider only one side of the domain for the analytical treatment. In this context the mass transport equation

$$\partial_\mathrm{x}(n_\mathrm{i}u_\mathrm{ix}) = s_\mathrm{n}$$

leads to the spatial derivative of the ion density

$$\partial_\mathrm{x}n_\mathrm{i} = \frac{s_\mathrm{n} - n_\mathrm{i}\partial_\mathrm{x}u_\mathrm{ix}}{u_\mathrm{ix}} \tag{4.8}$$

and its integrated form yields

$$n_\mathrm{i}u_\mathrm{ix} = (n_\mathrm{i}u_\mathrm{ix})_0 + S_\mathrm{n} \tag{4.9}$$

with the integrated mass source density S_n from equation (3.11). The total momentum balance equation has the following form in the one–dimensional formulation.

$$\begin{aligned}
n_\mathrm{i}u_\mathrm{ix}\partial_\mathrm{x}u_\mathrm{ix} &= -n_\mathrm{i}\left(u_\mathrm{iz} - u_\mathrm{ez}\right)\Omega_\mathrm{iy} - c_\mathrm{s}^2\partial_\mathrm{x}n_\mathrm{i} - s_\mathrm{n}u_\mathrm{ix} + s_\mathrm{px} \\
n_\mathrm{i}u_\mathrm{ix}\partial_\mathrm{x}u_\mathrm{iy} &= n_\mathrm{i}\left(u_\mathrm{iz} - u_\mathrm{ez}\right)\Omega_\mathrm{ix} - s_\mathrm{n}u_\mathrm{iy} + s_\mathrm{py} \\
n_\mathrm{i}u_\mathrm{ix}\partial_\mathrm{x}u_\mathrm{iz} &= n_\mathrm{i}\left[\left(u_\mathrm{ix} - u_\mathrm{ex}\right)\Omega_\mathrm{iy} - \left(u_\mathrm{iy} - u_\mathrm{ey}\right)\Omega_\mathrm{ix}\right] - s_\mathrm{n}u_\mathrm{iz} + s_\mathrm{pz}
\end{aligned}$$

By eliminating the ion density by means of equations (4.8) and (4.9) the complete system of differential equations is expressed wholly by the fluid velocities and the source terms.

$$\begin{aligned}
\left(u_\mathrm{ix} - \frac{c_\mathrm{s}^2}{u_\mathrm{ix}}\right)\partial_\mathrm{x}u_\mathrm{ix} = &-\left(u_\mathrm{iz} - u_\mathrm{ez}\right)\Omega_\mathrm{iy} \\
&+ \frac{u_\mathrm{ix}}{(n_\mathrm{i}u_\mathrm{ix})_0 + S_\mathrm{n}}\left(s_\mathrm{px} - s_\mathrm{n}\left(u_\mathrm{ix} + \frac{c_\mathrm{s}^2}{u_\mathrm{ix}}\right)\right)
\end{aligned} \tag{4.10}$$

$$u_{\mathrm{ix}}\partial_{\mathrm{x}}u_{\mathrm{iy}} = (u_{\mathrm{iz}} - u_{\mathrm{ez}})\,\Omega_{\mathrm{ix}} + \frac{u_{\mathrm{ix}}}{(n_{\mathrm{i}}u_{\mathrm{ix}})_0 + S_{\mathrm{n}}}\,(s_{\mathrm{py}} - s_{\mathrm{n}}u_{\mathrm{iy}}) \tag{4.11}$$

$$u_{\mathrm{ix}}\partial_{\mathrm{x}}u_{\mathrm{iz}} = [(u_{\mathrm{ix}} - u_{\mathrm{ex}})\,\Omega_{\mathrm{iy}} - (u_{\mathrm{iy}} - u_{\mathrm{ey}})\,\Omega_{\mathrm{ix}}] + \frac{u_{\mathrm{ix}}}{(n_{\mathrm{i}}u_{\mathrm{ix}})_0 + S_{\mathrm{n}}}\,(s_{\mathrm{pz}} - s_{\mathrm{n}}u_{\mathrm{iz}}) \tag{4.12}$$

Since the source terms are defined in chapter 3, the only quantities left to be specified for the solution of the above equations are the electron fluid velocities. These are obtained from the restriction on an irrotational electric field which is shown in the following section.

4.1.2 Enforcing irrotational electric fields

In the time–independent model the electric field needs to be irrotational as mentioned in chapter 3. This requires the electric field components E_{y} and E_{z} to be spatially constant in the one–dimensional formulation. Applying this condition (3.1) on the electric field (4.5) yields

$$\begin{aligned} E_{\mathrm{y}} &= -B_{\mathrm{x}}u_{\mathrm{ez}} - \frac{m_{\mathrm{i}}\nu_{\mathrm{ie}}}{Ze}(u_{\mathrm{ey}} - u_{\mathrm{iy}}) = \text{const.} \\ E_{\mathrm{z}} &= -B_{\mathrm{y}}u_{\mathrm{ex}} + B_{\mathrm{x}}u_{\mathrm{ey}} - \frac{m_{\mathrm{i}}\nu_{\mathrm{ie}}}{Ze}(u_{\mathrm{ez}} - u_{\mathrm{iz}}) = \text{const.} \end{aligned}$$

Rearranging the above conditions yields

$$\begin{aligned} u_{\mathrm{ey}} - u_{\mathrm{iy}} &= \frac{1}{\nu_{\mathrm{ie}}}\left(-\Omega_{\mathrm{ix}}u_{\mathrm{ez}} - \widetilde{E}_{\mathrm{y}}\right) \\ u_{\mathrm{ez}} - u_{\mathrm{iz}} &= \frac{1}{\nu_{\mathrm{ie}}}\left(-\Omega_{\mathrm{iy}}u_{\mathrm{ex}} + \Omega_{\mathrm{ix}}u_{\mathrm{ey}} - \widetilde{E}_{\mathrm{z}}\right) \end{aligned}$$

where the constant electric field components are treated as boundary conditions and are rewritten for better readability.

$$\widetilde{E}_{\mathrm{y}} = \frac{Ze}{m_{\mathrm{i}}}E_{\mathrm{y}} \qquad\qquad \widetilde{E}_{\mathrm{z}} = \frac{Ze}{m_{\mathrm{i}}}E_{\mathrm{z}}$$

Solving these equations for u_{ez} and u_{ey} respectively yields

$$\begin{aligned} u_{\mathrm{ey}} - u_{\mathrm{iy}} &= \frac{\Omega_{\mathrm{ix}}\left[\Omega_{\mathrm{iy}}u_{\mathrm{ex}} - \Omega_{\mathrm{ix}}u_{\mathrm{iy}} - \nu_{\mathrm{ie}}u_{\mathrm{iz}} - \widetilde{E}_{\mathrm{z}}\right] - \nu_{\mathrm{ie}}\widetilde{E}_{\mathrm{y}}}{\Omega_{\mathrm{ix}}^2 + \nu_{\mathrm{ie}}^2} \\ \Leftrightarrow \quad u_{\mathrm{ey}} &= \frac{\Omega_{\mathrm{ix}}\left[\Omega_{\mathrm{iy}}u_{\mathrm{ex}} - \nu_{\mathrm{ie}}u_{\mathrm{iz}} - \widetilde{E}_{\mathrm{z}}\right] + \nu_{\mathrm{ie}}^2u_{\mathrm{iy}} - \nu_{\mathrm{ie}}\widetilde{E}_{\mathrm{y}}}{\Omega_{\mathrm{ix}}^2 + \nu_{\mathrm{ie}}^2}, \end{aligned}$$

$$u_{\mathrm{ez}} - u_{\mathrm{iz}} = \frac{\nu_{\mathrm{ie}}\left[-\Omega_{\mathrm{iy}}u_{\mathrm{ex}} + \Omega_{\mathrm{ix}}u_{\mathrm{iy}} - \widetilde{E}_{\mathrm{z}}\right] - \Omega_{\mathrm{ix}}^2 u_{\mathrm{iz}} - \Omega_{\mathrm{ix}}\widetilde{E}_{\mathrm{y}}}{\Omega_{\mathrm{ix}}^2 + \nu_{\mathrm{ie}}^2}$$

$$\Leftrightarrow \quad u_{\mathrm{ez}} = \frac{\nu_{\mathrm{ie}}\left[-\Omega_{\mathrm{iy}}u_{\mathrm{ex}} + \Omega_{\mathrm{ix}}u_{\mathrm{iy}} - \widetilde{E}_{\mathrm{z}}\right] + \nu_{\mathrm{ie}}^2 u_{\mathrm{iz}} - \Omega_{\mathrm{ix}}\widetilde{E}_{\mathrm{y}}}{\Omega_{\mathrm{ix}}^2 + \nu_{\mathrm{ie}}^2}.$$

The remaining x–component of the electron fluid velocity is determined by the corresponding continuity equation and is thus related to a wall current density j_{w} perpendicular to the wall surfaces which is determined by the current I flowing between the electrodes.

$$n_{\mathrm{i}}(u_{\mathrm{ix}} - u_{\mathrm{ex}}) = \frac{j_{\mathrm{w}}}{Ze} \coloneqq \widetilde{j}_{\mathrm{w}} \qquad \Leftrightarrow \qquad u_{\mathrm{ex}} = u_{\mathrm{ix}} - \frac{\widetilde{j}_{\mathrm{w}}}{n_{\mathrm{i}}} \tag{4.13}$$

Hence the final expressions for the other two velocity components become

$$u_{\mathrm{ey}} = \frac{\Omega_{\mathrm{ix}}\left[\Omega_{\mathrm{iy}}\left(u_{\mathrm{ix}} - \frac{\widetilde{j}_{\mathrm{w}}}{n_{\mathrm{i}}}\right) - \nu_{\mathrm{ie}}u_{\mathrm{iz}} - \widetilde{E}_{\mathrm{z}}\right] + \nu_{\mathrm{ie}}^2 u_{\mathrm{iy}} - \nu_{\mathrm{ie}}\widetilde{E}_{\mathrm{y}}}{\Omega_{\mathrm{ix}}^2 + \nu_{\mathrm{ie}}^2} \tag{4.14}$$

$$u_{\mathrm{ez}} = \frac{\nu_{\mathrm{ie}}\left[-\Omega_{\mathrm{iy}}\left(u_{\mathrm{ix}} - \frac{\widetilde{j}_{\mathrm{w}}}{n_{\mathrm{i}}}\right) + \Omega_{\mathrm{ix}}u_{\mathrm{iy}} - \widetilde{E}_{\mathrm{z}}\right] + \nu_{\mathrm{ie}}^2 u_{\mathrm{iz}} - \Omega_{\mathrm{ix}}\widetilde{E}_{\mathrm{y}}}{\Omega_{\mathrm{ix}}^2 + \nu_{\mathrm{ie}}^2}. \tag{4.15}$$

With the above equations the electric field (4.5) in the one–dimensional model can be calculated directly from the ion fluid velocities for an arbitrary magnetic field while taking into account ion–electron collisions.

4.2 Hybrid model

In this section the hybrid model is described, which is used for the simulations in this thesis. This model was already presented in detail in the foregoing Bachelor thesis [Feh13] and will be adapted to the one–dimensional model from chapter 3.

The hybrid model treats ions kinetically in a PIC–model whilst considering the electrons as a background fluid. Here, the electrons determine the electric field $\mathbf{E}$ by their momentum balance which was already derived in equation (4.5). Since the only interest lies in stationary states here, an irrotational electric field is enforced as described in the previous section. Although the PIC–model treats the particles' motion time–dependently, their trajectory does not change in a stationary state. Thus after initialization, the simulation yields an iterative process to reach one specific state.

Since ions are combined in individual superparticles, their motion is deter-

mined by the Lorentz force

$$\frac{\mathrm{d}}{\mathrm{d}t}\mathbf{v}_{\mathrm{i}\alpha} = \frac{Ze}{m_{\mathrm{i}}}\left[\mathbf{E}_{\mathrm{mod}}(\mathbf{x}_{\mathrm{i}\alpha}) + \mathbf{v}_{\mathrm{i}\alpha} \times \mathbf{B}(\mathbf{x}_{\mathrm{i}\alpha})\right] \tag{4.16}$$

with

$$\mathbf{E}_{\mathrm{mod}}(\mathbf{x}_{\mathrm{i}\alpha}) = \mathbf{E}(\mathbf{x}_{\mathrm{i}\alpha}) - \frac{m_{\mathrm{i}}}{Ze}\nu_{\mathrm{ie}}(\mathbf{x}_{\mathrm{i}\alpha})\left[\mathbf{v}_{\mathrm{i}\alpha} - \mathbf{u}_{\mathrm{e}}(\mathbf{x}_{\mathrm{i}\alpha})\right], \tag{4.17}$$

where α is the particle index. Here a modified electric field $\mathbf{E}_{\mathrm{mod}}$ is introduced that additionally applies averaged electron–ion–collisions on the ions. Inserting the electric field (4.5) reveals that this particular choice yields a relaxation of the individual ion velocities to their average velocity and thus provides a cooling effect on the ions corresponding to the model from chapter 3.

$$\mathbf{E}_{\mathrm{mod}}(\mathbf{x}_{\mathrm{i}\alpha}) = -\mathbf{u}_{\mathrm{e}}(\mathbf{x}_{\mathrm{i}\alpha}) \times \mathbf{B} - \frac{k_{\mathrm{B}}T_{\mathrm{e}}}{e}\frac{\nabla n_{\mathrm{i}}(\mathbf{x}_{\mathrm{i}\alpha})}{n_{\mathrm{i}}(\mathbf{x}_{\mathrm{i}\alpha})} - \frac{m_{\mathrm{i}}}{Ze}\nu_{\mathrm{ie}}(\mathbf{x}_{\mathrm{i}\alpha})\left[\mathbf{v}_{\mathrm{i}\alpha}(\mathbf{x}_{\mathrm{i}\alpha}) - \mathbf{u}_{\mathrm{i}}(\mathbf{x}_{\mathrm{i}\alpha})\right]$$

With this additional collision term the ion momentum equation would become

$$\begin{aligned} m_{\mathrm{i}}n_{\mathrm{i}}\partial_{\mathrm{t}}\mathbf{u}_{\mathrm{i}} &= Zen_{\mathrm{i}}\left(\mathbf{E}_{\mathrm{mod}} + \mathbf{u}_{\mathrm{i}} \times \mathbf{B}\right) - \nabla p_{\mathrm{i}} \\ &= Zen_{\mathrm{i}}\left(\mathbf{E} + \mathbf{u}_{\mathrm{i}} \times \mathbf{B}\right) - \nabla p_{\mathrm{i}} - m_{\mathrm{i}}n_{\mathrm{i}}\nu_{\mathrm{ie}}\left(\mathbf{u}_{\mathrm{i}} - \mathbf{u}_{\mathrm{e}}\right) \end{aligned}$$

which equals the ion momentum balance equation (4.3, without momentum source density) and validates the modification.

4.3 Normalization

If a normalization is considered it needs to be applied on both models to make a comparison possible. For the normalization of a physical quantity f, it is separated in a numerical value $\bar{f}$ and a constant scale $\mathring{f}$ so that $f(x) = \bar{f}(x)\mathring{f}$.

Here the velocity is normalized to the ion sound velocity c_{s} for cold ions ($T_{\mathrm{i}} = 0$) and the temperature is normalized to the constant electron temperature. Since the ion motion is determined by the magnetic field, length and time are normalized to the ion Larmor radius and the inverse ion gyro frequency, respectively,

$$\mathring{T} = T_{\mathrm{e}}, \quad \mathring{v} = c_{\mathrm{s}}(T_{\mathrm{i}} = 0) = \sqrt{\frac{Zk_{\mathrm{B}}T_{\mathrm{e}}}{m_{\mathrm{i}}}}, \quad \mathring{t} = \mathring{\Omega}_{\mathrm{i}}^{-1} = \frac{m_{\mathrm{i}}}{Ze\mathring{B}}, \quad \mathring{l} = \mathring{r}_{\mathrm{i}} = \frac{m_{\mathrm{i}}\mathring{v}}{Ze\mathring{B}}$$

with $\mathring{B}$ the normalization value of the magnetic field. The ion density is normalized to an arbitrary constant n_0.

For the case without a magnetic field, the length scale is arbitrary whereas the normalization of time is determined by $\mathring{t} = \mathring{l}/\mathring{v}$.

Chapter 5

Numerical implementation of the one–dimensional hybrid model

The hybrid model is used for simulations in this thesis. Since its theory has been introduced in the previous section 4.2, its numerical implementation will be described in this chapter.

5.1 Particle–in–cell method

In simulations including kinetic effects, each particles' motion needs to be imaged properly, which occupies an incredible amount of computational resources. A common method to simplify these kind of simulations is the particle–in–cell method (PIC) which will be used for the hybrid simulations. Its basic idea is to divide the domain into a grid of uniformly shaped cells, with which the particles are interacting instead of considering each interaction between them. To do so plasma quantities are transfered to the grid and interpolated on each particle's position if required. To further save computational resources, particles are merged to superparticles describing particle clouds. [BL85]

For three–dimensional simulations the Yee grid is a common choice because it conserves $\nabla \cdot \mathbf{B}$ in time–dependent simulations. One exemplary cell is shown in Fig. 5.1. Here particle densities are collected on the corners while the particles' velocities as well as the electric fields are lying on the edges. The magnetic fields are saved centered on each side of a cell. [Yee66]

The Yee grid is used in the placebo framework. Though in this thesis one–dimensional simulation are performed, the simulation domain is based on this

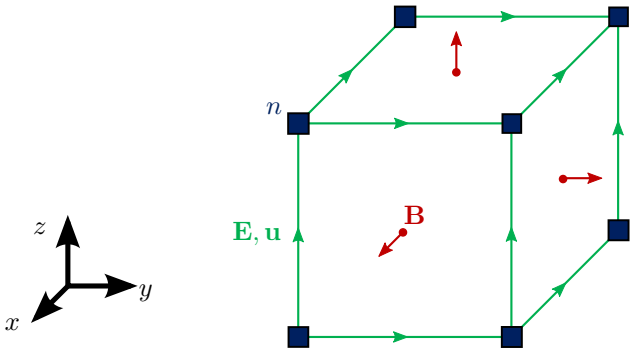

Figure 5.1: Scheme of a cell in the Yee grid. [Yee66]

type of grid to make it easier to transfer the findings of this thesis on a three–dimensional code.

The spatially limited simulation domain is additionally enclosed by so called ghost cells that act as a dump for the collected plasma quantities. The number of ghost cells is determined by the interaction length of the particles which is described by shape functions.

5.1.1 Shape functions

To collect the particle quantities on the discrete grid, so called weighting calculations are required, which are later used in reverse to compute the forces on each particle [BL85]. This weighting process draws upon so called shape functions. Recent algorithms are commonly based on b–splines which are presented in the following. [Lap]

The simplest type of weighting just sums up the particle's characteristics on the grid positions, which is also called nearest–grid–point weighting [BL85]. For this method, the first b–spline b_0 is the corresponding shape function

$$b_0(\xi) = \begin{cases} 1 & |\xi| < 0.5 \\ 0 & \text{other} \end{cases}$$

where $\xi = \frac{x - X_\mathrm{j}}{\Delta x}$ is the spatial coordinate, relative to the left side of grid cell j which has a length of Δx and is located at position X_j. Higher order weighting can be achieved by convolution

$$b_\mathrm{l}(\xi) = (b_{\mathrm{l}-1} * b_0)(\xi) = \int_{-\infty}^{\infty} b_{\mathrm{l}-1}(\xi') b_0(\xi - \xi')\, \mathrm{d}\xi'$$

which may be interpreted physically as a particle cloud of shape $b_{\mathrm{l}-1}$ passing

a rectangularly shaped grid cell described by the b_0–spline. Thus the next two higher order b–splines are

$$b_1(\xi) = (b_0 * b_0)(\xi) = \begin{cases} 1 - |\xi| & |\xi| < 1 \\ 0 & \text{other} \end{cases}$$

$$b_2(\xi) = (b_1 * b_0)(\xi) = \begin{cases} -\xi^2 + 0.75 & |\xi| < 0.5 \\ 0.5(|\xi| - 1.5)^2 & 0.5 < |\xi| < 1.5 \\ 0 & \text{other} \end{cases}$$

which are plotted together with the b_0–spline in Fig. 5.2. In terms of this understanding the b_1–spline describes the effect of a uniformly distributed particle cloud on a grid cell, whereas the b_2–spline considers a triangularly shaped cloud of particles. The use of higher order splines thus smooths the shape of the particle clouds and reduces noise on the collected quantities, however it requires more computation [BL85]. [Lap]

5.1.2 Exchange with grid

With the splines as defined above, the exchange between particles and grid can be performed. To collect the global quantities on the corresponding grid positions marked with j, namely ion particle and flux density as well as ion temperature, summation over the particles is required. Here, ions are marked with the index i from which α is the particle index.

$$(n_\mathrm{i})_\mathrm{j} = \frac{1}{\Delta x} \sum_\alpha b_\mathrm{l} \left(\frac{x_{\mathrm{i}\alpha} - X_\mathrm{j}}{\Delta x} \right)$$

$$(n_\mathrm{i}\mathbf{u}_\mathrm{i})_\mathrm{j} = \frac{1}{\Delta x} \sum_\alpha \mathbf{v}_{\mathrm{i}\alpha}\ b_\mathrm{l} \left(\frac{x_{\mathrm{i}\alpha} - X_\mathrm{j}}{\Delta x} \right)$$

$$(n_\mathrm{i}T_\mathrm{i})_\mathrm{j} = \frac{1}{\Delta x} \sum_\alpha (\mathbf{v}_{\mathrm{i}\alpha} - \mathbf{u}_\mathrm{ij})^2\ b_\mathrm{l} \left(\frac{x_{\mathrm{i}\alpha} - X_\mathrm{j}}{\Delta x} \right)$$

In reverse the quantities relevant for particle acceleration, like the electric field, are interpolated from the grid by summation.

$$E_\alpha = \sum_j E_j\ b_\mathrm{l} \left(\frac{X_j - x_{\mathrm{i}\alpha}}{\Delta x} \right)$$

Here, the same splines are used for collection and interpolation to preserve the shape of the particle clouds, which prevents gravitation–like instabilities and self–forces on the particles. [BL85]

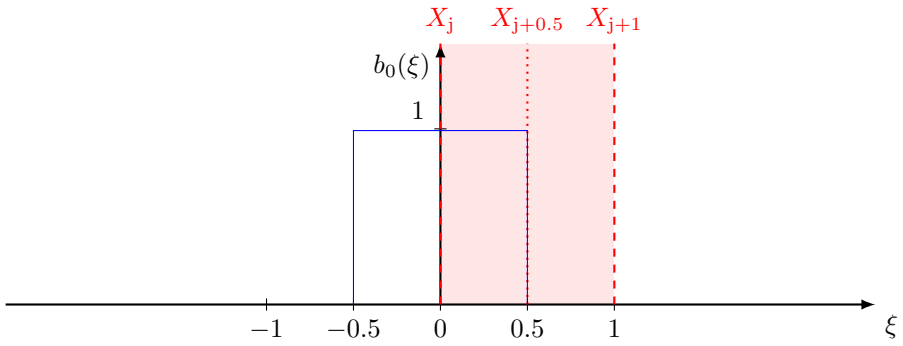

(a) b_0–spline.

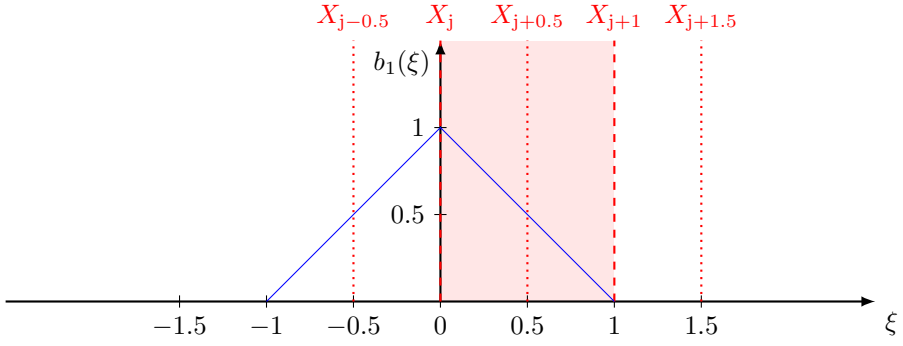

(b) b_1–spline.

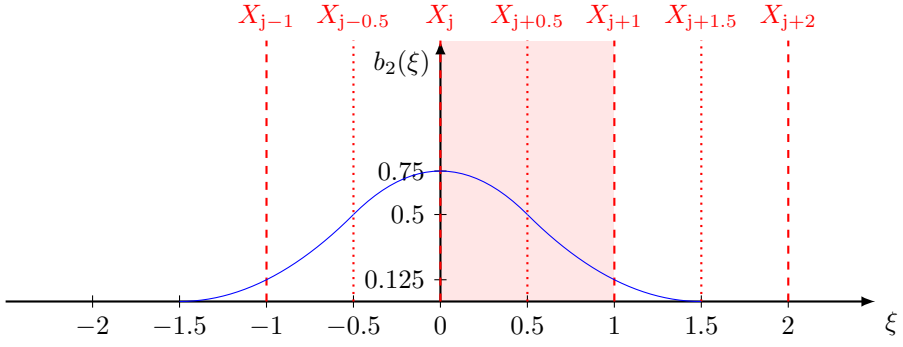

(c) b_2–spline.

Figure 5.2: Illustration of different order b–splines. The red highlighted area denotes the domain of the cell j. The red dashed lines mark the positions on which the collected quantities are saved and for which the particles inside cell j could have influence on, with the respective shape function. [BL85, Fig. 8.5a]

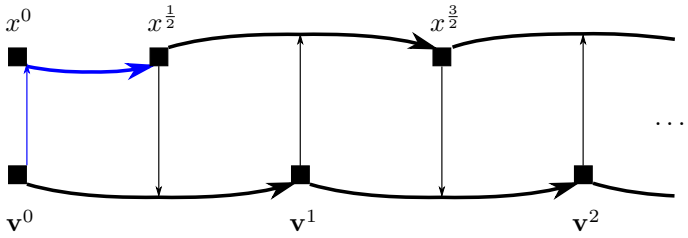

Figure 5.3: Leapfrog scheme with initial half–push of the particle positions, marked by the blue arrows.

5.2 Time evolution of particle quantities

For the numerical treatment of particle propagation, their equation of motion is rewritten into a set of differential equations of first order on which a Leapfrog scheme is applied that staggers the evolution of particle positions and velocities. Its discretized form in the one–dimensional formulation is

$$\begin{aligned} \frac{\mathbf{v}_{\mathrm{i}\alpha}^{n+1} - \mathbf{v}_{\mathrm{i}\alpha}^{n}}{\Delta t} &= \frac{Ze}{m_{\mathrm{i}}} \left[\mathbf{E}^{n+\frac{1}{2}} + \frac{\mathbf{v}_{\mathrm{i}\alpha}^{n+1} + \mathbf{v}_{\mathrm{i}\alpha}^{n}}{2} \times \mathbf{B} \right] \\ \frac{x_{\mathrm{i}\alpha}^{n+\frac{3}{2}} - x_{\mathrm{i}\alpha}^{n+\frac{1}{2}}}{\Delta t} &= v_{\mathrm{i}\alpha\mathrm{x}}^{n+1} \end{aligned} \tag{5.1}$$

where the upper index denotes the time step. To initialize the leapfrog scheme, a primary half–step is required. [BL85]

$$x^{\frac{1}{2}} = x^0 + \frac{\Delta t}{2} v_{\mathrm{x}}^0$$

Instead of solving the vector equation, a more simple algorithm will be used to update the particle velocities. For this case, the algorithm elaborated by Boris [Bor70] is the common choice. As sketched in Fig. 5.4, the particle propagation is separated in parts of **E**–field acceleration

$$\mathbf{v}_{\mathrm{i}\alpha}^{n} = \mathbf{v}_{\mathrm{i}\alpha}^{-} - \frac{\Delta t}{2} \frac{Ze}{m_{\mathrm{i}}} \mathbf{E} \qquad\qquad \mathbf{v}_{\mathrm{i}\alpha}^{n+1} = \mathbf{v}_{\mathrm{i}\alpha}^{+} + \frac{\Delta t}{2} \frac{Ze}{m_{\mathrm{i}}} \mathbf{E}$$

and **B**–field rotation, so that equation (5.1) becomes

$$\frac{\mathbf{v}_{\mathrm{i}\alpha}^{+} - \mathbf{v}_{\mathrm{i}\alpha}^{-}}{\Delta t} = \frac{Ze}{2m_{\mathrm{i}}} \left(\mathbf{v}_{\mathrm{i}\alpha}^{+} + \mathbf{v}_{\mathrm{i}\alpha}^{-} \right) \times \mathbf{B}.$$

$$\mathbf{v}_{\mathrm{i}\alpha}^{n} \xrightarrow{\mathbf{E}\text{–acceleration}} \underbrace{\mathbf{v}_{\mathrm{i}\alpha}^{-} \xrightarrow{\mathbf{B}\text{–rotation}} \mathbf{v}_{\mathrm{i}\alpha}^{+}}_{\frac{\mathbf{v}_{\mathrm{i}\alpha}^{n+1}+\mathbf{v}_{\mathrm{i}\alpha}^{n}}{2}=\frac{\mathbf{v}_{\mathrm{i}\alpha}^{+}+\mathbf{v}_{\mathrm{i}\alpha}^{-}}{2}} \xrightarrow{\mathbf{E}\text{–acceleration}} \mathbf{v}_{\mathrm{i}\alpha}^{n+1}$$

Figure 5.4: Illustration of the separated propagation in the Boris–scheme.

For small rotation angles θ, the following relation can be obtained by geometric interpretation of Fig. 5.5a.

$$\tan\left(\frac{\theta}{2}\right) = \frac{\left|\mathbf{v}_{\mathrm{i}\alpha,\perp}^{+} - \mathbf{v}_{\mathrm{i}\alpha,\perp}^{-}\right|}{\left|\mathbf{v}_{\mathrm{i}\alpha,\perp}^{+} + \mathbf{v}_{\mathrm{i}\alpha,\perp}^{-}\right|} = \frac{ZeB}{m_{\mathrm{i}}}\frac{\Delta t}{2}$$

With this relation two auxiliary vectors $\mathbf{t}$ and $\mathbf{v}'_{\mathrm{i}\alpha}$ are constructed from which the latter is perpendicular to $\mathbf{v}_{\mathrm{i}\alpha}^{+} - \mathbf{v}_{\mathrm{i}\alpha}^{-}$

$$\mathbf{t} = \tan\left(\frac{\theta}{2}\right)\widehat{\mathbf{B}} = \frac{Ze\mathbf{B}}{m_{\mathrm{i}}}\frac{\Delta t}{2} \qquad\qquad \mathbf{v}'_{\mathrm{i}\alpha} = \mathbf{v}_{\mathrm{i}\alpha}^{-} + \mathbf{v}_{\mathrm{i}\alpha}^{-} \times \mathbf{t}$$

where $\widehat{\mathbf{B}}$ is the unit vector in direction of $\mathbf{B}$. Thereby $\mathbf{v}'_{\mathrm{i}\alpha} \times \mathbf{B}$ is parallel to $\mathbf{v}_{\mathrm{i}\alpha}^{+} - \mathbf{v}_{\mathrm{i}\alpha}^{-}$ so that the final velocity $\mathbf{v}_{\mathrm{i}\alpha}^{+}$ after gyration is calculated by

$$\mathbf{v}_{\mathrm{i}\alpha}^{+} = \mathbf{v}_{\mathrm{i}\alpha}^{-} + \mathbf{v}'_{\mathrm{i}\alpha} \times \mathbf{s}$$

where $\mathbf{s}$ is a resized version of $\mathbf{t}$ that ensures conservation of the absolute values of velocities $\left|\mathbf{v}_{\mathrm{i}\alpha}^{+}\right| = \left|\mathbf{v}_{\mathrm{i}\alpha}^{-}\right|$ thus granting stability. [BL85]

$$\mathbf{s} = \sin(\theta)\,\widehat{\mathbf{B}} = \frac{2\mathbf{t}}{1+t^2}$$

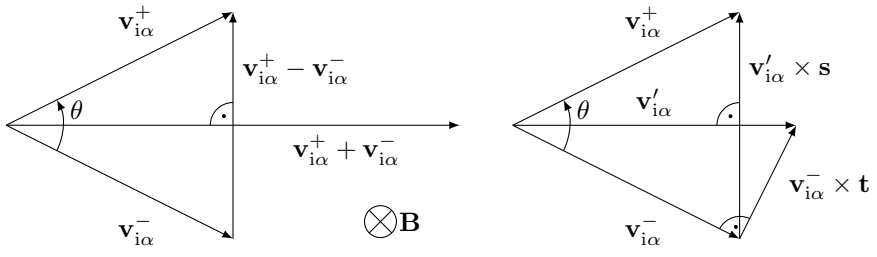

(a) Rotation from $\mathbf{v}_{\mathrm{i}\alpha}^{-}$ to $\mathbf{v}_{\mathrm{i}\alpha}^{+}$.

(b) Construction of rotation.

Figure 5.5: Graphical support to understand the Boris algorithm showing the rotation from $\mathbf{v}_{\mathrm{i}\alpha}^{-}$ to $\mathbf{v}_{\mathrm{i}\alpha}^{+}$ projected on a plane perpendicular to $\mathbf{B}$. [BL85, Fig. 4.3a & Fig. 4.4a]

5.3 Ionization and plasma–wall–interactions

As already stated in chapter 3, the hybrid simulation connects particle losses at the walls directly with the ionization sources. Superparticles are flagged as impeding a wall as soon as they reach a ghost cell. In the subsequent time step they will be removed and reinserted in the ionization domain according to one selected probability distribution function from section 3.2. Depending on whether ionization from a resting or comoving neutral gas background is specified, the flagged particles are reset with zero or average velocity as collected from grid in the previous time step.

Since only a rather small number of superparticles compared to natural occurring plasmas is considered in simulation, ionization reveals a source of noise in the collected quantities since not a single particle but rather a whole cloud of particles will be added to the domain. It was considered to counteract this effect by smoothing the ion density in each time step, but it was waived since it changes the final results dramatically, insofar as some of the observed kinetic effects were suppressed.

5.4 Application of Bohm forcing

The algorithms forcing the Bohm criterion as described in section 2.2 have been transfered to the one–dimensional hybrid simulations which ensures that the particles leaving the domain reach Bohm velocity. Interestingly when omitting these methods, simulations yield the same results. Thus a different way of interpreting plasma–wall interactions is provided in the following chapter on which the simulation of this thesis rely.

Chapter 6

Interpretation of walls as the cause for shocks

In the hybrid simulations as described in the previous chapter 5, the Bohm criterion seems to be automatically fulfilled, since particles are leaving the domain with Bohm velocity v_B without imposing any boundary condition at all. Only the removal of ions in the ghost cells seems to cause this effect, which leads to the assumption that a different kind of physical mechanism is presumably taking place. In this context, the occurring process is recognized by the buildup of discontinuities in the plasma quantities due to the presence of walls, thus interpreting the plasma–wall transition in a new manner as a stationary shock.

In this chapter, explanations to support this proposition are carried out with jump conditions. Firstly, investigations are considered in the electrostatic case, resulting in Rankine–Hugoniot conditions, and are then generalized on magnetic fields.

6.1 Jump conditions

6.1.1 Jump conditions in the absence of magnetic fields

In order to derive proper jump conditions, the ion mass transport equation (4.1) is considered as well as the total momentum balance equation (4.7). In the proposed model from chapter 3, no ionization is assumed in front of the walls yielding vanishing source densities. Since the electrostatic case is considered here, the magnetic field is omitted, so that the basic equations for the following examination are

$$\nabla \cdot (n_\mathrm{i} \mathbf{u}_\mathrm{i}) = 0, \qquad \nabla \cdot (n_\mathrm{i} \mathbf{u}_\mathrm{i} \mathbf{u}_\mathrm{i}) = -c_\mathrm{s}^2 (\nabla n_\mathrm{i}).$$

Here, it is sufficient to consider only the velocity component in parallel direction of the surface normal $\widehat{\mathbf{n}} = \widehat{\mathbf{e}}_\mathrm{x}$ because the other components are not influenced by any force in the one–dimensional model and are thus constants.

$$\partial_\mathrm{x}(n_\mathrm{i} u_\mathrm{ix}) = 0 \qquad\qquad \partial_\mathrm{x}(n_\mathrm{i} u_\mathrm{ix}^2) + c_\mathrm{s}^2(\partial_\mathrm{x} n_\mathrm{i}) = 0$$

Integrating these two equations in a small domain around the modeled position of the sheath edge at $x = x_2$ yields a set of two equations, which can be rearranged to find the ratios of adjacent values of density and velocity respectively.

$$\int_{x_\mathrm{l}}^{x_\mathrm{r}} \partial_\mathrm{x}(n_\mathrm{i} u_\mathrm{ix})\,\mathrm{d}x = n_\mathrm{r} u_\mathrm{r} - n_\mathrm{l} u_\mathrm{l} = 0$$

$$\int_{x_\mathrm{l}}^{x_\mathrm{r}} \left[\partial_\mathrm{x}(n_\mathrm{i} u_\mathrm{ix}^2) + c_\mathrm{s}^2(\partial_\mathrm{x} n_\mathrm{i})\right]\,\mathrm{d}x = n_\mathrm{r} u_\mathrm{r}^2 + c_\mathrm{s}^2 n_\mathrm{r} - n_\mathrm{l} u_\mathrm{l}^2 - c_\mathrm{s}^2 n_\mathrm{l} = 0$$

where the following quantities are introduced for convenience for small lengths ϵ.

$$x_\mathrm{r} \coloneqq x_2 + \epsilon \qquad\qquad x_\mathrm{l} \coloneqq x_2 - \epsilon$$

$$u_\mathrm{r} \coloneqq u_\mathrm{ix}(x_\mathrm{r}) \qquad u_\mathrm{l} \coloneqq u_\mathrm{ix}(x_\mathrm{l}) \qquad n_\mathrm{r} \coloneqq n_\mathrm{i}(x_\mathrm{r}) \qquad n_\mathrm{l} \coloneqq n_\mathrm{i}(x_\mathrm{l})$$

A common representation of these equations is

$$[n_\mathrm{i} u_\mathrm{ix}]_\mathrm{l}^r = 0 \qquad\qquad \left[n_\mathrm{i} u_\mathrm{ix}^2 + c_\mathrm{s}^2 n_\mathrm{i}\right]_\mathrm{l}^r = 0 \tag{6.1}$$

where $[f]_\mathrm{l}^r = f_\mathrm{r} - f_\mathrm{l}$ is a usual notation with f an arbitrary expression.

The latter expression yields a quadratic equation in u_r after elimination of the density in terms of the former one

$$u_\mathrm{r}^2 - u_\mathrm{r}\left(\frac{c_\mathrm{s}^2}{u_\mathrm{l}} - u_\mathrm{l}\right) + c_\mathrm{s}^2 = 0$$

so that the solution of this set of equations becomes

$$u_\mathrm{r} = \frac{1}{2}\left[\frac{c_\mathrm{s}^2}{u_\mathrm{l}} + u_\mathrm{l} \pm \left(\frac{c_\mathrm{s}^2}{u_\mathrm{l}} - u_\mathrm{l}\right)\right] \in \left\{\frac{c_\mathrm{s}^2}{u_\mathrm{l}}, u_\mathrm{l}\right\} \qquad\qquad \frac{n_\mathrm{l}}{n_\mathrm{r}} = \frac{u_\mathrm{r}}{u_\mathrm{l}} \in \left\{\frac{c_\mathrm{s}^2}{u_\mathrm{l}^2}, 1\right\}.$$

The second set of solutions represents the trivial, constant solution whereas the first set describes a discontinuity in both velocity and density.

In simulation smooth profiles of the plasma quantities are observed. The two branches of the solutions on each side of the sheath edge are only merging in terms of the above presented explanations if $u_\mathrm{r} = u_\mathrm{l} = c_\mathrm{s}$ is fulfilled, thus forcing a discontinuity by removing particles at the domain border automatically conforms to the Bohm criterion.

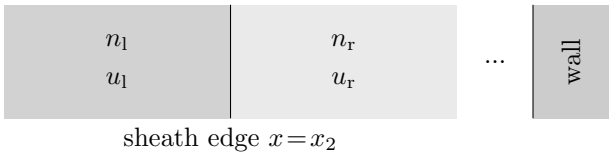

Figure 6.1: Sketch of a electrostatic sheath interpreted as a discontinuous stream.

6.1.2 Jump conditions with magnetic fields

The jump conditions for the electrostatic case provide a possible explanation for the fulfillment of the Bohm criterion, which may justify the generalization on jump conditions for arbitrary magnetic fields. Considering Ampère's law

$$\nabla \times \mathbf{B} = \mu_0 \mathbf{j} = \mu_0 Z e n_\mathrm{i} \left(\mathbf{u}_\mathrm{i} - \mathbf{u}_\mathrm{e} \right)$$

and further applying the vector identity

$$(\nabla \times \mathbf{B}) \times \mathbf{B} = \nabla \cdot (\mathbf{B}\mathbf{B}) - \nabla \cdot \left(\frac{B^2}{2} \right),$$

the total momentum balance equation (4.6) reads

$$\nabla \cdot \left[m_\mathrm{i} n_\mathrm{i} \mathbf{u}_\mathrm{i} \mathbf{u}_\mathrm{i} + m_\mathrm{i} c_\mathrm{s}^2 n_\mathrm{i} \mathbb{1} - \frac{1}{\mu_0} \left(\mathbf{B}\mathbf{B} - \frac{B^2}{2} \mathbb{1} \right) \right] = 0$$

in the ionization–free border region, where $\mathbf{s}_\mathrm{p} = 0$ applies. This equation is similar to the momentum equation of ideal magnetohydrodynamics in the stationary case ($\partial_\mathrm{t} = 0$). Additionally considering the mass transport equation and boundary conditions on the electric and the magnetic field, respectively, the jump conditions can be set up. [BS03]

$$\begin{aligned}
\left[n_\mathrm{i} \mathbf{u}_\mathrm{i} \cdot \widehat{\mathbf{n}} \right]_\mathrm{l}^r &= 0 \\
\left[m_\mathrm{i} n_\mathrm{i} \mathbf{u}_\mathrm{i} \left(\mathbf{u}_\mathrm{i} \cdot \widehat{\mathbf{n}} \right) + \left(m_\mathrm{i} c_\mathrm{s}^2 n_\mathrm{i} + \frac{B^2}{2\mu_0} \right) \widehat{\mathbf{n}} - \left(\mathbf{B} \cdot \widehat{\mathbf{n}} \right) \frac{\mathbf{B}}{\mu_0} \right]_\mathrm{l}^r &= 0 \\
\left[\mathbf{B} \cdot \widehat{\mathbf{n}} \right]_\mathrm{l}^r &= 0 \\
\left[\widehat{\mathbf{n}} \times \mathbf{E} \right]_\mathrm{l}^r &= 0
\end{aligned}$$

In the presented one–dimensional model with $\widehat{\mathbf{n}} = \widehat{\mathbf{e}}_{\mathrm{x}}$, the induced magnetic field is neglected compared to the external, constant magnetic field. Furthermore, the electric field is designed to be constant in y– and z–direction, so that the above presented jump conditions reduce to the ones from the electrostatic case presented in equation (6.1), thus yielding the same results.

$$[n_{\mathrm{i}} u_{\mathrm{ix}}]_{\mathrm{l}}^{r} = 0 \qquad\qquad \left[n_{\mathrm{i}} u_{\mathrm{ix}}^2 + c_{\mathrm{s}}^2 n_{\mathrm{i}}\right]_{\mathrm{l}}^{r} = 0$$

Chapter 7

Comparison of hybrid and fluid results

Up to this point, the fundamental system of differential equations for the two–fluid model (4.10), (4.11), (4.12) is provided with different ionization models from chapter 3. In this section, solutions for these equations are compared with the hybrid simulation results for different magnetic fields and source densities. The differential equations are going to be simplified as much as possible, so that an analytical solution is achievable in some cases.

In the beginning of each of the following sections, the equations are analyzed without any sources, which corresponds to the border region in which no ionization takes place. For the examination of the ionization domain, these terms are included, so that the whole domain can then be described. Afterwards these combined solutions are compared with the simulation results using proper boundary conditions which are read out from the corresponding simulations.

7.1 Considering the absence of magnetic fields

7.1.1 Analytic fluid approach

Without magnetic field the x–component of the momentum balance (4.10) becomes

$$\left(u_{\mathrm{ix}} - \frac{c_{\mathrm{s}}^2}{u_{\mathrm{ix}}}\right) \partial_{\mathrm{x}} u_{\mathrm{ix}} = \frac{u_{\mathrm{ix}}}{(n_{\mathrm{i}} u_{\mathrm{ix}})_0 + S_{\mathrm{n}}} \left(s_{\mathrm{px}} - s_{\mathrm{n}} \left(u_{\mathrm{ix}} + \frac{c_{\mathrm{s}}^2}{u_{\mathrm{ix}}}\right)\right) \ .$$

Omitting both source terms to describe the border region, the above equation is only solved by constant solutions in u_{ix}.

$$\left(u_{\mathrm{ix}} - \frac{c_{\mathrm{s}}^2}{u_{\mathrm{ix}}}\right) \partial_{\mathrm{x}} u_{\mathrm{ix}} = 0$$

For $u_{\mathrm{ix}} = c_{\mathrm{s}}$ the equation becomes singular. Since the border region is in contact with the wall, this specific solution fulfills the Bohm criterion from chapters 2 and 6, respectively, which will be used as a boundary condition for the ionization region in the upcoming part.

Fluid approach without momentum source

Leaving out the momentum source density $\mathbf{s}_{\mathrm{p}} = 0$ and thus assuming ionization from resting neutral gas the momentum balance reduces to

$$\left(u_{\mathrm{ix}} - \frac{c_{\mathrm{s}}^2}{u_{\mathrm{ix}}}\right) \partial_{\mathrm{x}} u_{\mathrm{ix}} = \frac{-s_{\mathrm{n}}(u_{\mathrm{ix}}^2 + c_{\mathrm{s}}^2)}{(n_{\mathrm{i}} u_{\mathrm{ix}})_0 + S_{\mathrm{n}}} \quad \Leftrightarrow \quad \frac{u_{\mathrm{ix}} - \frac{c_{\mathrm{s}}^2}{u_{\mathrm{ix}}}}{u_{\mathrm{ix}}^2 + c_{\mathrm{s}}^2} \partial_{\mathrm{x}} u_{\mathrm{ix}} = \frac{-s_{\mathrm{n}}}{(n_{\mathrm{i}} u_{\mathrm{ix}})_0 + S_{\mathrm{n}}} \ .$$

Integration from inside the ionization domain to its border yields

$$\int_x^{x_1} \frac{u_{\mathrm{ix}} - \frac{c_{\mathrm{s}}^2}{u_{\mathrm{ix}}}}{u_{\mathrm{ix}}^2 + c_{\mathrm{s}}^2} \partial_{\mathrm{x}} u_{\mathrm{ix}} \, \mathrm{d}x = \int_x^{x_1} \frac{-s_{\mathrm{n}}(x')}{(n_{\mathrm{i}} u_{\mathrm{ix}})_0 + S_{\mathrm{n}}(x')} \, \mathrm{d}x' \ .$$

Both integrals can be solved by substitution and further inserting the continuity condition from equation (3.12) yields a quadratic equation that can be solved.

$$\ln\left(\frac{u_{\mathrm{ix}} + \frac{c_{\mathrm{s}}^2}{u_{\mathrm{ix}}}}{u_{\mathrm{ix1}} + \frac{c_{\mathrm{s}}^2}{u_{\mathrm{ix1}}}}\right) = \ln\left(\frac{(n_{\mathrm{i}} u_{\mathrm{ix}})_0 + S_{\mathrm{n}}(x_1)}{(n_{\mathrm{i}} u_{\mathrm{ix}})_0 + S_{\mathrm{n}}(x)}\right) = \ln\left(\frac{(n_{\mathrm{i}} u_{\mathrm{ix}})_1}{(n_{\mathrm{i}} u_{\mathrm{ix}})_0 + S_{\mathrm{n}}(x)}\right)$$

$$\Leftrightarrow \qquad u_{\mathrm{ix}} + \frac{c_{\mathrm{s}}^2}{u_{\mathrm{ix}}} = \frac{(n_{\mathrm{i}} u_{\mathrm{ix}})_1 \left(u_{\mathrm{ix1}} + \frac{c_{\mathrm{s}}^2}{u_{\mathrm{ix1}}}\right)}{(n_{\mathrm{i}} u_{\mathrm{ix}})_0 + S_{\mathrm{n}}(x)} \quad =: \quad p(x)$$

$$\Leftrightarrow \quad u_{\mathrm{ix}}^2 - p(x) u_{\mathrm{ix}} + c_{\mathrm{s}}^2 = 0$$

$$\Leftrightarrow \qquad u_{\mathrm{ix}}(x) = \frac{p(x)}{2} \pm \sqrt{\frac{p^2(x)}{4} - c_{\mathrm{s}}^2}$$

The solution with the upper sign runs into a singularity, if the denominator of $p(x)$ becomes zero. The corresponding density profile can be obtained by inserting the velocity profile in the integrated mass transport equation (4.9).

$$
\begin{aligned}
n_\mathrm{i}(x) &= \frac{(n_\mathrm{i}u_\mathrm{ix})_0 + S_\mathrm{n}(x)}{u_\mathrm{ix}(x)} = \frac{(n_\mathrm{i}u_\mathrm{ix})_0 + S_\mathrm{n}(x)}{\frac{p(x)}{2} \pm \sqrt{\frac{p(x)^2}{4} - c_\mathrm{s}^2}} \\
&= ((n_\mathrm{i}u_\mathrm{ix})_0 + S_\mathrm{n}(x)) \frac{\frac{p(x)}{2} \mp \sqrt{\frac{p(x)^2}{4} - c_\mathrm{s}^2}}{\frac{p(x)^2}{4} - \left(\frac{p(x)^2}{4} - c_\mathrm{s}^2\right)} \\
&= \frac{(n_\mathrm{i}u_\mathrm{ix})_0 + S_\mathrm{n}(x)}{c_\mathrm{s}^2} \left(\frac{p(x)}{2} \mp \sqrt{\frac{p(x)^2}{4} - c_\mathrm{s}^2}\right)
\end{aligned}
$$

This representation of u_ix and n_i switches signs when passing $x_0 = 0$, thus combining both solutions from the quadratic equation. This can be corrected by matching both branches to one specific type of solution with the following modification.

$$
\begin{aligned}
u_\mathrm{ix}(x) &= \frac{p(x)}{2} \pm \mathrm{sign}(p(x)) \sqrt{\frac{p(x)^2}{4} - c_\mathrm{s}^2} \\
n_\mathrm{i}(x) &= \frac{(n_\mathrm{i}u_\mathrm{ix})_0 + S_\mathrm{n}(x)}{c_\mathrm{s}^2} \left(\frac{p(x)}{2} \mp \mathrm{sign}(p(x)) \sqrt{\frac{p(x)^2}{4} - c_\mathrm{s}^2}\right)
\end{aligned}
$$

These equations still contain both solutions from the quadratic equation. Obviously only the one with the lower sign represents the model, because it reproduces the acceleration to the walls and the increase in density in the domain center caused by ionization. Thus the other one will be discarded for the remaining part of this section.

Continuing the ion sound velocity from the border region according to the foregoing section and considering the symmetry of the profiles, two boundary conditions can be specified.

$$
u_\mathrm{ix1} = c_\mathrm{s} \qquad \text{and} \qquad (n_\mathrm{i}u_\mathrm{ix})_0 = 0 \tag{7.1}
$$

The remaining one $(n_\mathrm{i}u_\mathrm{ix})_1$ will be obtained from simulation. Now density and velocity profiles can be written in their final form as

$$
\begin{aligned}
u_\mathrm{ix}(x) &= c_\mathrm{s} \left(\frac{(n_\mathrm{i}u_\mathrm{ix})_1}{S_\mathrm{n}(x)} - \mathrm{sign}(S_\mathrm{n}(x)) \sqrt{\left(\frac{(n_\mathrm{i}u_\mathrm{ix})_1}{S_\mathrm{n}(x)}\right)^2 - c_\mathrm{s}^2}\right) \\
&= \frac{(n_\mathrm{i}u_\mathrm{ix})_1 c_\mathrm{s}}{S_\mathrm{n}(x)} \left(1 - \mathrm{sign}((n_\mathrm{i}u_\mathrm{ix})_1) \sqrt{1 - \left(\frac{S_\mathrm{n}(x) c_\mathrm{s}}{(n_\mathrm{i}u_\mathrm{ix})_1}\right)^2}\right) \qquad (7.2) \\
n_\mathrm{i}(x) &= \frac{S_\mathrm{n}(x)}{c_\mathrm{s}} \left(\frac{(n_\mathrm{i}u_\mathrm{ix})_1}{S_\mathrm{n}(x)} + \mathrm{sign}(S_\mathrm{n}(x)) \sqrt{\left(\frac{(n_\mathrm{i}u_\mathrm{ix})_1}{S_\mathrm{n}(x)}\right)^2 - 1}\right) \\
&= \frac{(n_\mathrm{i}u_\mathrm{ix})_1}{c_\mathrm{s}} \left(1 + \mathrm{sign}((n_\mathrm{i}u_\mathrm{ix})_1) \sqrt{1 - \left(\frac{S_\mathrm{n}(x)}{(n_\mathrm{i}u_\mathrm{ix})_1}\right)^2}\right). \qquad (7.3)
\end{aligned}
$$

To obtain the shape of the profiles the integrated ionization source density S_n has to be specified. The results for the constant source density as specified in equation (3.5) are plotted in Fig. 7.1. It is worth mentioning that the density profile becomes a semicircle here. The same is displayed for the raised cosine source density from equation (3.6) in Fig. 7.2.

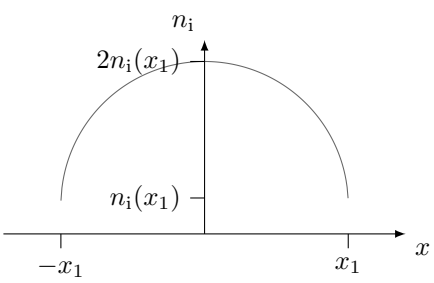

(a) Ion density $n_\mathrm{i}(x)$.

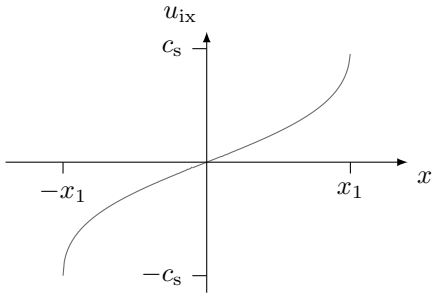

(b) Ion velocity $u_\mathrm{ix}(x)$.

Figure 7.1: Density and velocity profiles for the case without magnetic field and momentum source. Ionization is described by the constant distribution. The boundary conditions from equation (7.1) are applied. Solution without singularities at the domain center is chosen.

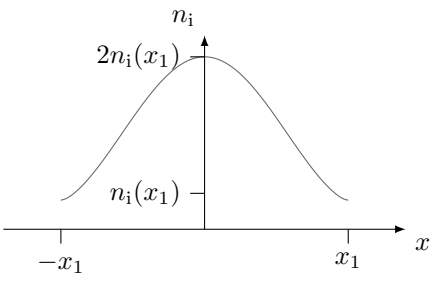

(a) Ion density $n_\mathrm{i}(x)$.

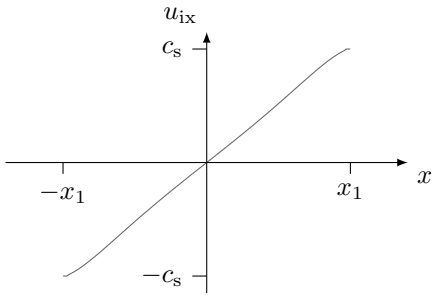

(b) Ion velocity $u_\mathrm{ix}(x)$.

Figure 7.2: Density and velocity profiles for the case without magnetic field and momentum source. Ionization is described by the raised cosine distribution. The boundary conditions from equation (7.1) are applied. Solution without singularities at the domain center is chosen.

Fluid approach with both ionization and momentum source

Considering ionization from a comoving gas background yields a momentum source density of $\mathbf{s}_\mathrm{p} = s_\mathrm{n}\mathbf{u}$ that reduces the momentum balance (4.10) to

$$\left(u_\mathrm{ix} - \frac{c_\mathrm{s}^2}{u_\mathrm{ix}}\right)\partial_\mathrm{x} u_\mathrm{ix} = \frac{-s_\mathrm{n}c_\mathrm{s}^2}{(n_\mathrm{i}u_\mathrm{ix})_0 + S_\mathrm{n}}.$$

Just as in the previous section, this expression is integrated from inside the ionization domain to its border and is simplified with the continuity condition (3.12).

$$\begin{aligned}
&\int_x^{x_1}\left(u_\mathrm{ix} - \frac{c_\mathrm{s}^2}{u_\mathrm{ix}}\right)\partial_\mathrm{x} u_\mathrm{ix}\,\mathrm{d}x = \int_x^{x_1}\frac{-s_\mathrm{n}(x')c_\mathrm{s}^2}{(n_\mathrm{i}u_\mathrm{ix})_0 + S_\mathrm{n}(x')}\,\mathrm{d}x' \\
\Leftrightarrow\quad &\frac{u_\mathrm{ix}^2}{2} - \frac{u_\mathrm{ix1}^2}{2} + c_\mathrm{s}^2\ln\left(\frac{u_\mathrm{ix1}}{u_\mathrm{ix}}\right) = c_\mathrm{s}^2\ln\left(\frac{(n_\mathrm{i}u_\mathrm{ix})_0 + S_\mathrm{n}(x_1)}{(n_\mathrm{i}u_\mathrm{ix})_0 + S_\mathrm{n}(x)}\right) \\
\Leftrightarrow\quad &\frac{u_\mathrm{ix}^2}{2} + c_\mathrm{s}^2\ln\left(\frac{u_\mathrm{ix1}}{u_\mathrm{ix}}\right) = \frac{u_\mathrm{ix1}^2}{2} + c_\mathrm{s}^2\ln\left(\frac{(n_\mathrm{i}u_\mathrm{ix})_1}{(n_\mathrm{i}u_\mathrm{ix})_0 + S_\mathrm{n}(x)}\right)
\end{aligned}$$

The result is an implicit equation. However spatial profiles of ion fluid velocity and density can be received by integrating the corresponding differential equation numerically.

7.1.2 Hybrid simulation results

Up to this point, the momentum balance without a magnetic field for different source densities has been solved analytically. Now simulations with the hybrid model from chapter 4.2 are performed for comparison. Before showing and discussing the simulation results, the used simulation parameters are provided as well as how the plasma is initialized. These parameters, if not specified else, are applied on the other simulation runs with magnetic fields, too.

Splines of second order are used to collect and distribute moments which imply two ghost cells on each side of the domain. Each cell except for the ghost cells is initialized with a specific amount of equally spaced particles, so that the simulation starts at a homogeneous density $n = \mathring{n}$ and zero velocity $\mathbf{u}_\mathrm{i} = 0$. The amount of cells is set to $N_\mathrm{cells} = 600$ which provides a decent resolution of the collected moments in the domain. The number of particles per cell needs to be sufficiently large to reproduce the complex dynamics of plasmas correctly, but without wasting computational resources. As a decision support, a comparison of simulation runs is provided in Fig. 7.3 in which this

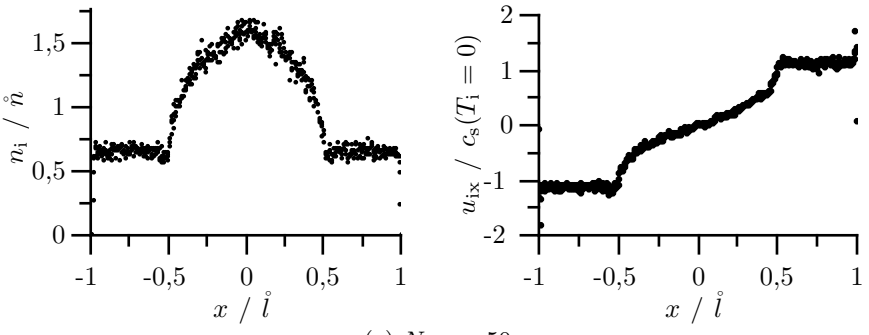

(a) $N_{\mathrm{p/c}} = 50$

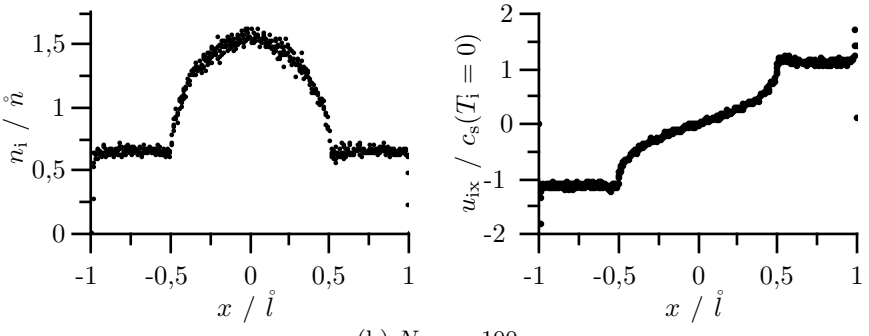

(b) $N_{\mathrm{p/c}} = 100$

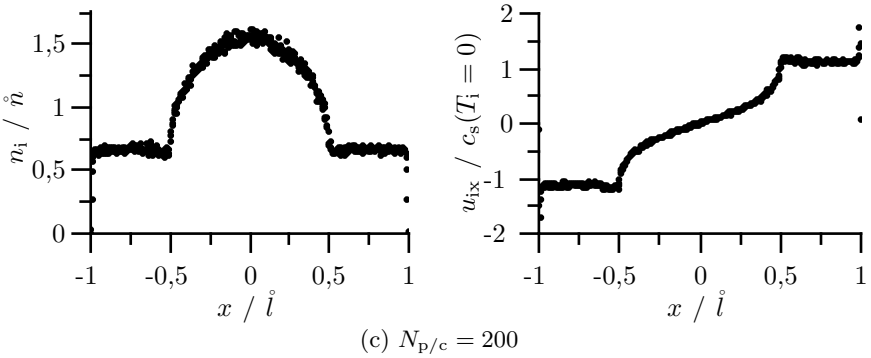

(c) $N_{\mathrm{p/c}} = 200$

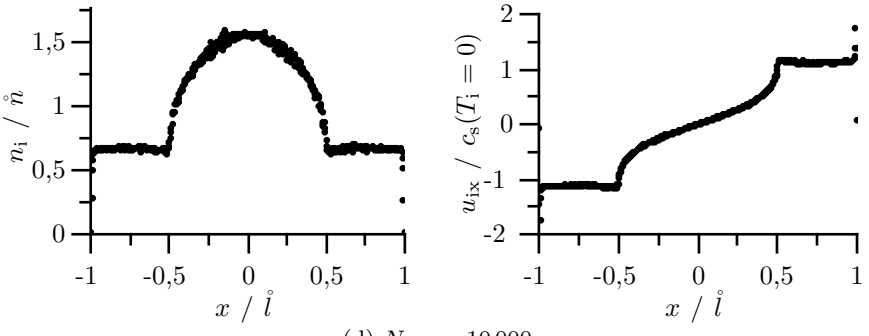

(d) $N_{\mathrm{p/c}} = 10\,000$

Figure 7.3: Ion density n_i and velocity u_ix profiles for different numbers of particles per cell $N_{\mathrm{p/c}}$. The simulation parameters are set to $B = 0$, $\widehat{\nu}_\mathrm{ie} = 0$, $s_\mathrm{n} = A f_\mathrm{cd}(x)$, $\mathbf{s}_\mathrm{p} = 0$.

parameter is varied. This sample configuration corresponds to the case without magnetic fields, momentum sources and collisions with a constant ionization source density s_n for which analytic profiles have been derived in the fluid model (see Fig. 7.1). The results will be discussed later in detail. The profiles in Fig. 7.3a and Fig. 7.3b appear to be quite noisy, but there is not much of a difference between the simulation results from Fig. 7.3c and 7.3d, so that the parameters concerning the amount of particles are set to those corresponding to the former case.

$$N_\mathrm{cells} = 600,\ N_\mathrm{particles/cell} = 200 \qquad \Rightarrow \qquad N_\mathrm{particles} = 119\,200.$$

The size of the ionization domain is chosen to be half the complete domain, whose size is arbitrarily set to one, so that the width of each cell Δx becomes

$$x_1 = 0.5,\ x_2 = 1 \qquad \Rightarrow \qquad \Delta x = \frac{2x_2}{N_\mathrm{cells}} = \frac{1}{300}.$$

Due to the extent of the upcoming investigations, it is waived here to examine cases with non–vanishing electric fields E_y, E_z and wall current densities j_w.

$$E_\mathrm{y} = 0 \qquad E_\mathrm{z} = 0 \qquad j_\mathrm{w} = 0$$

Since now the simulation parameters are specified, the simulations can be performed and their results will be examined in the following. In Fig. 7.4 the results of a simulation run are displayed in which the ionization source density s_n is constant. In addition, no collisions or momentum sources are taken into account. The displayed results are the collected moments out of the simulation domain. Thus each data point corresponds to one specific cell. Since there are two ghost cells on each side and the second order spline function has a width of three cells, the last five cells of each plot do not have any physical meaning and are thus accounted as numerical artifacts. The continuous lines correspond to the numerical integration of the two–fluid equations as discussed in the previous part of this chapter.

The shapes of both simulation and two–fluid results are similar. However, the simulation result for the ion velocity exceeds the two–fluid solution in the border region of the domain. The opposite is true for the ion density. Taking a look at the temperature provides an explanation because the ion temperature is not zero as assumed in the two–fluid solution. Inserting particles with zero velocity yields a broadening of the ion velocity distribution and therefore an increase of their temperature, that also affects the sound velocity in the border region on which the ions are accelerated.

To counteract the temperature rise, simulations with electron–ion collisions have been performed whose results are provided in Fig. 7.5. In the border region, it is observable that the ion temperature decreases towards the walls. However, due to ionization from a resting gas background and thus supplying ions with zero momentum, the ion temperature still differs from zero in the ionization region.

Another approach to prevent any increase of the ion temperature is to include the momentum source term as discussed in chapter 3 since the ions are inserted with their average velocity here. Both profiles of simulation and fluid model are in agreement as shown in Fig. 7.6 although they appear more noisy compared to the case without any momentum source. The ion temperature still differs from zero in the ionization region, though.

To check whether the discontinuous ionization source density s_n, as used until now, has any effect on the accordance of the simulation and fluid profiles, simulations have been performed with a smooth raised cosine ionization source density s_n with similar simulation parameters. Their results are displayed in Fig. 7.7 to 7.9. In comparison to the previous simulation runs, similar statements about the profiles in terms of temperatures are possible. However, for the raised cosine source density it does not appear that both fluid and simulation results seem to be in better agreement in comparison to the constant source density. This allows the conclusion that the continuity of the ionization source density does not seem to have any influence on the difference between the hybrid simulation and fluid results.

Table 7.1: Overview of the set of parameters for the presented results in the absence of magnetic fields.

B	$\widehat{\nu}_\mathrm{ie}$	s_n	$\mathbf{s}_\mathrm{p}$	Figure
0	0	Af_cd	0	7.4
0	1	Af_cd	0	7.5
0	0	Af_cd	$s_\mathrm{n}\mathbf{u}$	7.6
0	0	Af_rcd	0	7.7
0	1	Af_rcd	0	7.8
0	0	Af_rcd	$s_\mathrm{n}\mathbf{u}$	7.9

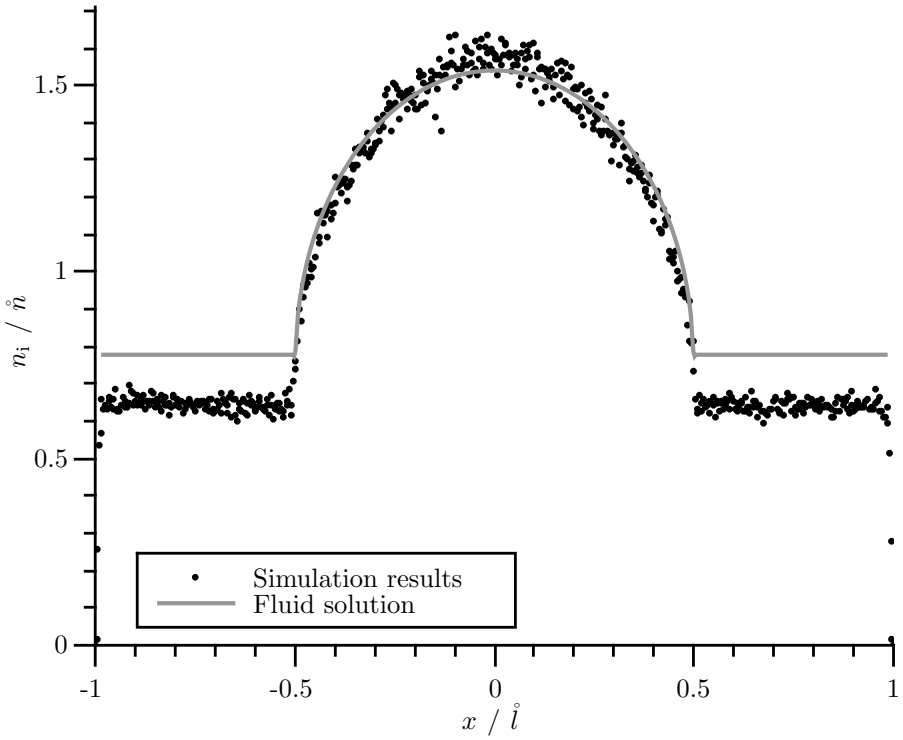

(a) Ion density n_i.

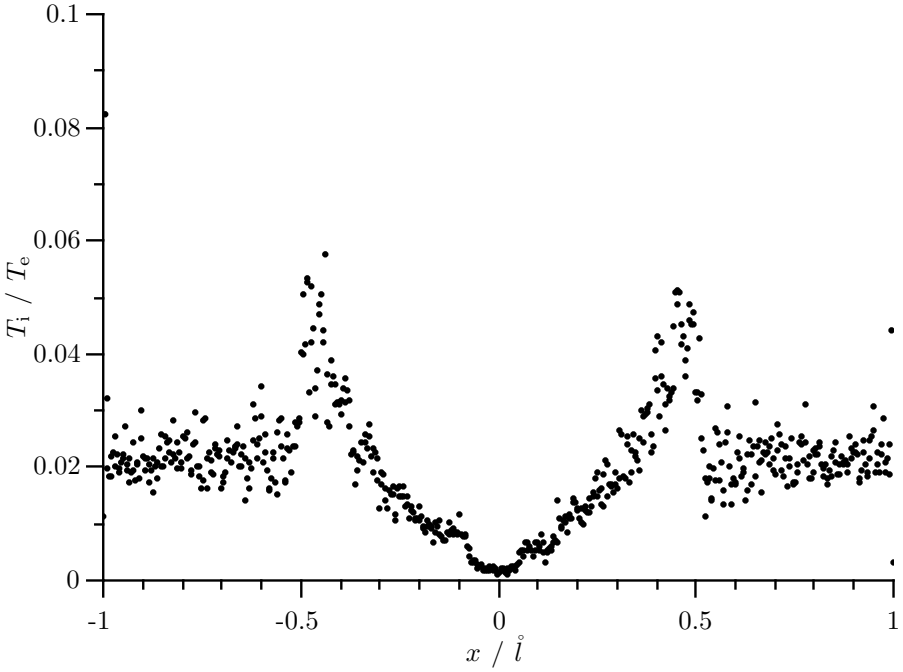

(b) Ion temperature T_i normalized on constant electron temperature T_e.

Figure 7.4: Comparison of profiles from numerical integration of fluid equations with hybrid simulation results with $B = 0,\ \widehat{\nu}_\mathrm{ie} = 0,\ s_\mathrm{n} = Af_\mathrm{cd}(x),\ \mathbf{s}_\mathrm{p} = 0$. For the fluid solution the following boundary conditions were used $n_0 = 1.54,\ u_\mathrm{ix0} = 10^{-6},\ (n_\mathrm{i}u_\mathrm{ix})_1 = 0.7735$.

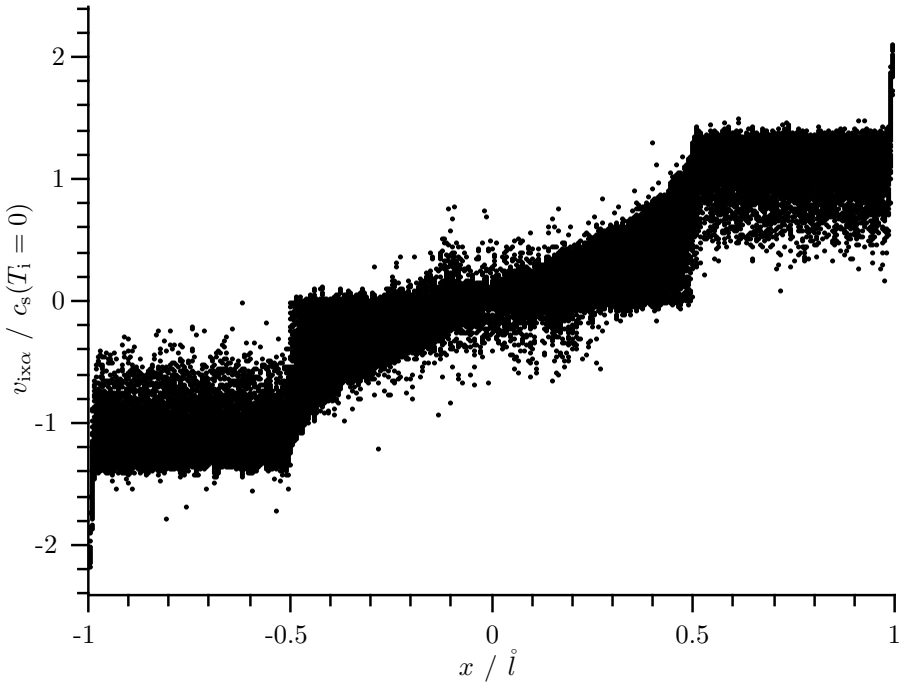

(c) Particle velocities v_{ix}.

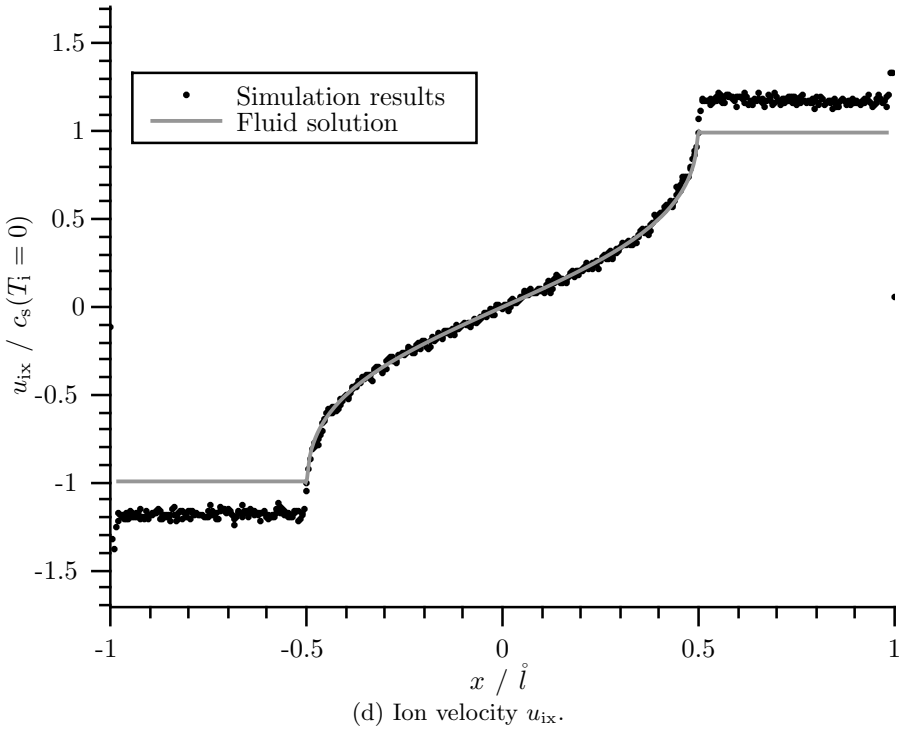

(d) Ion velocity u_{ix}.

Figure 7.4: (continued) Comparison of profiles from numerical integration of fluid equations with hybrid simulation results with $B = 0,\ \widehat{\nu}_{\mathrm{ie}} = 0,\ s_{\mathrm{n}} = Af_{\mathrm{cd}}(x),\ \mathbf{s}_{\mathrm{p}} = 0$. For the fluid solution the following boundary conditions were used $n_0 = 1.54,\ u_{\mathrm{ix}0} = 10^{-6},\ (n_{\mathrm{i}}u_{\mathrm{ix}})_1 = 0.7735$.

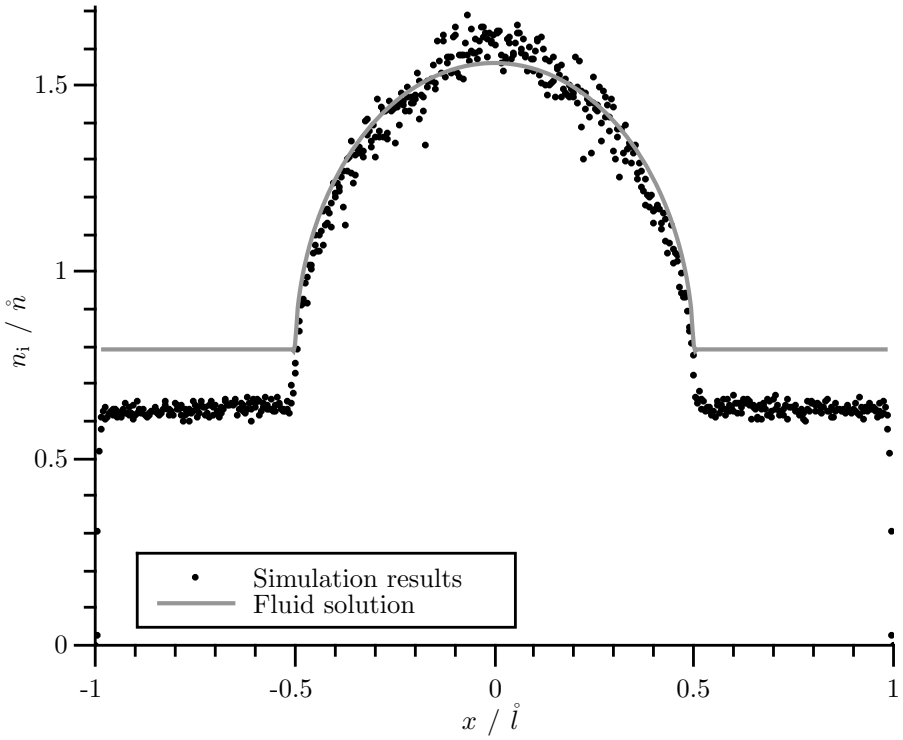

(a) Ion density n_i.

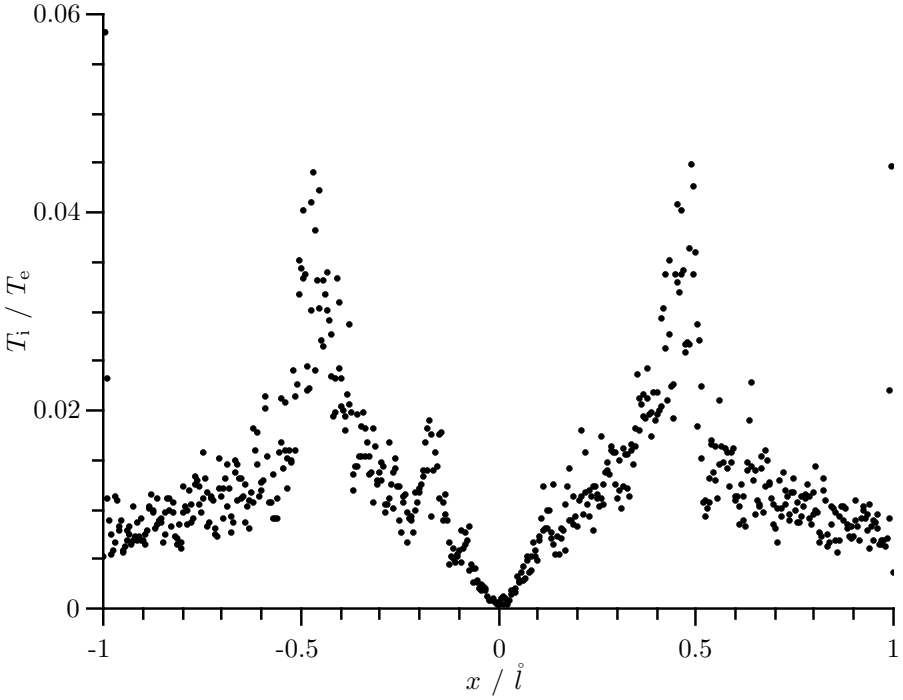

(b) Ion temperature T_i normalized on constant electron temperature T_e.

Figure 7.5: Comparison of profiles from numerical integration of fluid equations with hybrid simulation results with $B = 0,\ \widehat{\nu}_\mathrm{ie} = 1,\ s_\mathrm{n} = Af_\mathrm{cd}(x),\ \mathbf{s}_\mathrm{p} = 0$. For the fluid solution the following boundary conditions were used $n_0 = 1.56,\ u_\mathrm{ix0} = 10^{-6},\ (n_\mathrm{i}u_\mathrm{ix})_1 = 0.7816$.

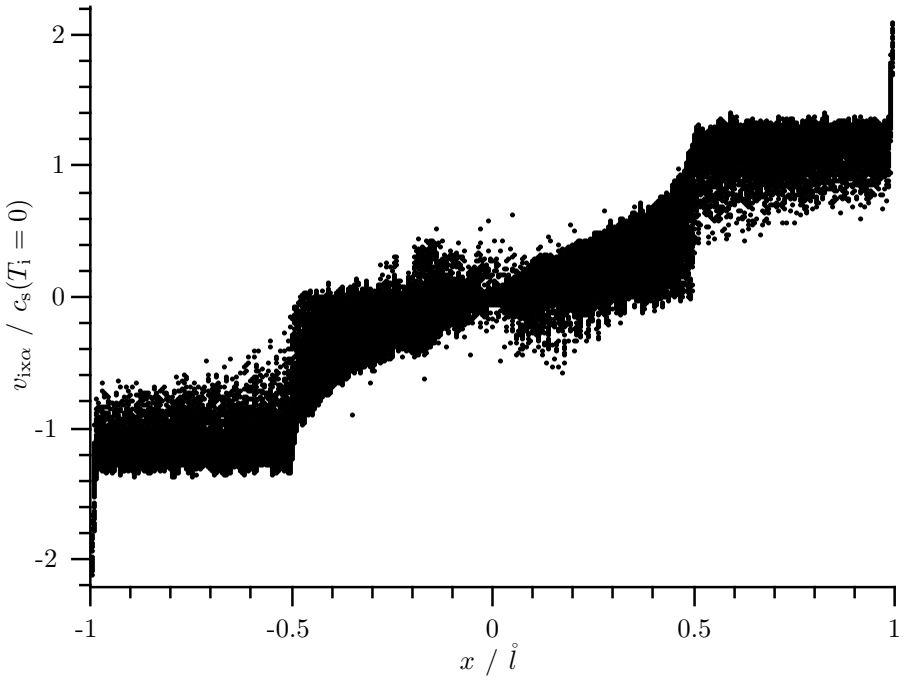

(c) Particle velocities v_{ix}.

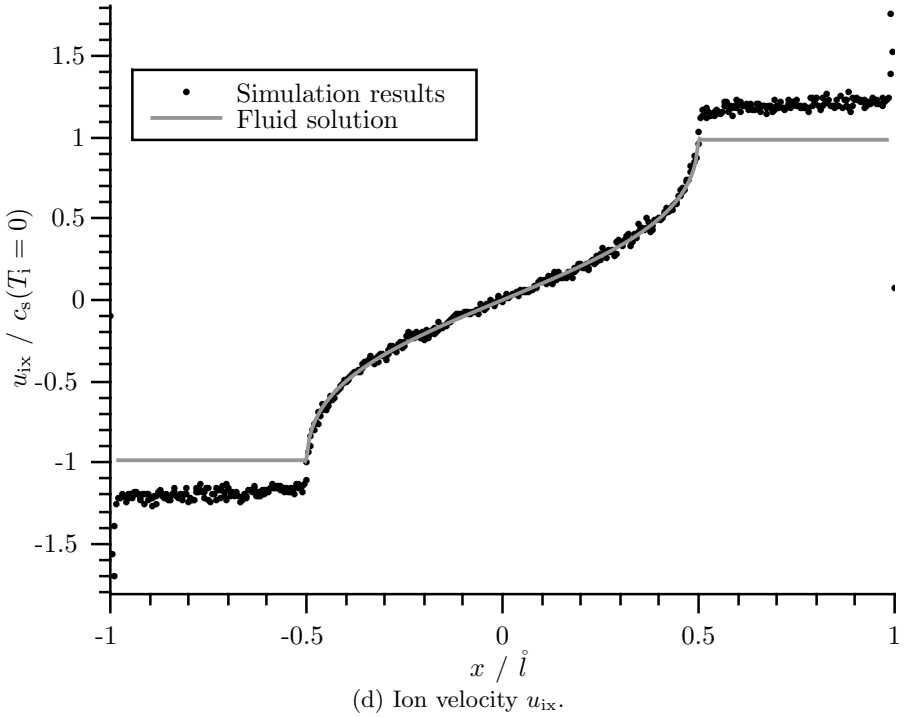

(d) Ion velocity u_{ix}.

Figure 7.5: (continued) Comparison of profiles from numerical integration of fluid equations with hybrid simulation results with $B = 0$, $\widehat{\nu}_{\mathrm{ie}} = 1$, $s_{\mathrm{n}} = Af_{\mathrm{cd}}(x)$, $\mathbf{s}_{\mathrm{p}} = 0$. For the fluid solution the following boundary conditions were used $n_0 = 1.56$, $u_{\mathrm{ix}0} = 10^{-6}$, $(n_{\mathrm{i}}u_{\mathrm{ix}})_1 = 0.7816$.

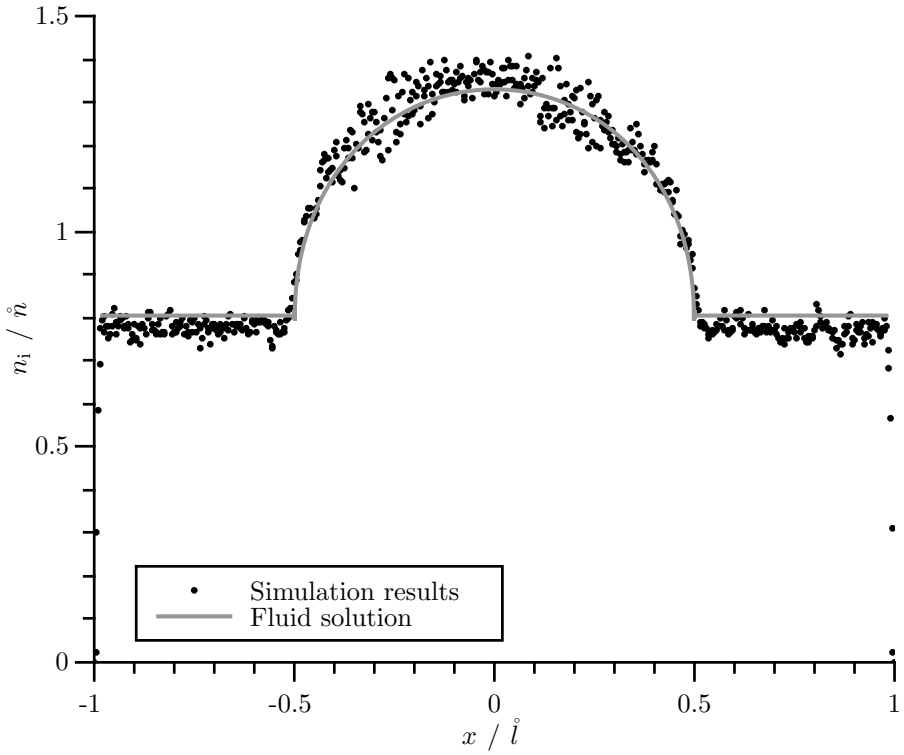

(a) Ion density n_i.

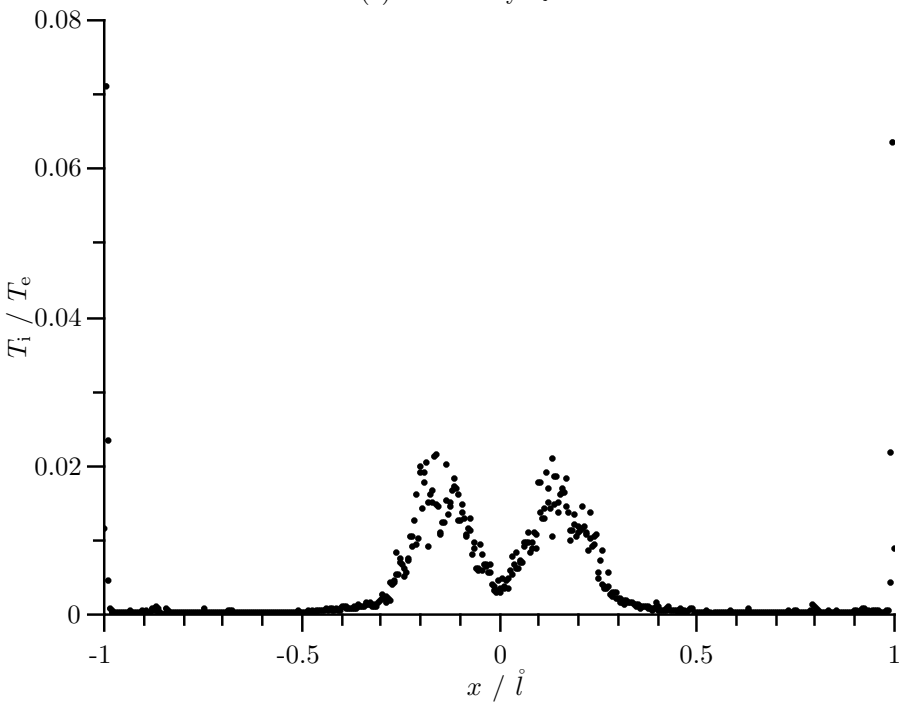

(b) Ion temperature T_i normalized on constant electron temperature T_e.

Figure 7.6: Comparison of profiles from numerical integration of fluid equations with hybrid simulation results with $B = 0$, $\widehat{\nu}_\mathrm{ie} = 0$, $s_\mathrm{n} = Af_\mathrm{cd}(x)$, $\mathbf{s}_\mathrm{p} = s_\mathrm{n}\mathbf{u}$. For the fluid solution the following boundary conditions were used $n_0 = 1.33$, $u_\mathrm{ix0} = 10^{-6}$, $(n_\mathrm{i}u_\mathrm{ix})_1 = 0.8090$.

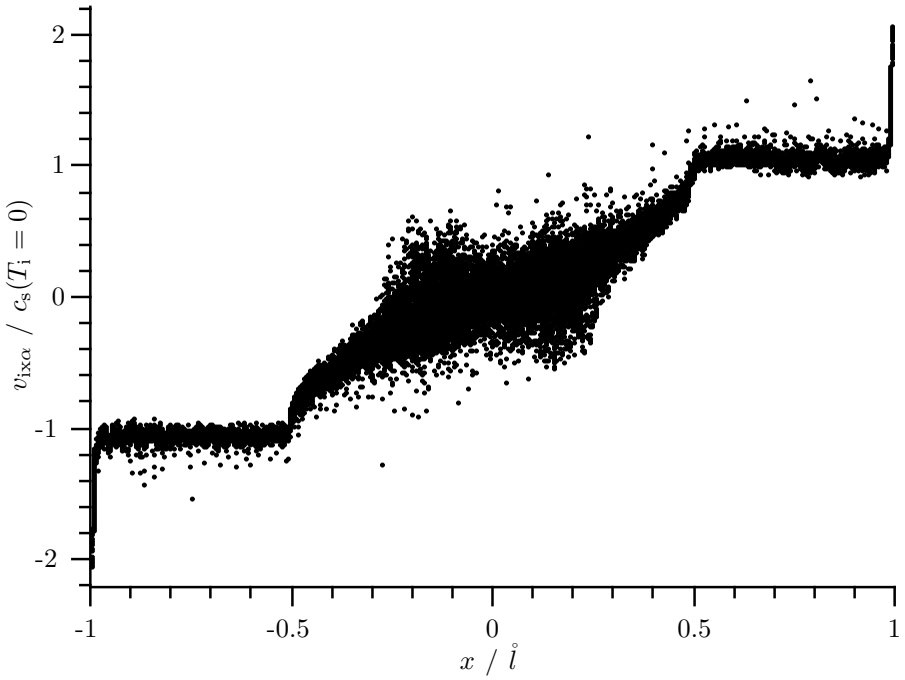

(c) Particle velocities v_{ix}.

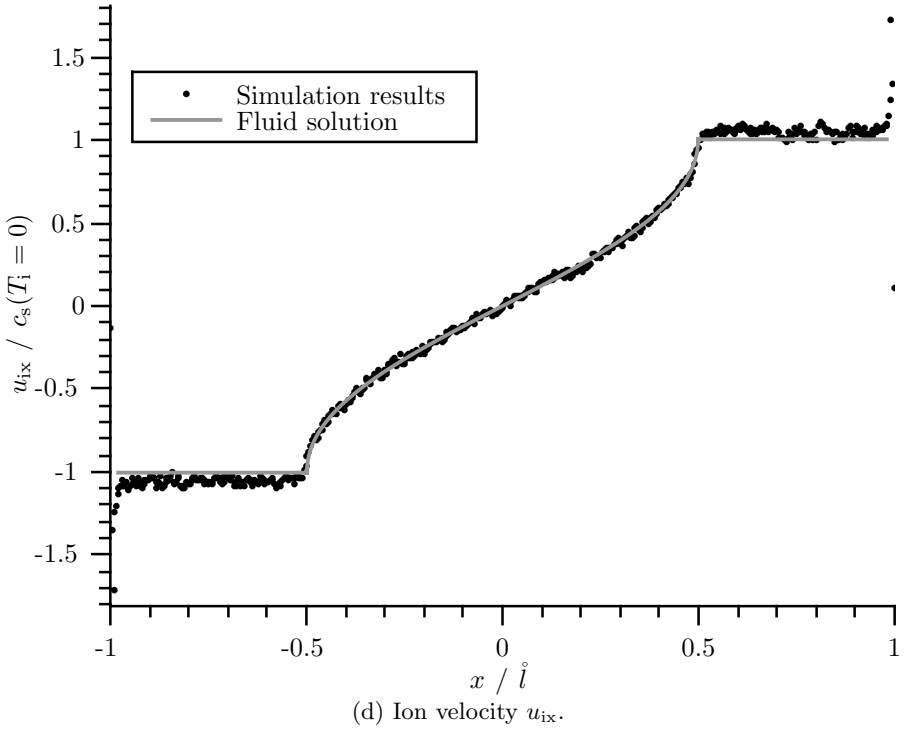

(d) Ion velocity u_{ix}.

Figure 7.6: (continued) Comparison of profiles from numerical integration of fluid equations with hybrid simulation results with $B = 0$, $\widehat{\nu}_{\mathrm{ie}} = 0$, $s_{\mathrm{n}} = Af_{\mathrm{cd}}(x)$, $\mathbf{s}_{\mathrm{p}} = s_{\mathrm{n}}\mathbf{u}$. For the fluid solution the following boundary conditions were used $n_0 = 1.33$, $u_{\mathrm{ix}0} = 10^{-6}$, $(n_{\mathrm{i}}u_{\mathrm{ix}})_1 = 0.8090$.

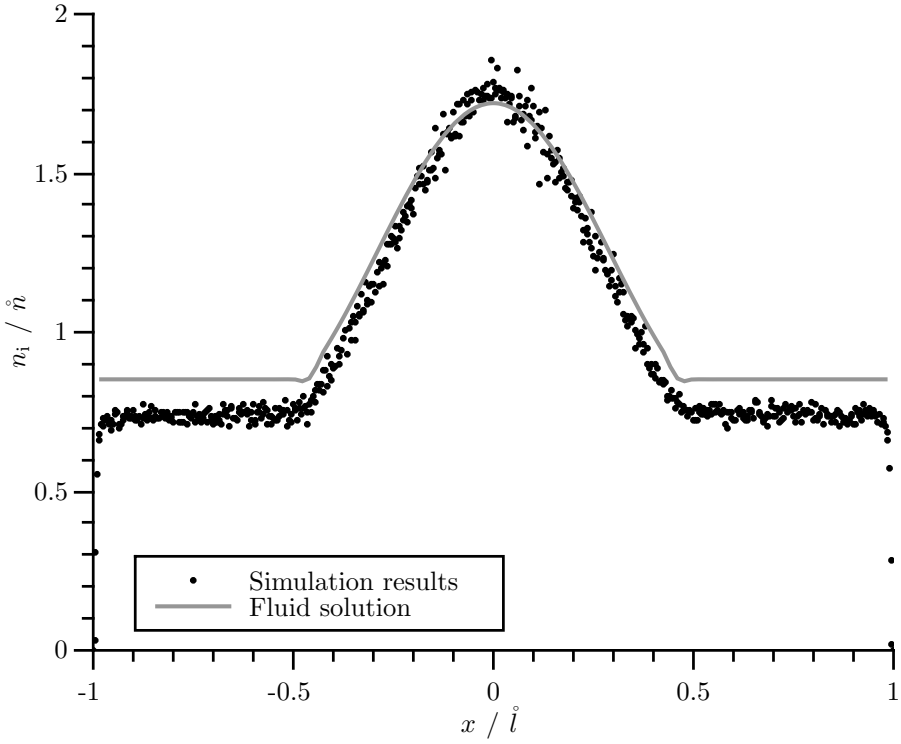

(a) Ion density n_i.

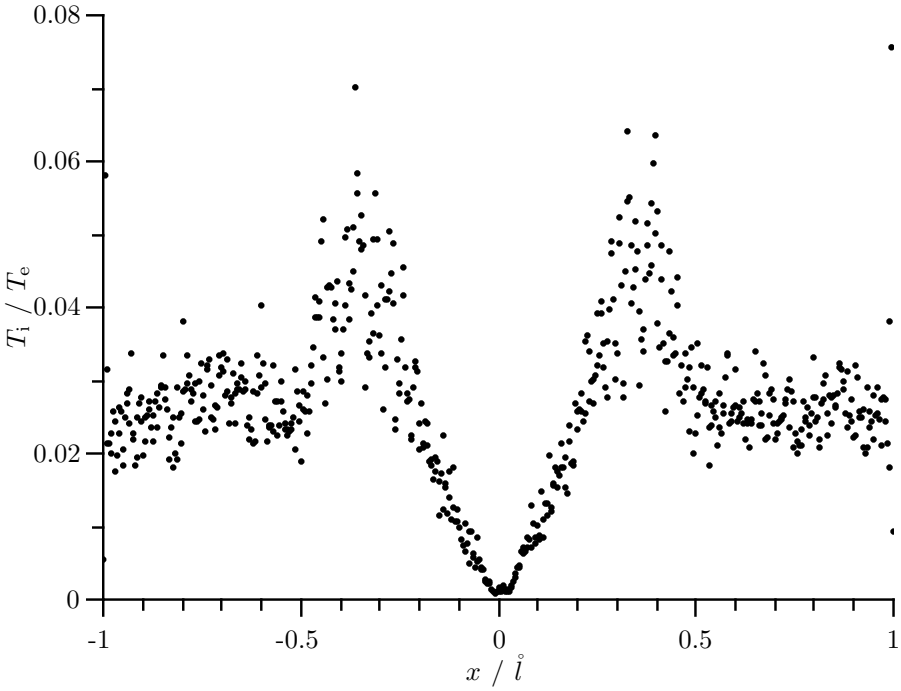

(b) Ion temperature T_i normalized on constant electron temperature T_e.

Figure 7.7: Comparison of profiles from numerical integration of fluid equations with hybrid simulation results with $B = 0,\ \widehat{\nu}_\mathrm{ie} = 0,\ s_\mathrm{n} = Af_\mathrm{rcd}(x),\ \mathbf{s}_\mathrm{p} = 0$. For the fluid solution the following boundary conditions were used $n_0 = 1.72,\ u_\mathrm{ix0} = 10^{-6},\ (n_\mathrm{i}u_\mathrm{ix})_1 = 0.8612$.

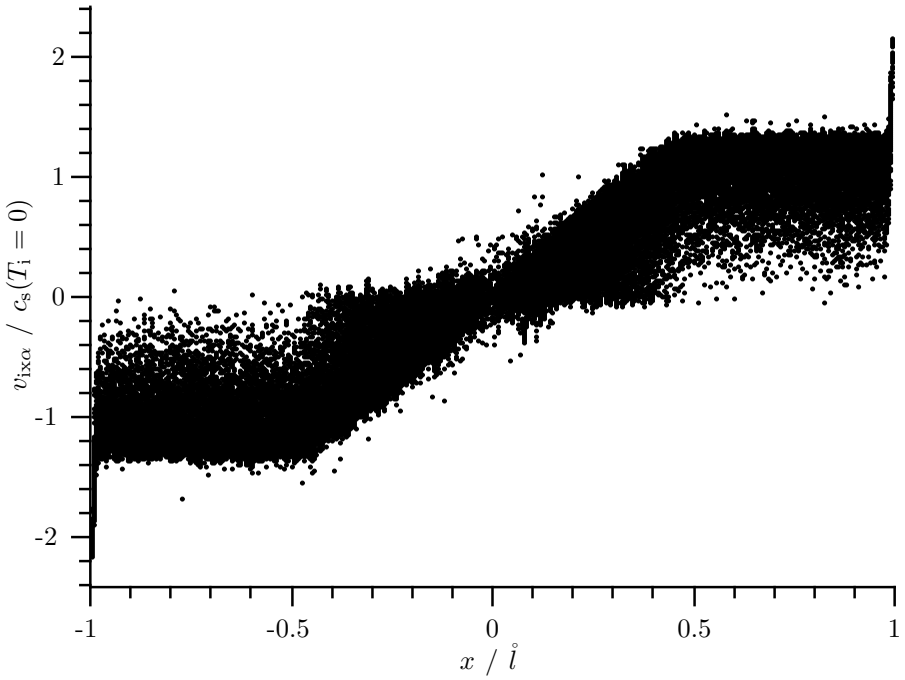

(c) Particle velocities v_{ix}.

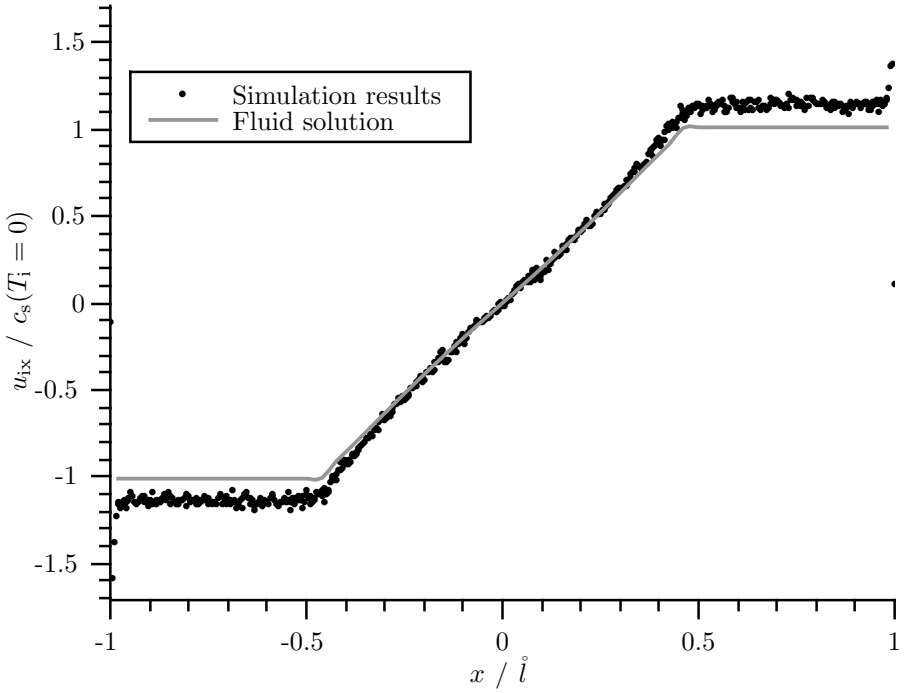

(d) Ion velocity u_{ix}.

Figure 7.7: (continued) Comparison of profiles from numerical integration of fluid equations with hybrid simulation results with $B = 0,\ \widehat{\nu}_{ie} = 0,\ s_n = Af_{rcd}(x),\ \mathbf{s}_p = 0$. For the fluid solution the following boundary conditions were used $n_0 = 1.72,\ u_{ix0} = 10^{-6},\ (n_i u_{ix})_1 = 0.8612$.

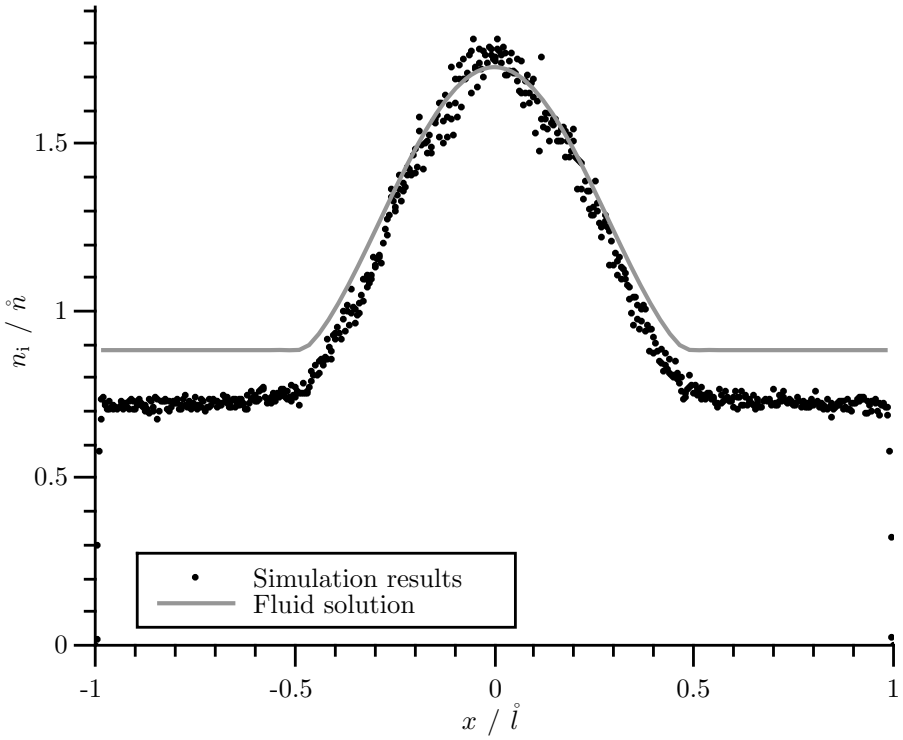

(a) Ion density n_i.

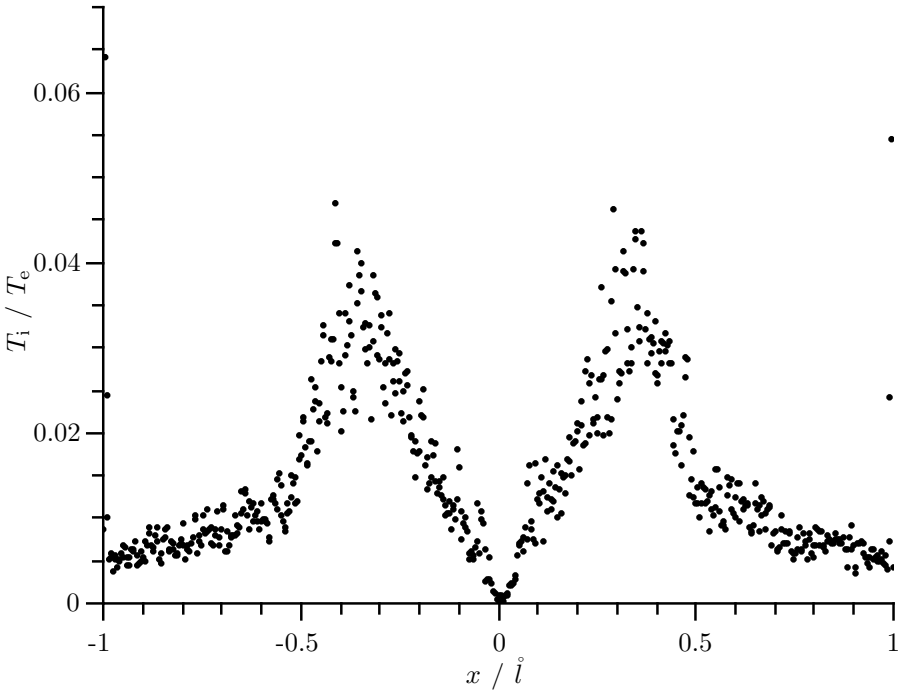

(b) Ion temperature T_i normalized on constant electron temperature T_e.

Figure 7.8: Comparison of profiles from numerical integration of fluid equations with hybrid simulation results with $B = 0,\ \widehat{\nu}_\mathrm{ie} = 1,\ s_\mathrm{n} = Af_\mathrm{rcd}(x),\ \mathbf{s}_\mathrm{p} = 0$. For the fluid solution the following boundary conditions were used $n_0 = 1.73,\ u_\mathrm{ix0} = 10^{-6},\ (n_\mathrm{i}u_\mathrm{ix})_1 = 0.8649$.

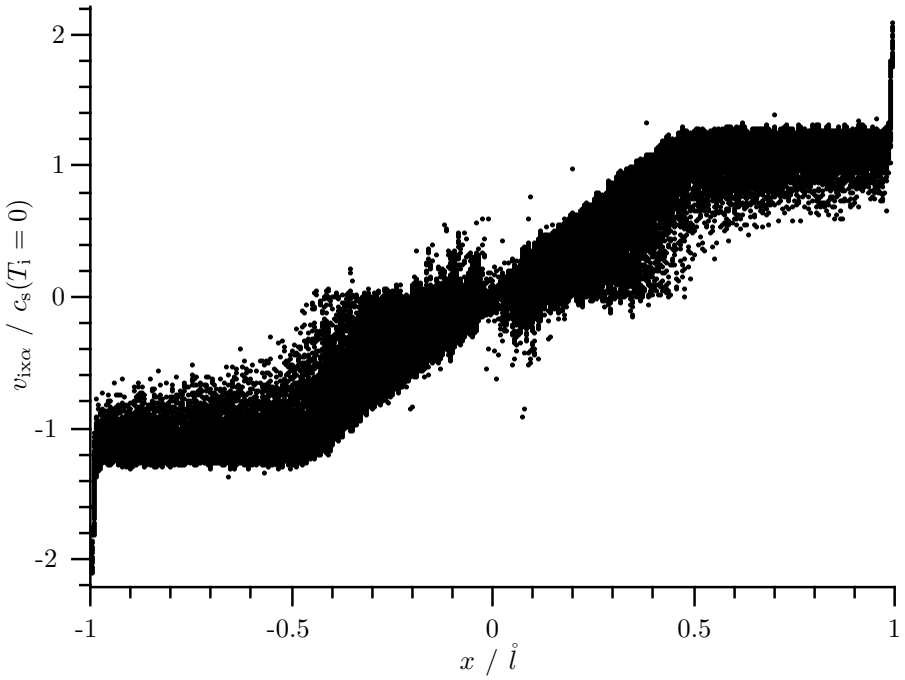

(c) Particle velocities v_{ix}.

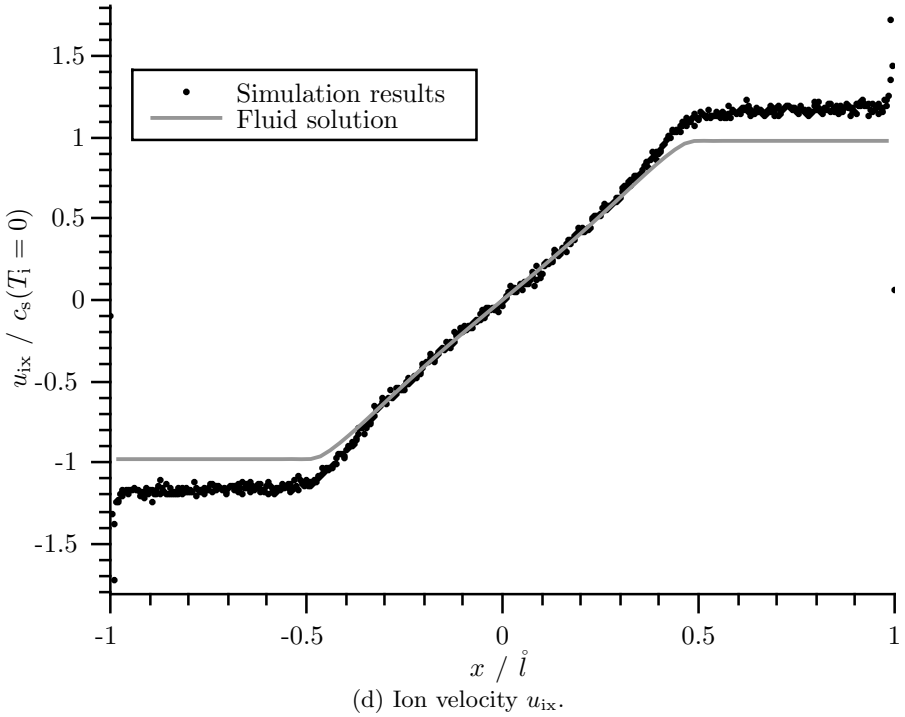

(d) Ion velocity u_{ix}.

Figure 7.8: (continued) Comparison of profiles from numerical integration of fluid equations with hybrid simulation results with $B = 0$, $\widehat{\nu}_{\mathrm{ie}} = 1$, $s_{\mathrm{n}} = Af_{\mathrm{rcd}}(x)$, $\mathbf{s}_{\mathrm{p}} = 0$. For the fluid solution the following boundary conditions were used $n_0 = 1.73$, $u_{\mathrm{ix}0} = 10^{-6}$, $(n_{\mathrm{i}}u_{\mathrm{ix}})_1 = 0.8649$.

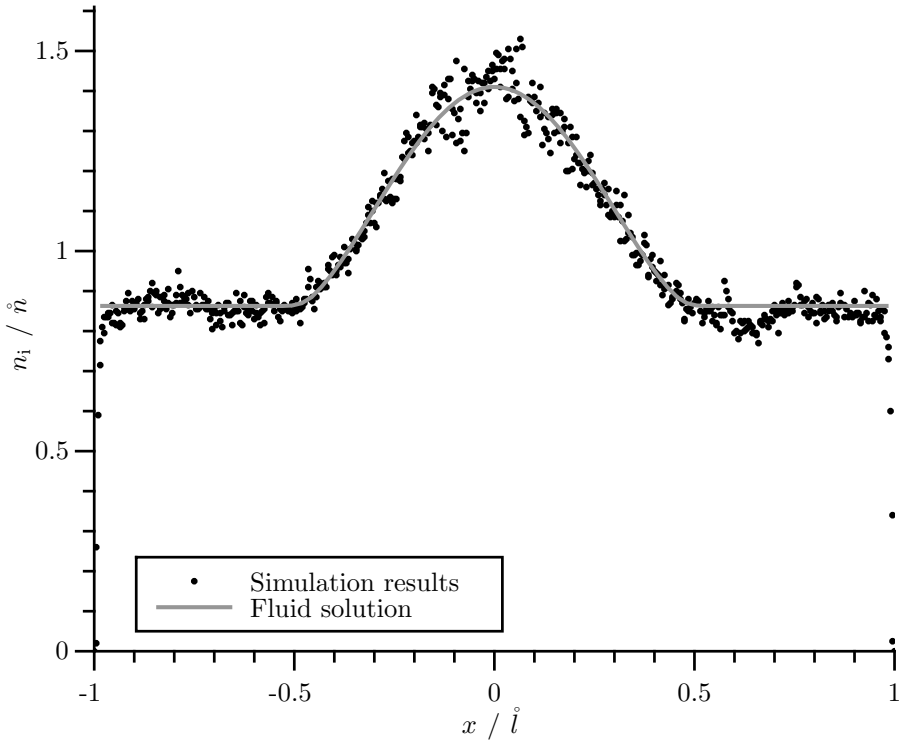

(a) Ion density n_i.

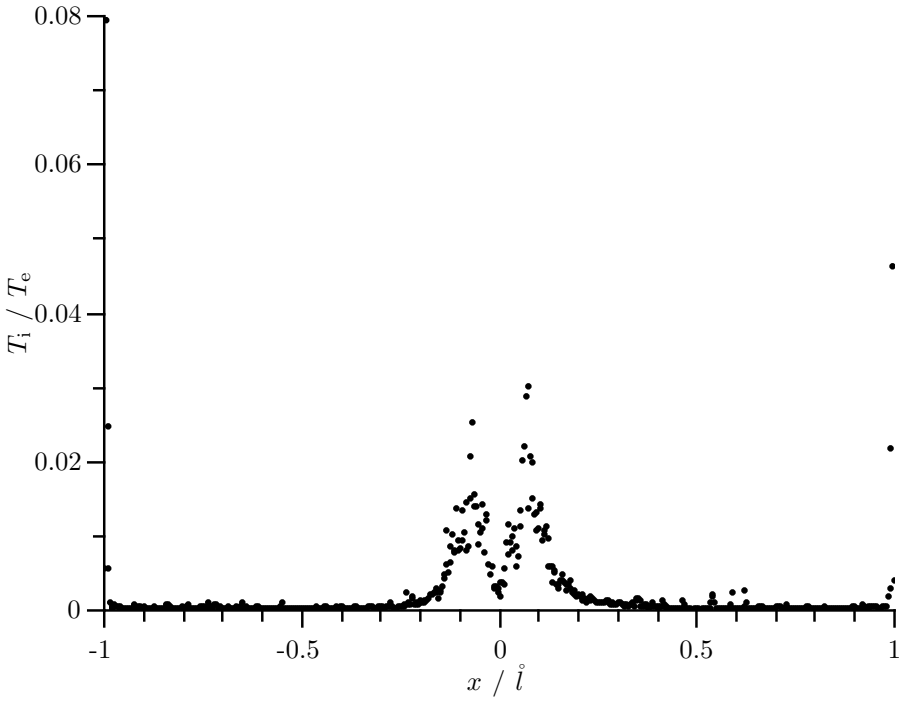

(b) Ion temperature T_i normalized on constant electron temperature T_e.

Figure 7.9: Comparison of profiles from numerical integration of fluid equations with hybrid simulation results with $B = 0$, $\widehat{\nu}_\mathrm{ie} = 0$, $s_\mathrm{n} = Af_\mathrm{rcd}(x)$, $\mathbf{s}_\mathrm{p} = s_\mathrm{n}\mathbf{u}$. For the fluid solution the following boundary conditions were used $n_0 = 1.41$, $u_\mathrm{ix0} = 10^{-6}$, $(n_\mathrm{i}u_\mathrm{ix})_1 = 0.8551$.

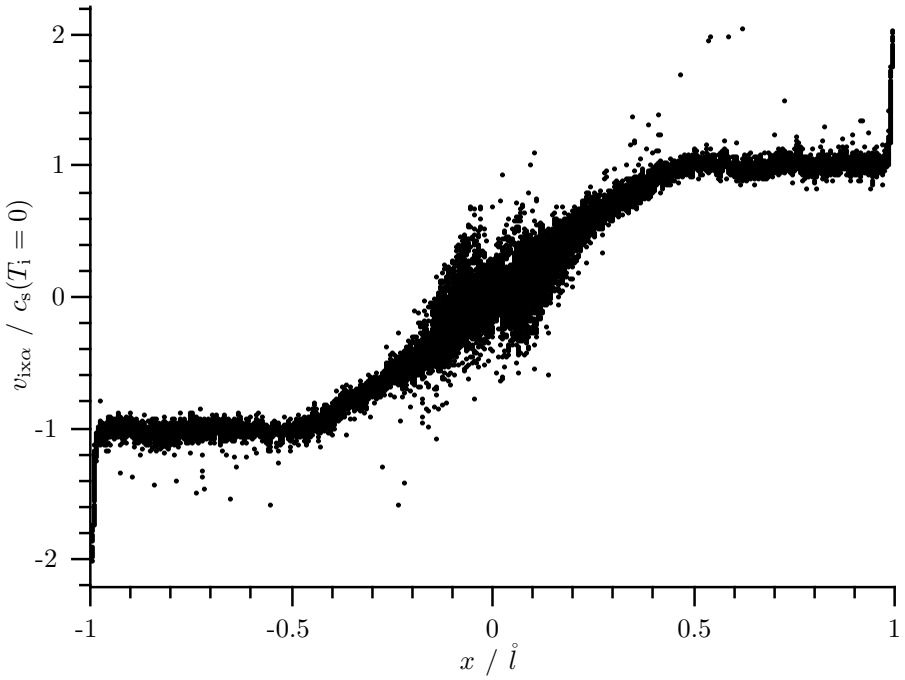

(c) Particle velocities v_{ix}.

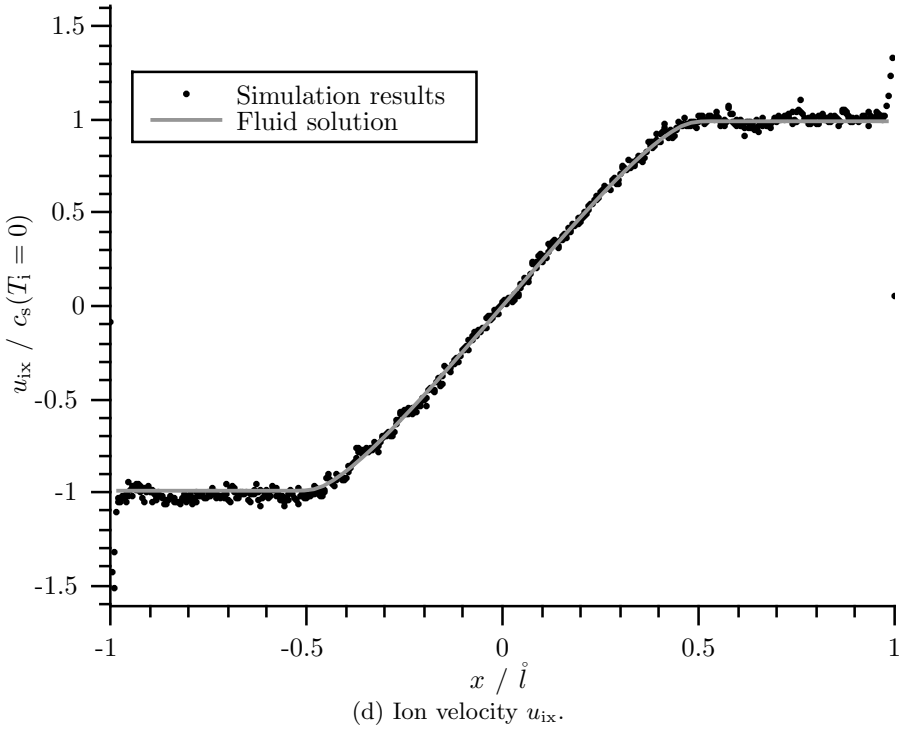

(d) Ion velocity u_{ix}.

Figure 7.9: (continued) Comparison of profiles from numerical integration of fluid equations with hybrid simulation results with $B = 0$, $\widehat{\nu}_{\mathrm{ie}} = 0$, $s_{\mathrm{n}} = Af_{\mathrm{rcd}}(x)$, $\mathbf{s}_{\mathrm{p}} = s_{\mathrm{n}}\mathbf{u}$. For the fluid solution the following boundary conditions were used $n_0 = 1.41$, $u_{\mathrm{ix}0} = 10^{-6}$, $(n_{\mathrm{i}}u_{\mathrm{ix}})_1 = 0.8551$.

7.2 Considering a magnetic field parallel to the walls

7.2.1 Analytic fluid approach

With a magnetic field parallel to the walls $\mathbf{B} = B_\mathrm{y}\mathbf{e}_\mathrm{y}$, the x– and z–component of the momentum balance (4.10) and (4.12) become

$$\left(u_\mathrm{ix} - \frac{c_\mathrm{s}^2}{u_\mathrm{ix}}\right)\partial_\mathrm{x}u_\mathrm{ix} = -\left(u_\mathrm{iz} - u_\mathrm{ez}\right)\Omega_\mathrm{iy} + \frac{u_\mathrm{ix}}{(n_\mathrm{i}u_\mathrm{ix})_0 + S_\mathrm{n}}\left(s_\mathrm{px} - s_\mathrm{n}\left(u_\mathrm{ix} + \frac{c_\mathrm{s}^2}{u_\mathrm{ix}}\right)\right),$$
$$u_\mathrm{ix}\partial_\mathrm{x}u_\mathrm{iz} = \left(u_\mathrm{ix} - u_\mathrm{ex}\right)\Omega_\mathrm{iy} + \frac{u_\mathrm{ix}}{(n_\mathrm{i}u_\mathrm{ix})_0 + S_\mathrm{n}}\left(s_\mathrm{pz} - s_\mathrm{n}u_\mathrm{iz}\right).$$

Inserting the electron velocities (4.13) and (4.15) decouples this system of differential equations, so that each equation can be solved independently.

$$\begin{aligned}
\left(u_\mathrm{ix} - \frac{c_\mathrm{s}^2}{u_\mathrm{ix}}\right)\partial_\mathrm{x}u_\mathrm{ix} &= \frac{-\Omega_\mathrm{iy}\left(u_\mathrm{ix} - \frac{\widetilde{j}_\mathrm{w}}{n_\mathrm{i}}\right) - \widetilde{E}_\mathrm{z}}{\nu_\mathrm{ie}}\Omega_\mathrm{iy} \\
&\quad + \frac{u_\mathrm{ix}}{(n_\mathrm{i}u_\mathrm{ix})_0 + S_\mathrm{n}}\left(s_\mathrm{px} - s_\mathrm{n}\left(u_\mathrm{ix} + \frac{c_\mathrm{s}^2}{u_\mathrm{ix}}\right)\right) \\
u_\mathrm{ix}\partial_\mathrm{x}u_\mathrm{iz} &= \frac{\widetilde{j}_\mathrm{w}}{n_\mathrm{i}}\Omega_\mathrm{iy} + \frac{u_\mathrm{ix}}{(n_\mathrm{i}u_\mathrm{ix})_0 + S_\mathrm{n}}\left(s_\mathrm{pz} - s_\mathrm{n}u_\mathrm{iz}\right) \\
\Leftrightarrow \qquad \partial_\mathrm{x}u_\mathrm{iz} &= \frac{\widetilde{j}_\mathrm{w}}{n_\mathrm{i}u_\mathrm{ix}}\Omega_\mathrm{iy} + \frac{s_\mathrm{pz} - s_\mathrm{n}u_\mathrm{iz}}{(n_\mathrm{i}u_\mathrm{ix})_0 + S_\mathrm{n}}
\end{aligned}$$

Considering the dependency of the collision frequency on the ion density (3.2) and eliminating the latter by means of equation (4.9) yields the final representation of the differential equations to be solved for a magnetic field parallel to the modeled walls.

$$\begin{aligned}
\left(u_\mathrm{ix} - \frac{c_\mathrm{s}^2}{u_\mathrm{ix}}\right)\partial_\mathrm{x}u_\mathrm{ix} &= \frac{u_\mathrm{ix}}{(n_\mathrm{i}u_\mathrm{ix})_0 + S_\mathrm{n}}\left(-\frac{\Omega_\mathrm{iy}^2}{\widehat{\nu}_\mathrm{ie}}u_\mathrm{ix} + s_\mathrm{px} - s_\mathrm{n}\left(u_\mathrm{ix} + \frac{c_\mathrm{s}^2}{u_\mathrm{ix}}\right) - \frac{\widetilde{E}_\mathrm{z}\Omega_\mathrm{iy}}{\widehat{\nu}_\mathrm{ie}}\right) \\
&\quad + \left(\frac{u_\mathrm{ix}}{(n_\mathrm{i}u_\mathrm{ix})_0 + S_\mathrm{n}}\right)^2\frac{\Omega_\mathrm{iy}^2\widetilde{j}_\mathrm{w}}{\widehat{\nu}_\mathrm{ie}} \\
\partial_\mathrm{x}u_\mathrm{iz} &= \frac{\widetilde{j}_\mathrm{w}\Omega_\mathrm{iy} + s_\mathrm{pz} - s_\mathrm{n}u_\mathrm{iz}}{(n_\mathrm{i}u_\mathrm{ix})_0 + S_\mathrm{n}}
\end{aligned} \tag{7.4}$$

Fluid approach without any sources

In the ionization–free border region ($x > x_1$) the integrated ionization source density S_n is constant. Inserting equation (3.12) which describes this circumstance into the above equations yields

$$\left(u_{\mathrm{ix}} - \frac{c_{\mathrm{s}}^2}{u_{\mathrm{ix}}}\right)\partial_{\mathrm{x}} u_{\mathrm{ix}} = \frac{\Omega_{\mathrm{iy}}}{(n_{\mathrm{i}}u_{\mathrm{ix}})_1 \widehat{\nu}_{\mathrm{ie}}}\left[\left(\frac{j_{\mathrm{w}}}{(n_{\mathrm{i}}u_{\mathrm{ix}})_1} - 1\right)\Omega_{\mathrm{iy}} u_{\mathrm{ix}}^2 - \widetilde{E}_{\mathrm{z}} u_{\mathrm{ix}}\right] = a_2 u_{\mathrm{ix}}^2 + a_1 u_{\mathrm{ix}},$$

$$\partial_{\mathrm{x}} u_{\mathrm{iz}} = \frac{\widetilde{j}_{\mathrm{w}}\Omega_{\mathrm{iy}}}{(n_{\mathrm{i}}u_{\mathrm{ix}})_1} = \text{const.},$$

where the constants a_2 and a_1 are introduced for convenience.

$$a_2 = \frac{\Omega_{\mathrm{iy}}^2}{(n_{\mathrm{i}}u_{\mathrm{ix}})_1 \widehat{\nu}_{\mathrm{ie}}}\left(\frac{j_{\mathrm{w}}}{(n_{\mathrm{i}}u_{\mathrm{ix}})_1} - 1\right) \qquad a_1 = -\frac{\Omega_{\mathrm{iy}}\widetilde{E}_{\mathrm{z}}}{(n_{\mathrm{i}}u_{\mathrm{ix}})_1 \widehat{\nu}_{\mathrm{ie}}}$$

Integration of the z–component from the ionization border to the border region is trivial and leads to a linear behavior of the ion fluid velocity in z–direction corresponding to $\mathbf{j} \times \mathbf{B}$ forces.

$$\int_{x_1}^{x} \partial_{\mathrm{x}'} u_{\mathrm{iz}}\,\mathrm{d}x' = u_{\mathrm{iz}} - u_{\mathrm{iz}1} = \int_{x_1}^{x} \frac{\widetilde{j}_{\mathrm{w}}\Omega_{\mathrm{iy}}}{(n_{\mathrm{i}}u_{\mathrm{ix}})_1}\,\mathrm{d}x' = \frac{\widetilde{j}_{\mathrm{w}}\Omega_{\mathrm{iy}}}{(n_{\mathrm{i}}u_{\mathrm{ix}})_1}(x - x_1)$$

$$\Leftrightarrow \qquad u_{\mathrm{iz}} = u_{\mathrm{iz}1} + \frac{\widetilde{j}_{\mathrm{w}}\Omega_{\mathrm{iy}}}{(n_{\mathrm{i}}u_{\mathrm{ix}})_1}(x - x_1)$$

To calculate the x–component, partial fraction decomposition is necessary to solve the occurring integrals

$$\int_{x_1}^{x} \mathrm{d}x' = x - x_1$$

$$= \int_{x_1}^{x} \frac{u_{\mathrm{ix}} - \frac{c_{\mathrm{s}}^2}{u_{\mathrm{ix}}}}{a_2 u_{\mathrm{ix}}^2 + a_1 u_{\mathrm{ix}}}\partial_{\mathrm{x}'} u_{\mathrm{ix}}\,\mathrm{d}x' = \int_{u_{\mathrm{ix}1}}^{u_{\mathrm{ix}}} \left(\frac{a_2 c_{\mathrm{s}}^2}{a_1^2 u'_{\mathrm{ix}}} - \frac{c_{\mathrm{s}}^2}{a_1 u'^2_{\mathrm{ix}}} + \frac{1 - c_{\mathrm{s}}^2 \frac{a_2^2}{a_1^2}}{a_2 u'_{\mathrm{ix}} + a_1}\right)\mathrm{d}u'_{\mathrm{ix}}$$

$$= \frac{a_2 c_{\mathrm{s}}^2}{a_1^2}\ln\left(\frac{u_{\mathrm{ix}}}{u_{\mathrm{ix}1}}\right) + \frac{c_{\mathrm{s}}^2}{a_1}\left(\frac{1}{u_{\mathrm{ix}}} - \frac{1}{u_{\mathrm{ix}1}}\right) + \left(\frac{1}{a_2} - c_{\mathrm{s}}^2\frac{a_2}{a_1^2}\right)\ln\left(\frac{a_2 u_{\mathrm{ix}} + a_1}{a_2 u_{\mathrm{ix}1} + a_1}\right)$$

yielding an implicit equation.

This solution does not apply for the case without any electric field $\boldsymbol{E_{\mathrm{y}} = 0}$ since it becomes singular. Instead the original differential equation can be integrated easily

$$\int_{x_1}^{x} a_2\,\mathrm{d}x' = \int_{x_1}^{x}\left(\frac{1}{u_{\mathrm{ix}}} - \frac{c_{\mathrm{s}}^2}{u_{\mathrm{ix}}^3}\right)\partial_{\mathrm{x}'} u_{\mathrm{ix}}\,\mathrm{d}x'$$

$$\Leftrightarrow \qquad a_2(x - x_1) = \ln\left(\frac{u_{\mathrm{ix}}}{u_{\mathrm{ix}1}}\right) + \frac{c_{\mathrm{s}}^2}{2}\left(\frac{1}{u_{\mathrm{ix}}^2} - \frac{1}{u_{\mathrm{ix}1}^2}\right)$$

again yielding an implicit equation. This case corresponds to the investigations of Alterkop et al., which was supplemented here by a non–vanishing wall current

density j_w and additional constant electric fields parallel to the wall E_y, E_z. Their results conform to the above equation. They also note that the ions are mainly accelerated in a layer of thickness $\sim r_\mathrm{i}(c_\mathrm{s})/\beta(x_2)$ with $r_\mathrm{i}(c_\mathrm{s}) = \Omega_\mathrm{iy}/c_\mathrm{s}$ the ion gyro radius at sound velocity and $\beta(x_2) = \Omega_\mathrm{iy}/\nu_\mathrm{ie}(x_2)$ the Hall parameter at the sheath edge $x = x_2$. This observation is described by the factor a_2 in the above presented solution. Applying conservation of ion mass (4.9), splitting the boundary condition of the ion flux to density and velocity and substituting the collision term (3.2) reveals

$$a_2 = \frac{\Omega_\mathrm{iy}^2}{(n_\mathrm{i}u_\mathrm{ix})_1\widehat{\nu}_\mathrm{ie}} = \frac{\Omega_\mathrm{iy}^2}{(n_\mathrm{i}u_\mathrm{ix})_2\widehat{\nu}_\mathrm{ie}} = \frac{\Omega_\mathrm{iy}^2}{n_\mathrm{i2}u_\mathrm{ix2}\widehat{\nu}_\mathrm{ie}} = \frac{\Omega_\mathrm{iy}^2}{u_\mathrm{ix2}\nu_\mathrm{ie}(x_2)} = \frac{\beta(x_2)}{r_\mathrm{i}(u_\mathrm{ix2})} \tag{7.5}$$

where the numerical indexes correspond to boundary conditions at positions x_1 and x_2, respectively. Thus the results of Alterkop et al. are reproduced as long as the Bohm criterion is respected $u_\mathrm{ix2} = c_\mathrm{s}$. [AGB05]

Fluid approach without momentum source

Assuming ionization from resting neutral gas sets the momentum source density to zero $\mathbf{s}_\mathrm{p} = 0$. The following considerations omits the wall current density $\boldsymbol{j_\mathrm{w}} = \mathbf{0}$ since its additional ion density term makes an analytical solution of the x–component impossible. Secondary, these investigations only consider a constant ionization source density $\boldsymbol{s_\mathrm{n}} = \mathbf{const.}$ that allows an analytical solution by separation of variables. For the cosine–shaped ionization source density only the numerical profiles along with the hybrid simulation results are provided later.

$$\left(u_\mathrm{ix} - \frac{c_\mathrm{s}^2}{u_\mathrm{ix}}\right)\partial_\mathrm{x}u_\mathrm{ix} = \frac{u_\mathrm{ix}}{(n_\mathrm{i}u_\mathrm{ix})_0 + S_\mathrm{n}}\left(-\frac{\Omega_\mathrm{iy}^2}{\widehat{\nu}_\mathrm{ie}}u_\mathrm{ix} - s_\mathrm{n}\left(u_\mathrm{ix} + \frac{c_\mathrm{s}^2}{u_\mathrm{ix}}\right) - \frac{\widetilde{E}_\mathrm{z}\Omega_\mathrm{iy}}{\widehat{\nu}_\mathrm{ie}}\right)$$

$$\partial_\mathrm{x}u_\mathrm{iz} = \frac{-s_\mathrm{n}u_\mathrm{iz}}{(n_\mathrm{i}u_\mathrm{ix})_0 + S_\mathrm{n}}$$

Integrating the z–component of the total momentum equation from inside the ionization domain to its border yields

$$\int_x^{x_1} \frac{1}{u_\mathrm{iz}}\partial_{\mathrm{x}'}u_\mathrm{iz}\,\mathrm{d}x = \int_x^{x_1} \frac{-s_\mathrm{n}}{(n_\mathrm{i}u_\mathrm{ix})_0 + S_\mathrm{n}}\,\mathrm{d}x.$$

Solving the above integrals is possible by substitution and additionally applying the continuity condition from equation (3.12), which leads to the final expression

for the ion fluid velocity in z–direction.

$$\ln\left(\frac{u_{\mathrm{iz1}}}{u_{\mathrm{iz}}}\right) = \ln\left(\frac{(n_{\mathrm{i}}u_{\mathrm{ix}})_0 + S_{\mathrm{n}}(x_1)}{(n_{\mathrm{i}}u_{\mathrm{ix}})_0 + S_{\mathrm{n}}(x)}\right) = \ln\left(\frac{(n_{\mathrm{i}}u_{\mathrm{ix}})_1}{(n_{\mathrm{i}}u_{\mathrm{ix}})_0 + S_{\mathrm{n}}(x)}\right)$$
$$\Leftrightarrow \qquad u_{\mathrm{iz}} = u_{\mathrm{iz1}}\frac{(n_{\mathrm{i}}u_{\mathrm{ix}})_0 + S_{\mathrm{n}}(x)}{(n_{\mathrm{i}}u_{\mathrm{ix}})_1}$$

The x–component of the momentum balance can be solved by following the subsequent steps. Firstly, the polynomial in the denominator on the right hand side of the equation is sorted

$$\left(u_{\mathrm{ix}} - \frac{c_{\mathrm{s}}^2}{u_{\mathrm{ix}}}\right)\partial_{\mathrm{x}}u_{\mathrm{ix}} = \frac{1}{(n_{\mathrm{i}}u_{\mathrm{ix}})_0 + S_{\mathrm{n}}}\left[\left(-\frac{\Omega_{\mathrm{iy}}^2}{\widehat{\nu}_{\mathrm{ie}}} - s_{\mathrm{n}}\right)u_{\mathrm{ix}}^2 - \frac{\widetilde{E}_{\mathrm{z}}\Omega_{\mathrm{iy}}}{\widehat{\nu}_{\mathrm{ie}}}u_{\mathrm{ix}} - s_{\mathrm{n}}c_{\mathrm{s}}^2\right]$$
$$= \frac{a_2u_{\mathrm{ix}}^2 + a_1u_{\mathrm{ix}} + a_0}{(n_{\mathrm{i}}u_{\mathrm{ix}})_0 + S_{\mathrm{n}}}$$

with constants

$$a_2 = -\frac{\Omega_{\mathrm{iy}}^2}{\widehat{\nu}_{\mathrm{ie}}} - s_{\mathrm{n}}, \qquad a_1 = -\frac{\widetilde{E}_{\mathrm{z}}\Omega_{\mathrm{iy}}}{\widehat{\nu}_{\mathrm{ie}}}, \qquad a_0 = -s_{\mathrm{n}}c_{\mathrm{s}}^2.$$

Secondly, after separating the variables, partial fraction decomposition is applied, so that each summand can be integrated

$$\frac{1}{(n_{\mathrm{i}}u_{\mathrm{ix}})_0 + S_{\mathrm{n}}} = \frac{u_{\mathrm{ix}} - \frac{c_{\mathrm{s}}^2}{u_{\mathrm{ix}}}}{a_2u_{\mathrm{ix}}^2 + a_1u_{\mathrm{ix}} + a_0}\partial_{\mathrm{x}}u_{\mathrm{ix}} = \left(\frac{b_0}{u_{\mathrm{ix}}} + \frac{b_2u_{\mathrm{ix}} + b_1}{a_2u_{\mathrm{ix}}^2 + a_1u_{\mathrm{ix}} + a_0}\right)\partial_{\mathrm{x}}u_{\mathrm{ix}}$$

with constants

$$b_2 = 1 + c_{\mathrm{s}}^2\frac{a_2}{a_0} = 2 + \frac{\Omega_{\mathrm{iy}}^2}{\widehat{\nu}_{\mathrm{ie}}s_{\mathrm{n}}}, \qquad b_1 = c_{\mathrm{s}}^2\frac{a_1}{a_0} = -\frac{\Omega\widetilde{E}_{\mathrm{z}}}{\widehat{\nu}_{\mathrm{ie}}s_{\mathrm{n}}}, \qquad b_0 = -\frac{c_{\mathrm{s}}^2}{a_0} = s_{\mathrm{n}}.$$

Finally, the integration from inside the ionization domain to its border yields

$$\int_x^{x_1}\frac{1}{(n_{\mathrm{i}}u_{\mathrm{ix}})_0 + S_{\mathrm{n}}}\,\mathrm{d}x' = \int_x^{x_1}\left(\frac{b_0}{u_{\mathrm{ix}}} + \frac{b_2u_{\mathrm{ix}} + b_1}{a_2u_{\mathrm{ix}}^2 + a_1u_{\mathrm{ix}} + a_0}\right)\partial_{\mathrm{x}'}u_{\mathrm{ix}}\,\mathrm{d}x'$$

and inserting the continuity condition (3.12) yields an implicit equation

$$\ln\left(\frac{(n_{\mathrm{i}}u_{\mathrm{ix}})_1}{(n_{\mathrm{i}}u_{\mathrm{ix}})_0 + S_{\mathrm{n}}}\right) = \ln\left(\frac{u_{\mathrm{ix1}}}{u_{\mathrm{ix}}}\right) + \frac{1}{2}\left(\frac{s_{\mathrm{n}}}{a_2} - 1\right)\ln\left(\frac{a_2u_{\mathrm{ix1}}^2 + a_1u_{\mathrm{ix1}} + a_0}{a_2u_{\mathrm{ix}}^2 + a_1u_{\mathrm{ix}} + a_0}\right)$$
$$- \frac{a_1}{\sqrt{4a_2a_0 - a_1^2}}\left(\frac{s_{\mathrm{n}}}{a_2} + 1\right)\left[\arctan\left(\frac{2a_2u_{\mathrm{ix1}} + a_1}{\sqrt{4a_2a_0 - a_1^2}}\right) - \arctan\left(\frac{2a_2u_{\mathrm{ix}} + a_1}{\sqrt{4a_2a_0 - a_1^2}}\right)\right].$$

It is noted here that the arc tangent term originates from the constant electric field E_{y} and vanishes for $E_{\mathrm{y}} = 0$.

Fluid approach with both ionization and momentum source

Ionization from a comoving gas background sets the momentum source density to $\mathbf{s}_\mathrm{p} = s_\mathrm{n}\mathbf{u}_\mathrm{i}$. Again, only the case with a constant ionization source density $\boldsymbol{s_\mathrm{n} = \text{const.}}$ and without a wall current density $\boldsymbol{j_\mathrm{w} = 0}$ is considered due to the same reasons as in the previous case.

$$\left(u_\mathrm{ix} - \frac{c_\mathrm{s}^2}{u_\mathrm{ix}}\right)\partial_\mathrm{x} u_\mathrm{ix} = \frac{u_\mathrm{ix}}{(n_\mathrm{i}u_\mathrm{ix})_0 + S_\mathrm{n}}\left(-\frac{\Omega_\mathrm{iy}^2}{\widehat{\nu}_\mathrm{ie}}u_\mathrm{ix} - s_\mathrm{n}\frac{c_\mathrm{s}^2}{u_\mathrm{ix}} - \frac{\widetilde{E}_\mathrm{z}\Omega_\mathrm{iy}}{\widehat{\nu}_\mathrm{ie}}\right)$$

$$\partial_\mathrm{x} u_\mathrm{iz} = 0$$

Here, the z–component of the momentum balance just yields a constant fluid velocity u_iz.

$$\int_x^{x_1} \partial_{\mathrm{x}'} u_\mathrm{iz}\,\mathrm{d}x = 0 \qquad \Leftrightarrow \qquad u_\mathrm{iz} = u_\mathrm{iz1}$$

The x–component of the momentum balance only differs from the case above by the coefficients, thus resulting in the same implicit equation for different constants, namely

$$a_2 = -\frac{\Omega_\mathrm{iy}^2}{\widehat{\nu}_\mathrm{ie}}, \qquad a_1 = -\frac{\widetilde{E}_\mathrm{z}\Omega_\mathrm{iy}}{\widehat{\nu}_\mathrm{ie}}, \qquad a_0 = -s_\mathrm{n}c_\mathrm{s}^2.$$

7.2.2 Hybrid simulation results

Currently, the total momentum equation was only solvable with restrictions on different parameters and yielded implicit equations after integration. Now the numerical integration of the differential equations from the fluid model along with the hybrid simulation results are provided in the following.

As stated by Alterkop et al. and confirmed in equation (7.5), the ions are mainly accelerated in a layer before the walls of size $\sim r_\mathrm{i}(c_\mathrm{s})/\beta(x_2)$ which means that its size is dependent on the magnetic field B_y on the one hand and the collision frequency at the walls $\nu_\mathrm{ie}(x_2)$ on the other. Since the influence of the collision frequency along with its effect on the ion temperature has been discussed in the previous section 7.1, only the magnetic field B_y will be varied to investigate this dependency while keeping the collision frequency parameter $\widehat{\nu}_\mathrm{ie}$ constant. This is performed in various simulation runs, whose results are displayed along with the velocities in z–direction in Fig. 7.10 to 7.12. Here a constant ionization source density $s_\mathrm{n} = Af_\mathrm{cd}$ is set while assuming a comoving gas background $\mathbf{s}_\mathrm{p} = s_\mathrm{n}\mathbf{u}_\mathrm{i}$. To examine the influence of the momentum source density, simulation results with ionization from a resting gas background $\mathbf{s}_\mathrm{p} = 0$

and $B_y = 1$ are pictured in 7.14. Finally simulation runs with the cosine–shaped ionization source density $s_n = Af_{rcd}$ and $B_y = 1$ were performed with $\mathbf{s}_p = 0$ (Fig. 7.15) and $\mathbf{s}_p = s_n \mathbf{u}_i$ (Fig. 7.13).

In the following the profiles of density n_i and average velocity in x–direction u_{ix} for different magnetic fields are discussed, which can be categorized in three different cases. For strongly magnetized plasmas $r_i(c_s) \ll x_2$ the acceleration of the ions mainly happens in the border region which is shown in Fig. 7.10. The effect of ionization on the profiles is vanishingly small. Both profiles are smooth compared to the other simulation results. For weakly magnetized plasmas $r_i(c_s) \gg x_2$ profiles are similar to those without magnetic fields in the ionization region, so that the ionization is the dominant process here as pictured in Fig. 7.11, but in the border region where no ionization takes place, the magnetic field is responsible for the deviation from the constant solution. For $r_i(c_s) \approx x_2$ both ionization and magnetic field seem to play a similar role for the profiles which can be observed in Fig. 7.12. One additional observation for the latter two cases is, that the density profiles n_i from simulation differ uniformly from those of the numerical integration in the center of the ionization region. This effect is not visible in the velocity profiles u_{ix}, which does not simultaneously mean that they do not manifest here according to equation (4.9). The reason for this behavior is most likely explained by the magnetic field, since it is not observable in the cases without it. Since the domain is symmetric to its center, the positions where the particles are ionized basically determine to which wall they will move. The gyration induced by magnetic fields disturbs the collective motion of the ions in the domain center, which has a severe impact on the profiles in this particular region. This anisotropic effect is most likely responsible for the deviation from the fluid solution because only a simplified version of the stress tensor is considered in its derivation. This is the reason why the boundary conditions for the numerical integration of the fluid equations were chosen so that the profiles fit the hybrid results well in the border region.

Concerning the ion velocities in z–direction, a vast deviation of the hybrid results from the zero fluid solutions are observable. For weakly magnetized plasmas and plasmas for which $r_i(c_s) \approx x_2$ is valid, the velocity is negatively constant in the right side of the domain and positively constant in the left side, yielding some kind of drift separately on each side. Both branches merge in the center region over a similar length scale for both cases, which is most likely caused by the same reason of ions moving in separate directions as already mentioned above. For the considered simulation runs ionization from a comoving neutral gas background is assumed, so that each particle is inserted with the respective average velocity $\mathbf{u}_i$ at its ionization position. By doing so the inserted particles also adapt the gyro phase of the surrounding particles, so that an

isotropic gyro motion is happening, which is a possible explanation for the constant solution for each separate branch. For weakly magnetized plasmas, the constants for each branch have similar absolute values, whereas for $r_\mathrm{i}(c_\mathrm{s}) \approx x_2$ those are different. This is also observable in the simulation runs with a cosine–shaped ionization density which is why it is most probably a physical effect. To compare anyhow both hybrid and fluid results in this case, different boundary conditions are considered for each branch, denoted by f_l for the left one and f_r for the right one where f specifies the boundary condition. If only one boundary condition is specified for the ion velocity or their flux, then $f \equiv f_\mathrm{r} = -f_\mathrm{l}$ applies.

When ionization from a neutral gas background is considered, the velocities differ from constants which can be seen in Fig. 7.14 and 7.15. Here, the average velocity u_iz again diverges in the center region, but relaxes to zero at the walls, where it gets more and more diffuse. Each branch here is rather noisy compared to the case with a comoving gas background. Contrary to the comoving case, the ions are inserted with zero velocity and are thus not assigned to any gyro phase at all. They start gyrating after initial acceleration by the electric field, thus yielding rather evenly distributed gyro phases, which may be the reason for the observed behavior. Unlike the hybrid results, the fluid solution falls down to zero after a very short length for $\mathbf{s}_\mathrm{p} = 0$, since equation (7.4) gets singular at $x = 0$. This indicates that the differences between both results are most likely caused by kinetic effects, which is why $u_\mathrm{iz0} = 0$ is chosen to be the boundary condition for the upcoming presentation of the results in Fig. 7.14 and 7.15.

For strongly magnetized plasmas, the ion velocity u_iz is only zero in the ionization region and diffuses in the border region. In the beginning of the simulation this diffusive part is localized at the walls and then propagates gradually deeper into the plasma up to the ionization domain, extending into it in the same magnitude for both sides.

For completeness, results from simulation runs corresponding to $r_\mathrm{i}(c_\mathrm{s}) \approx x_2$ with the cosine–shaped ionization source density $s_\mathrm{n} = A f_\mathrm{rcd}$ are provided in Fig. 7.13 and Fig. 7.15. Apart from differently shaped profiles, a smooth source density does not seem to make any difference in comparison to the constant one aside from the previously stated effects.

Table 7.2: Overview of the set of parameters for the presented results in the case of a magnetic field parallel to the modeled walls.

B_x	B_y	$\widehat{\nu}_\mathrm{ie}$	s_n	$\mathbf{s}_\mathrm{p}$	Figure
0	10	1	Af_cd	$s_\mathrm{n}\mathbf{u}$	7.10
0	0.1	1	Af_cd	$s_\mathrm{n}\mathbf{u}$	7.11
0	1	1	Af_cd	$s_\mathrm{n}\mathbf{u}$	7.12
0	1	1	Af_rcd	$s_\mathrm{n}\mathbf{u}$	7.13
0	1	1	Af_cd	0	7.14
0	1	1	Af_rcd	0	7.15

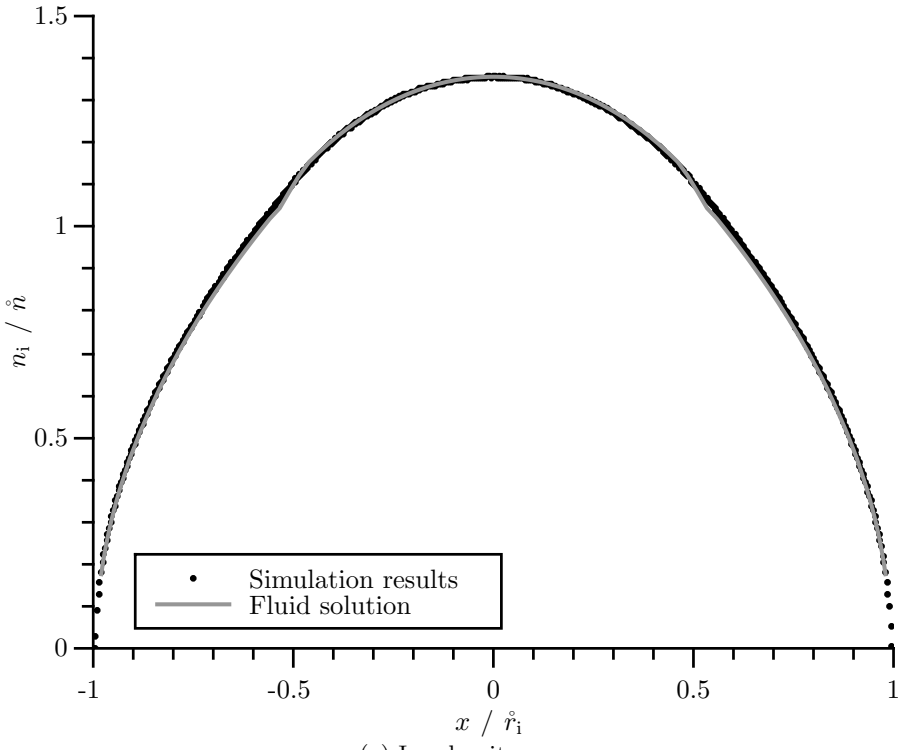

(a) Ion density n_i.

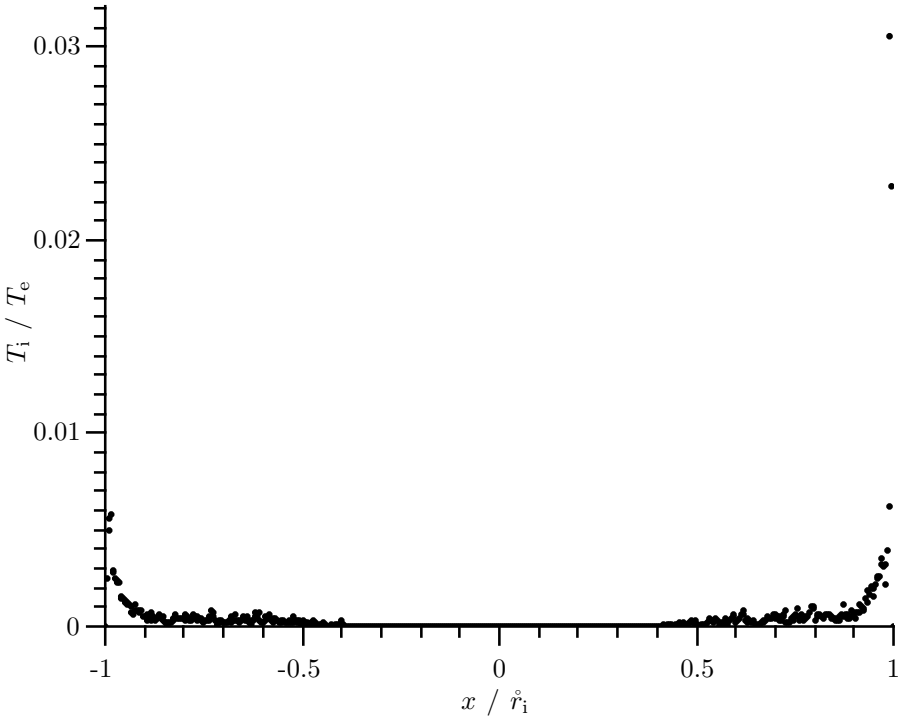

(b) Ion temperature T_i normalized on constant electron temperature T_e.

Figure 7.10: Comparison of profiles from numerical integration of fluid equations with hybrid simulation results with $B_\mathrm{x} = 0,\ B_\mathrm{y} = 10,\ \widehat{\nu}_\mathrm{ie} = 1,\ s_\mathrm{n} = Af_\mathrm{cd}(x),\ \mathbf{s}_\mathrm{p} = s_\mathrm{n}\mathbf{u}$. For the fluid solution the following boundary conditions were used $n_0 = 1.356,\ u_\mathrm{ix0} = 10^{-6},\ u_\mathrm{iz0} = 0,\ (n_\mathrm{i}u_\mathrm{ix})_1 = 0.01195$.

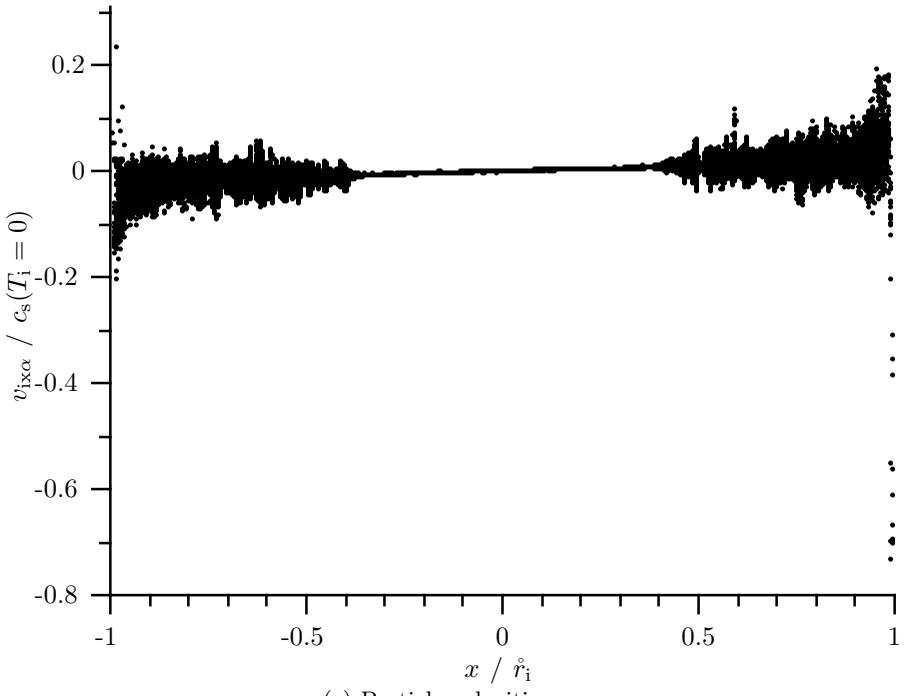

(c) Particle velocities v_{ix}.

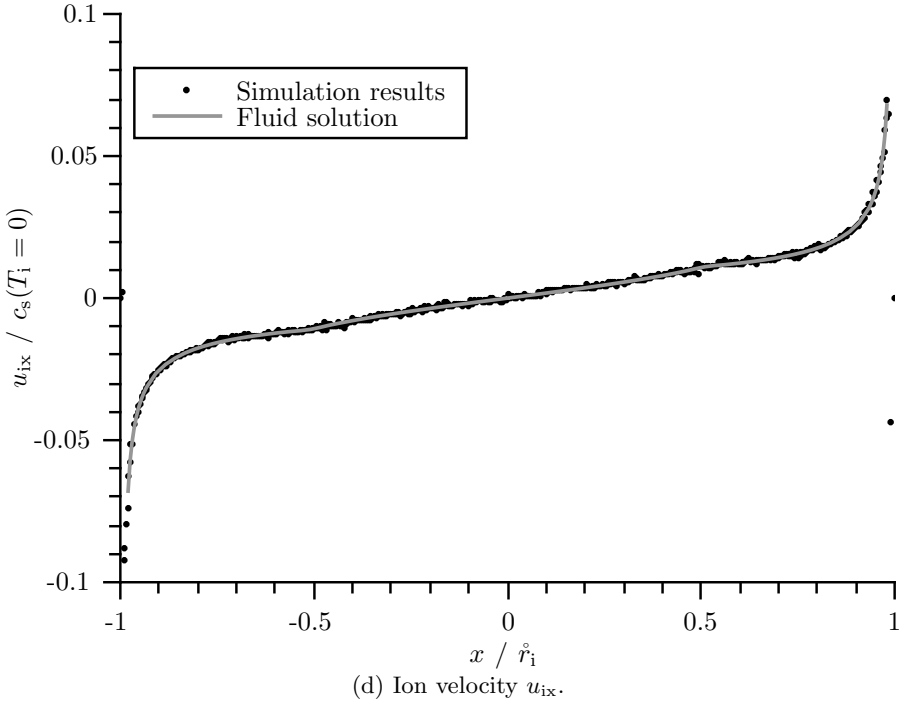

(d) Ion velocity u_{ix}.

Figure 7.10: (continued) Comparison of profiles from numerical integration of fluid equations with hybrid simulation results with $B_{\mathrm{x}} = 0,\ B_{\mathrm{y}} = 10,\ \widehat{\nu}_{\mathrm{ie}} = 1,\ s_{\mathrm{n}} = Af_{\mathrm{cd}}(x),\ \mathbf{s}_{\mathrm{p}} = s_{\mathrm{n}}\mathbf{u}$. For the fluid solution the following boundary conditions were used $n_0 = 1.356,\ u_{\mathrm{ix0}} = 10^{-6},\ u_{\mathrm{iz0}} = 0,\ (n_{\mathrm{i}}u_{\mathrm{ix}})_1 = 0.01195$.

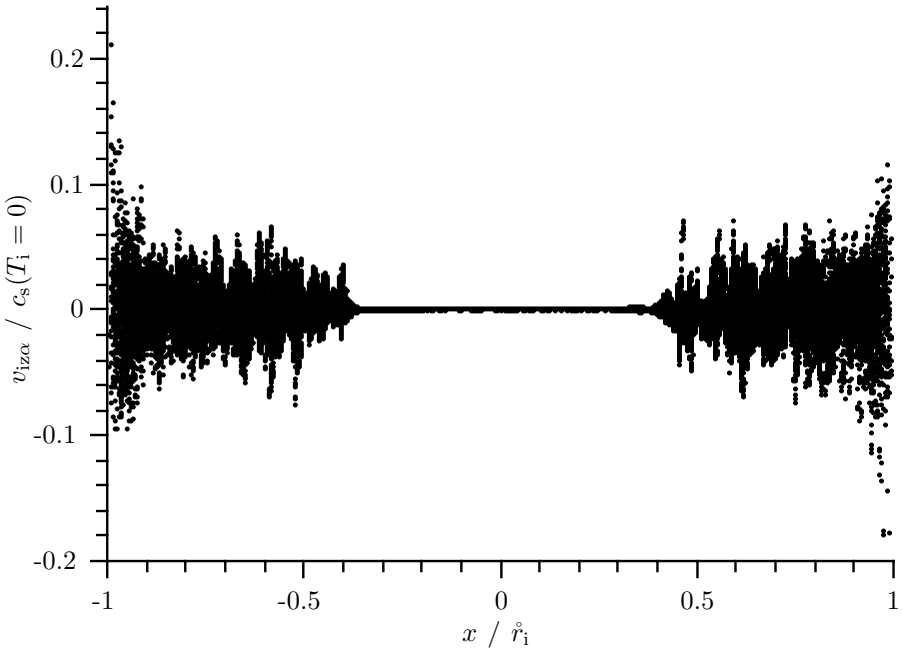

(e) Particle velocities v_{iz}.

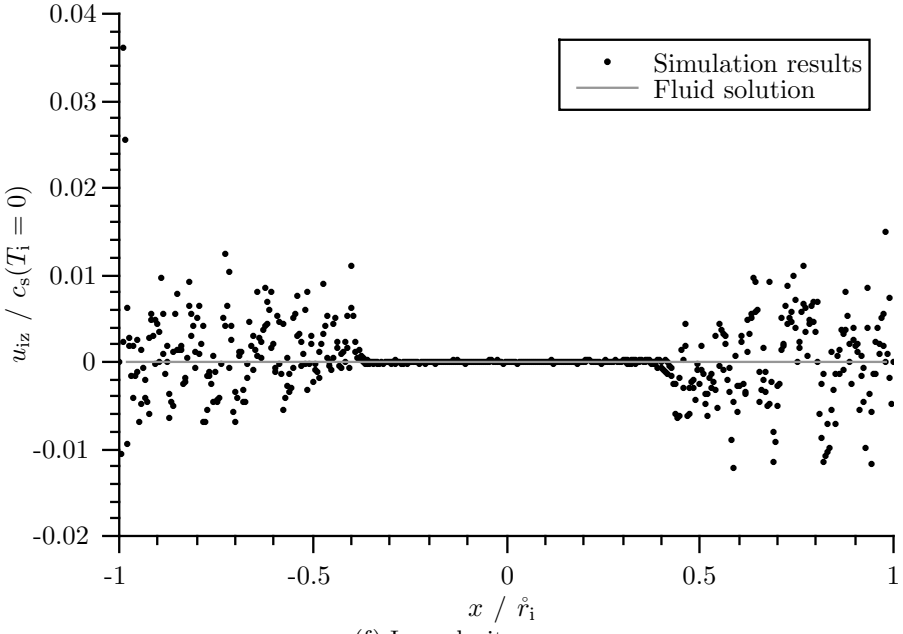

(f) Ion velocity u_{iz}.

Figure 7.10: (continued) Comparison of profiles from numerical integration of fluid equations with hybrid simulation results with $B_{\mathrm{x}} = 0$, $B_{\mathrm{y}} = 10$, $\widehat{\nu}_{\mathrm{ie}} = 1$, $s_{\mathrm{n}} = Af_{\mathrm{cd}}(x)$, $\mathbf{s}_{\mathrm{p}} = s_{\mathrm{n}}\mathbf{u}$. For the fluid solution the following boundary conditions were used $n_0 = 1.356$, $u_{\mathrm{ix0}} = 10^{-6}$, $u_{\mathrm{iz0}} = 0$, $(n_{\mathrm{i}}u_{\mathrm{ix}})_1 = 0.01195$.

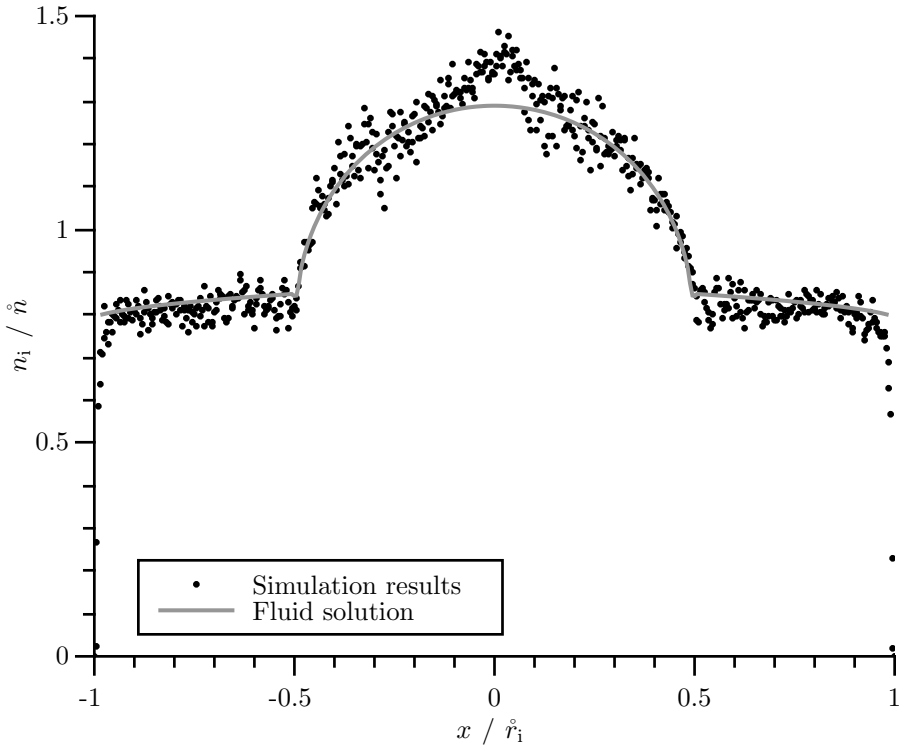

(a) Ion density n_i.

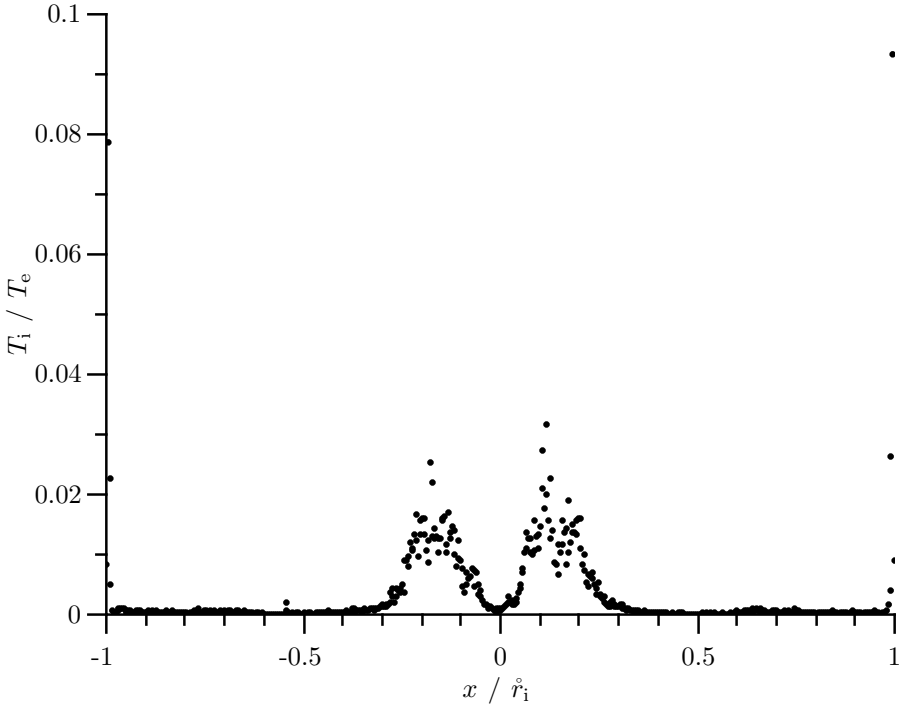

(b) Ion temperature T_i normalized on constant electron temperature T_e.

Figure 7.11: Comparison of profiles from numerical integration of fluid equations with hybrid simulation results with $B_\mathrm{x} = 0$, $B_\mathrm{y} = 0.1$, $\widehat{\nu}_\mathrm{ie} = 1$, $s_\mathrm{n} = Af_\mathrm{cd}(x)$, $\mathbf{s}_\mathrm{p} = s_\mathrm{n}\mathbf{u}$. For the fluid solution the following boundary conditions were used $n_0 = 1.29$, $u_\mathrm{ix0} = 10^{-6}$, $u_\mathrm{iz0l} = 0.0066$, $u_\mathrm{iz0r} = -0.0054$, $(n_\mathrm{i}u_\mathrm{ix})_1 = 0.7851$.

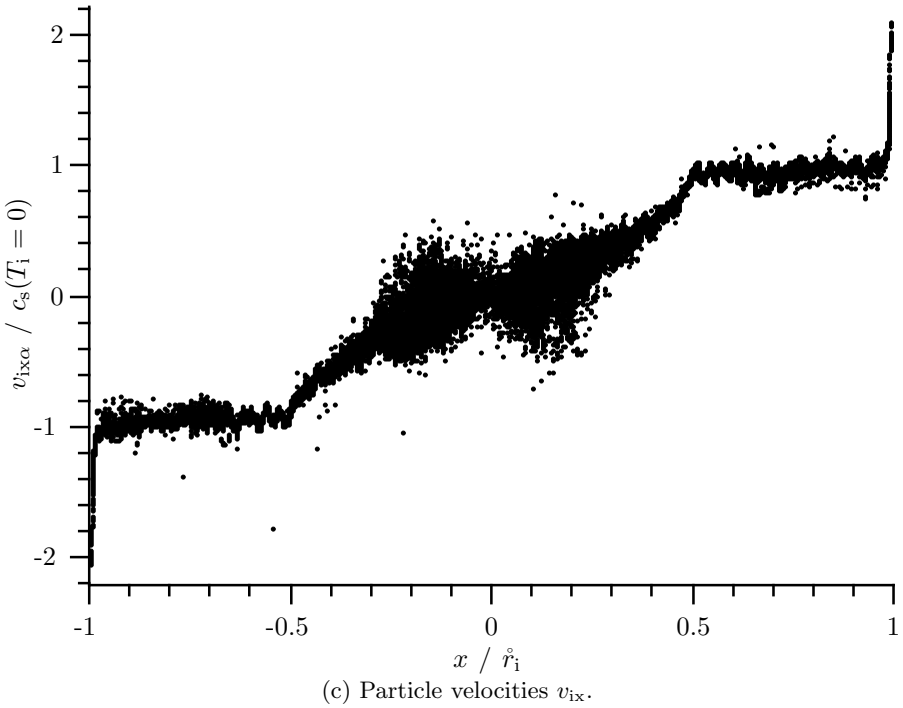

(c) Particle velocities v_{ix}.

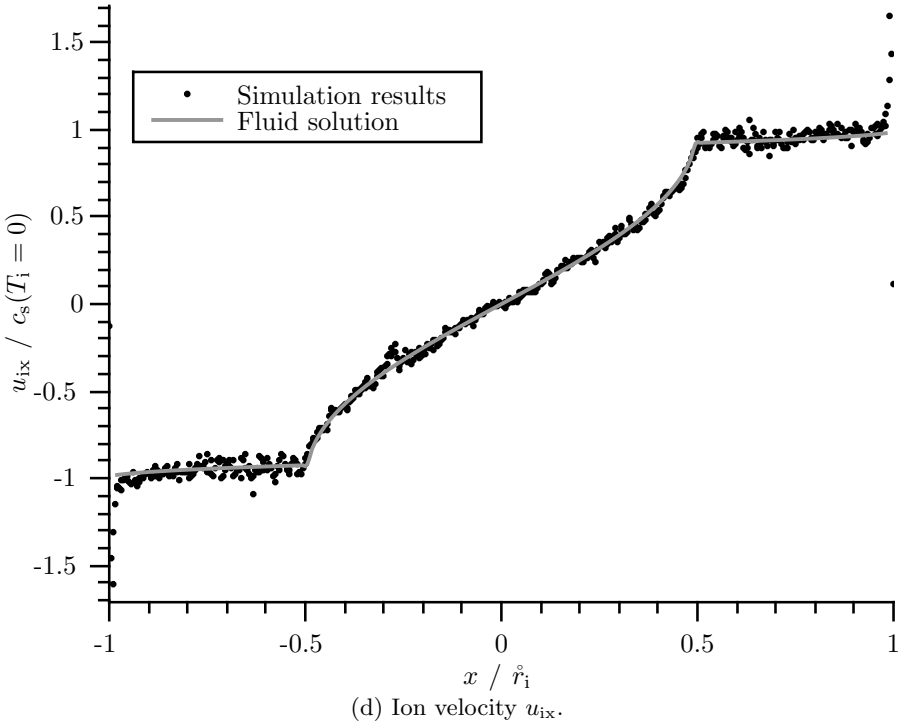

(d) Ion velocity u_{ix}.

Figure 7.11: (continued) Comparison of profiles from numerical integration of fluid equations with hybrid simulation results with $B_{\mathrm{x}} = 0$, $B_{\mathrm{y}} = 0.1$, $\widehat{\nu}_{\mathrm{ie}} = 1$, $s_{\mathrm{n}} = Af_{\mathrm{cd}}(x)$, $\mathbf{s}_{\mathrm{p}} = s_{\mathrm{n}}\mathbf{u}$. For the fluid solution the following boundary conditions were used $n_0 = 1.29$, $u_{\mathrm{ix0}} = 10^{-6}$, $u_{\mathrm{iz0l}} = 0.0066$, $u_{\mathrm{iz0r}} = -0.0054$, $(n_{\mathrm{i}}u_{\mathrm{ix}})_1 = 0.7851$.

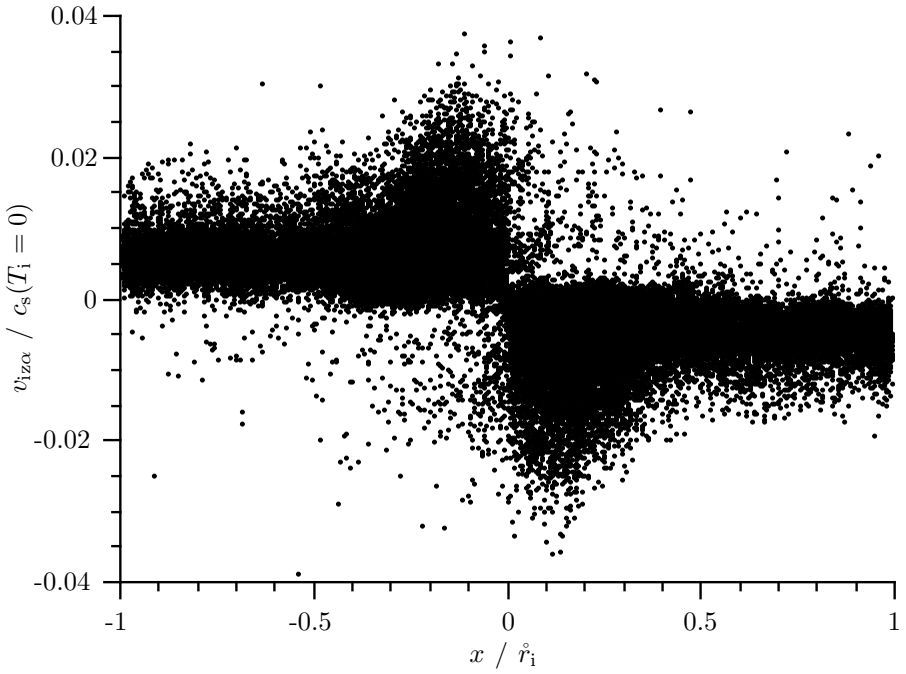

(e) Particle velocities v_{iz}.

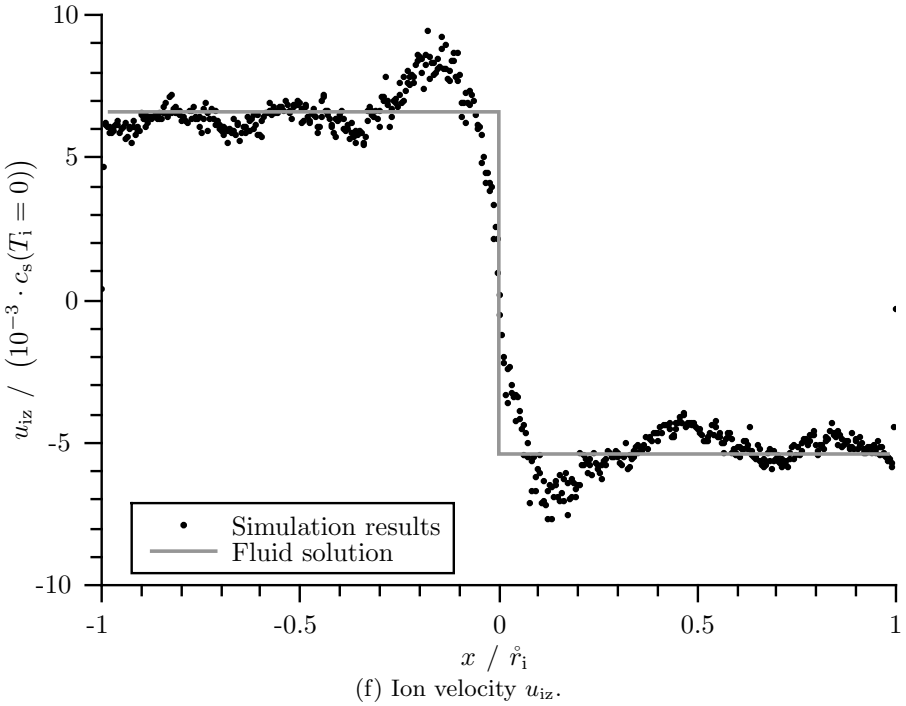

(f) Ion velocity u_{iz}.

Figure 7.11: (continued) Comparison of profiles from numerical integration of fluid equations with hybrid simulation results with $B_{\mathrm{x}} = 0$, $B_{\mathrm{y}} = 0.1$, $\widehat{\nu}_{\mathrm{ie}} = 1$, $s_{\mathrm{n}} = Af_{\mathrm{cd}}(x)$, $\mathbf{s}_{\mathrm{p}} = s_{\mathrm{n}}\mathbf{u}$. For the fluid solution the following boundary conditions were used $n_0 = 1.29$, $u_{\mathrm{ix0}} = 10^{-6}$, $u_{\mathrm{iz0l}} = 0.0066$, $u_{\mathrm{iz0r}} = -0.0054$, $(n_{\mathrm{i}}u_{\mathrm{ix}})_1 = 0.7851$.

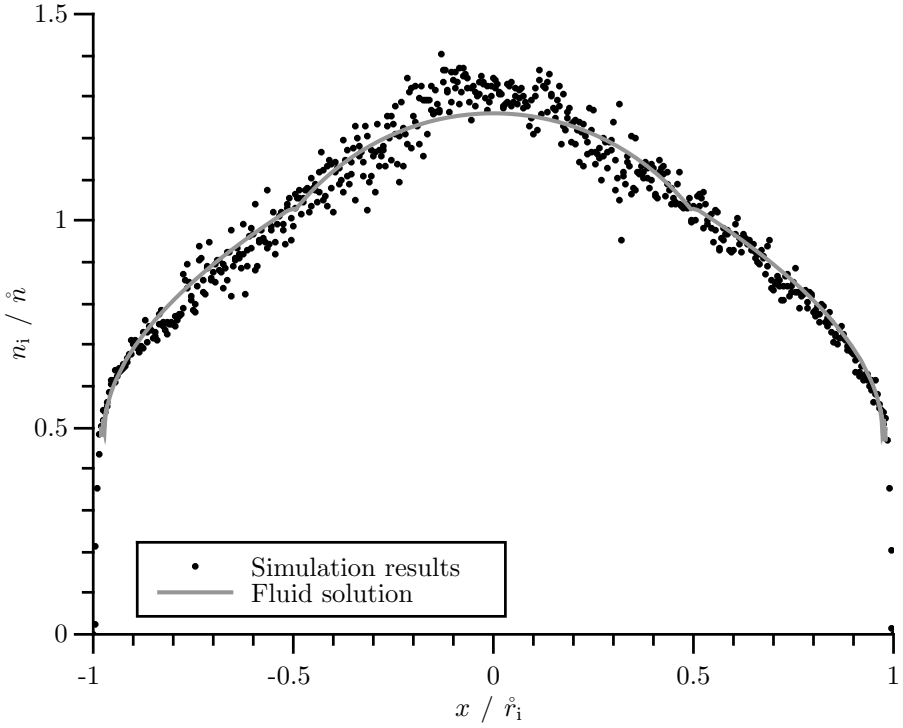

(a) Ion density n_i.

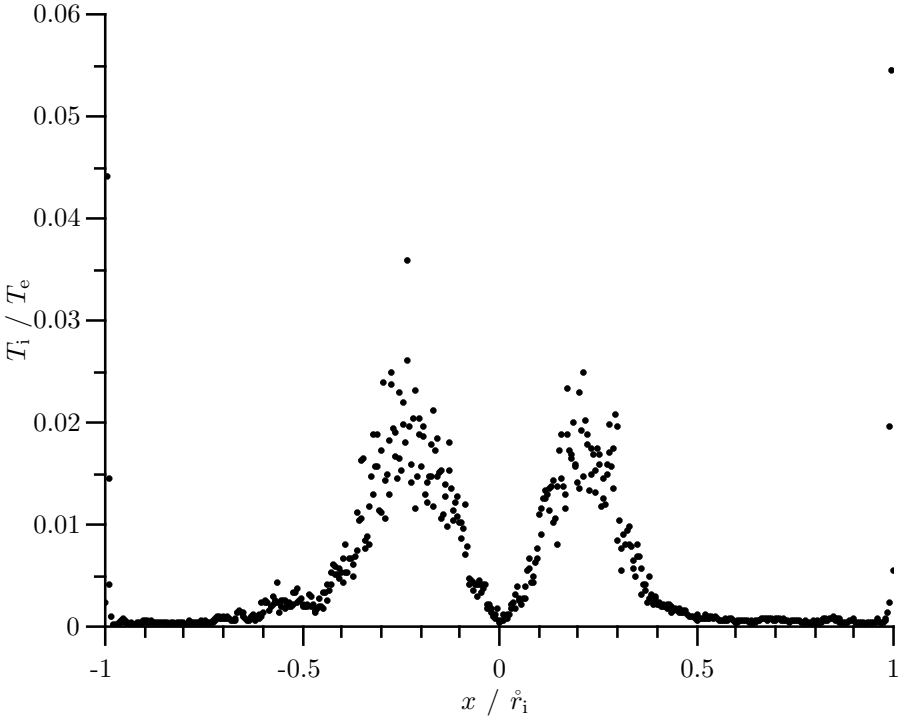

(b) Ion temperature T_i normalized on constant electron temperature T_e.

Figure 7.12: Comparison of profiles from numerical integration of fluid equations with hybrid simulation results with $B_\mathrm{x} = 0$, $B_\mathrm{y} = 1$, $\widehat{\nu}_\mathrm{ie} = 1$, $s_\mathrm{n} = Af_\mathrm{cd}(x)$, $\mathbf{s}_\mathrm{p} = s_\mathrm{n}\mathbf{u}$. For the fluid solution the following boundary conditions were used $n_0 = 1.26$, $u_\mathrm{ix0} = 10^{-6}$, $u_\mathrm{iz0l} = 0.11$, $u_\mathrm{iz0r} = -0.052$, $(n_\mathrm{i}u_\mathrm{ix})_1 = 0.4931$.

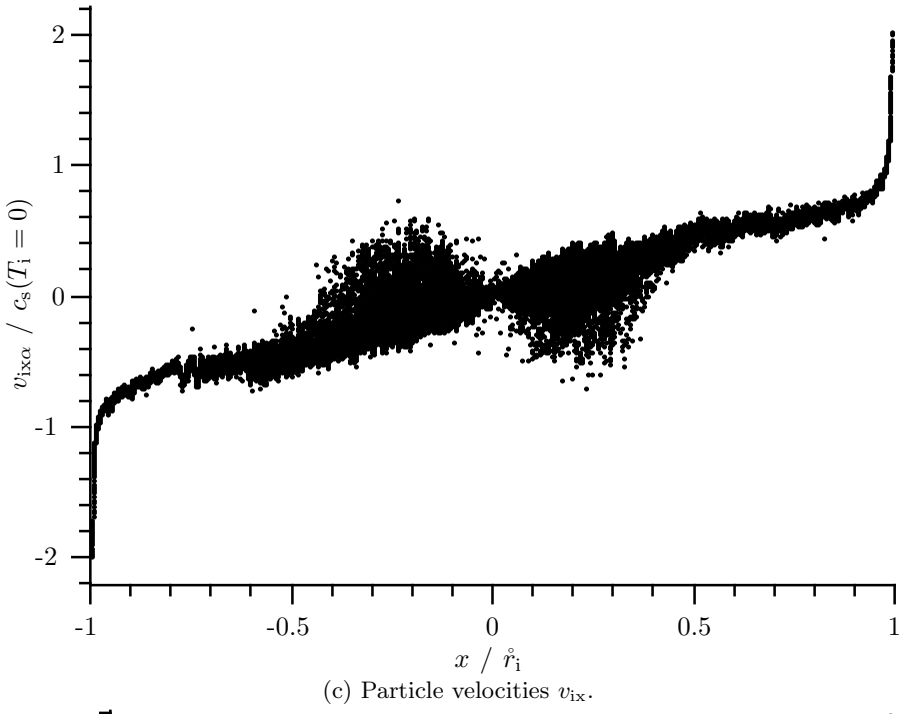

(c) Particle velocities v_{ix}.

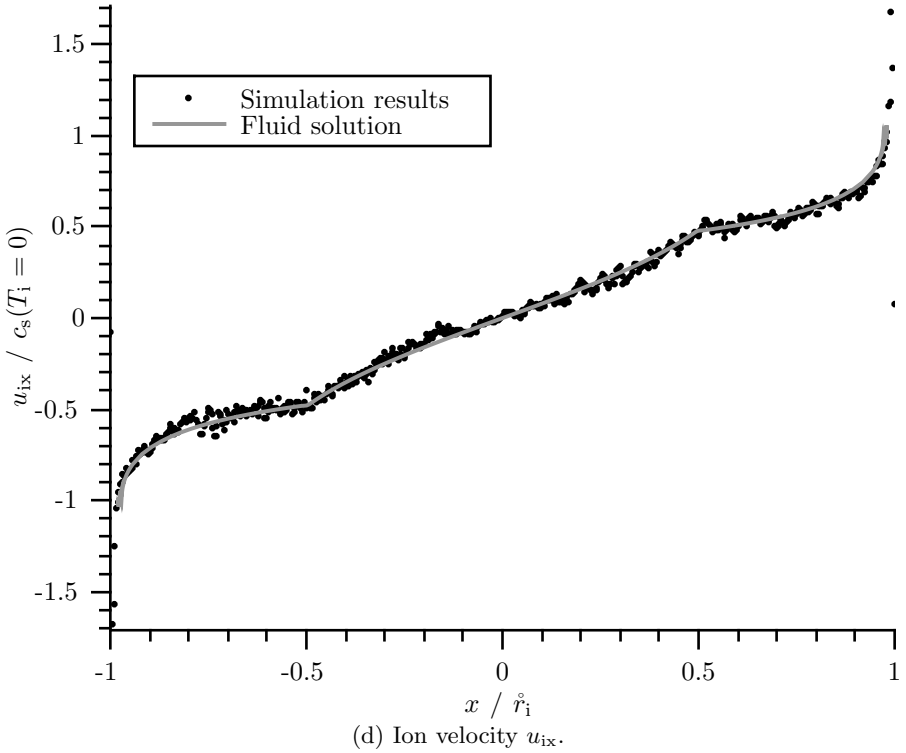

(d) Ion velocity u_{ix}.

Figure 7.12: (continued) Comparison of profiles from numerical integration of fluid equations with hybrid simulation results with $B_x = 0$, $B_y = 1$, $\widehat{\nu}_{ie} = 1$, $s_n = Af_{cd}(x)$, $\mathbf{s}_p = s_n\mathbf{u}$. For the fluid solution the following boundary conditions were used $n_0 = 1.26$, $u_{ix0} = 10^{-6}$, $u_{iz0l} = 0.11$, $u_{iz0r} = -0.052$, $(n_i u_{ix})_1 = 0.4931$.

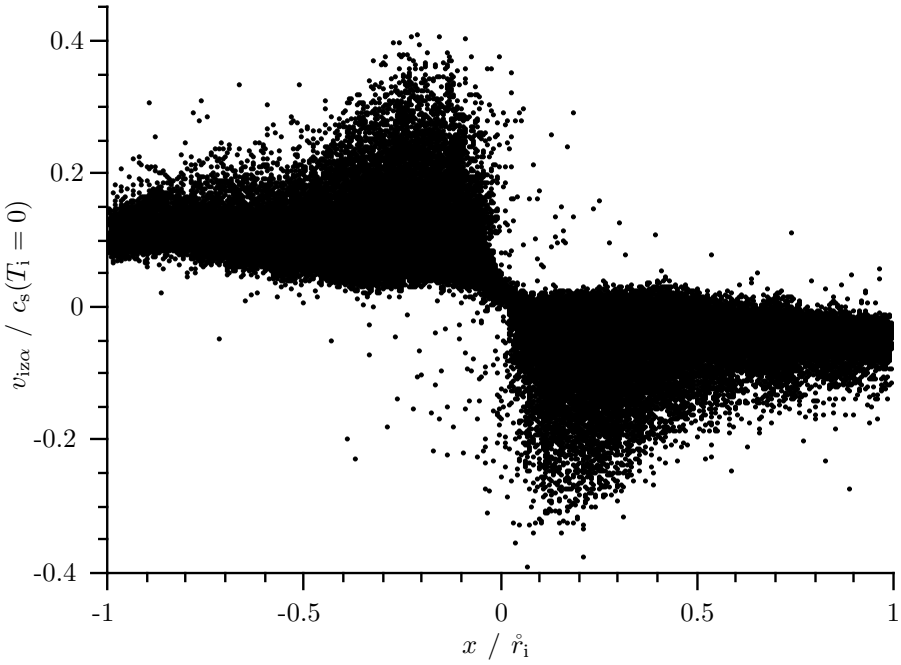

(e) Particle velocities v_{iz}.

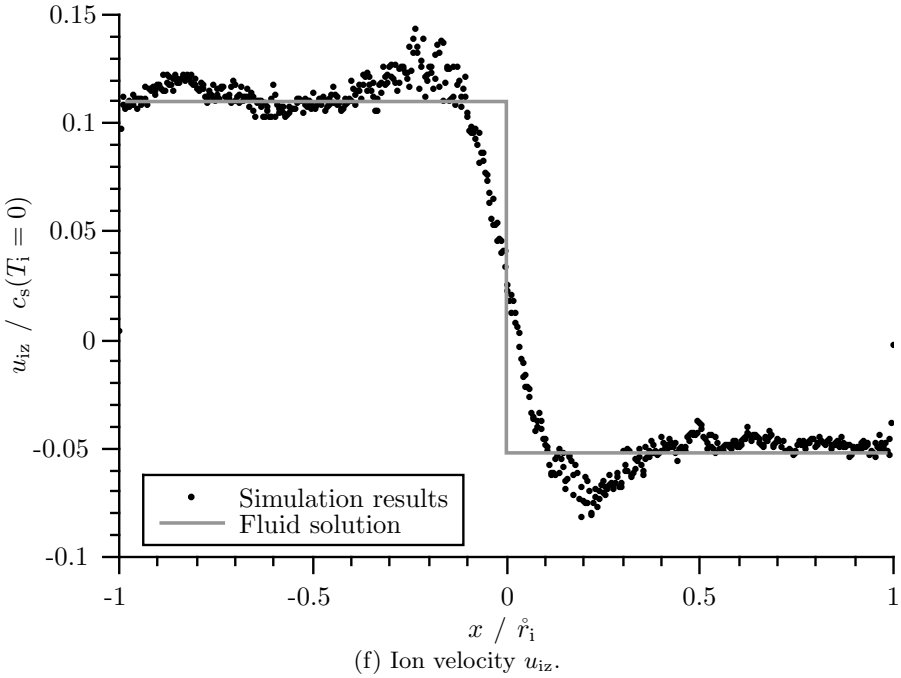

(f) Ion velocity u_{iz}.

Figure 7.12: (continued) Comparison of profiles from numerical integration of fluid equations with hybrid simulation results with $B_{\mathrm{x}} = 0$, $B_{\mathrm{y}} = 1$, $\widehat{\nu}_{\mathrm{ie}} = 1$, $s_{\mathrm{n}} = Af_{\mathrm{cd}}(x)$, $\mathbf{s}_{\mathrm{p}} = s_{\mathrm{n}}\mathbf{u}$. For the fluid solution the following boundary conditions were used $n_0 = 1.26$, $u_{\mathrm{ix0}} = 10^{-6}$, $u_{\mathrm{iz0l}} = 0.11$, $u_{\mathrm{iz0r}} = -0.052$, $(n_{\mathrm{i}}u_{\mathrm{ix}})_1 = 0.4931$.

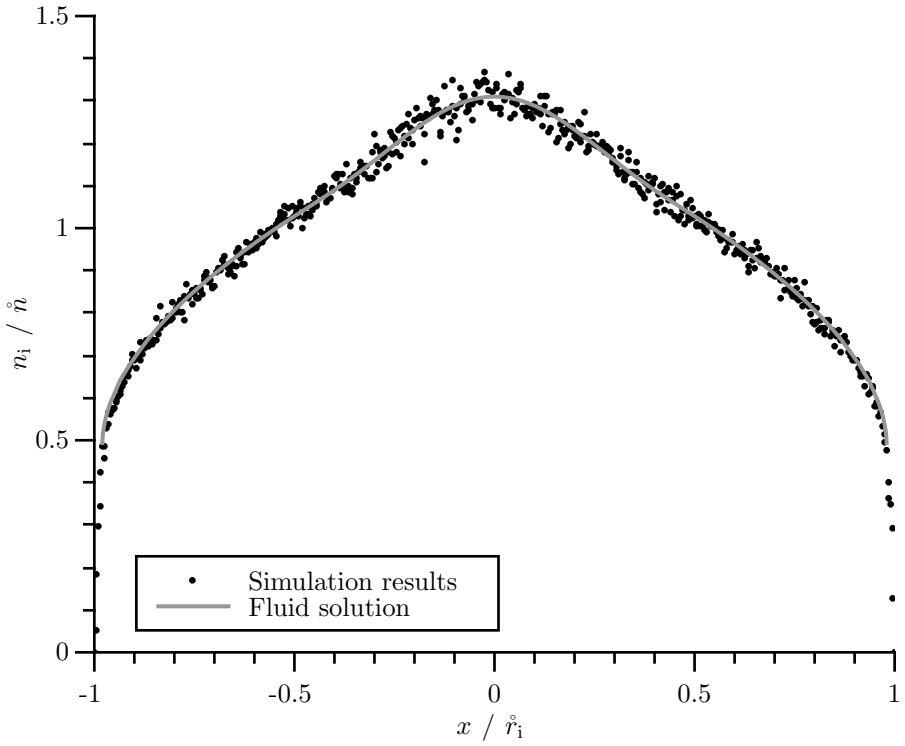

(a) Ion density n_i.

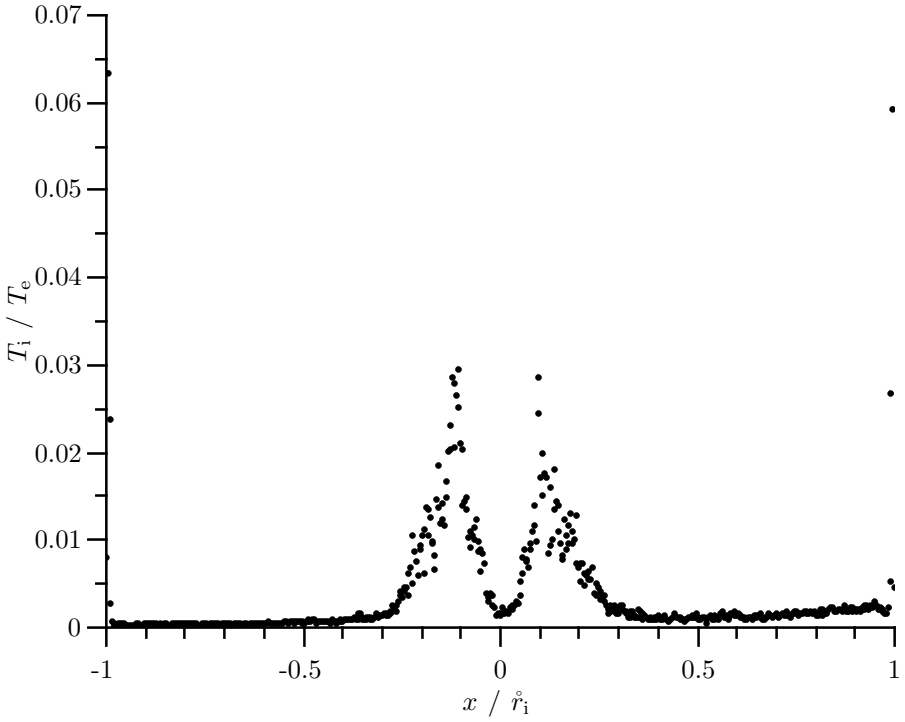

(b) Ion temperature T_i normalized on constant electron temperature T_e.

Figure 7.13: Comparison of profiles from numerical integration of fluid equations with hybrid simulation results with $B_\mathrm{x} = 0$, $B_\mathrm{y} = 1$, $\widehat{\nu}_\mathrm{ie} = 1$, $s_\mathrm{n} = Af_\mathrm{rcd}(x)$, $\mathbf{s}_\mathrm{p} = s_\mathrm{n}\mathbf{u}$. For the fluid solution the following boundary conditions were used $n_0 = 1.31$, $u_\mathrm{ix0} = 10^{-6}$, $u_\mathrm{iz0l} = 0.082$, $u_\mathrm{iz0r} = -0.021$, $(n_\mathrm{i}u_\mathrm{ix})_1 = 0.4862$.

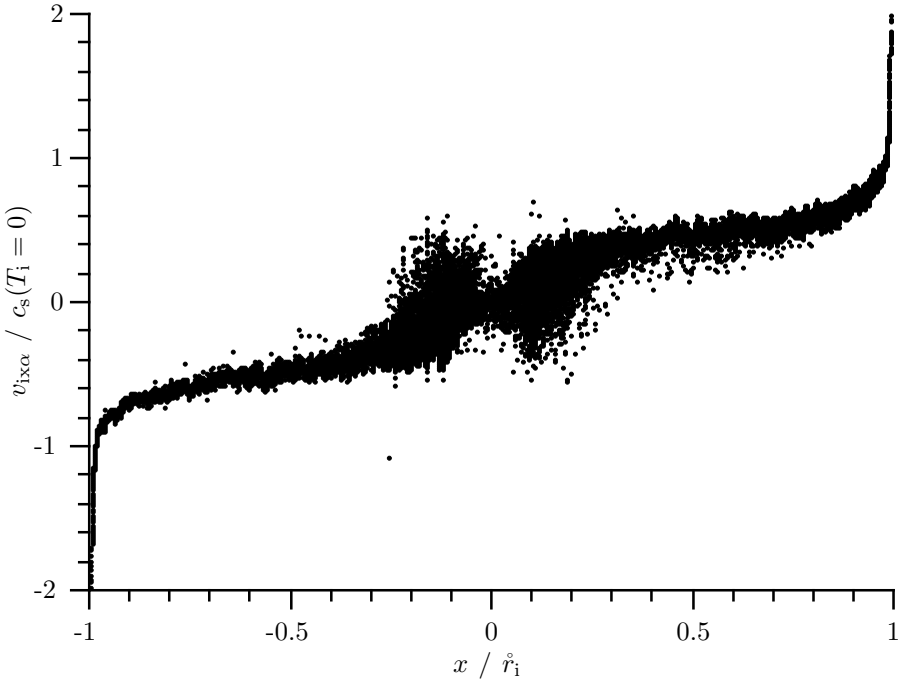

(c) Particle velocities v_{ix}.

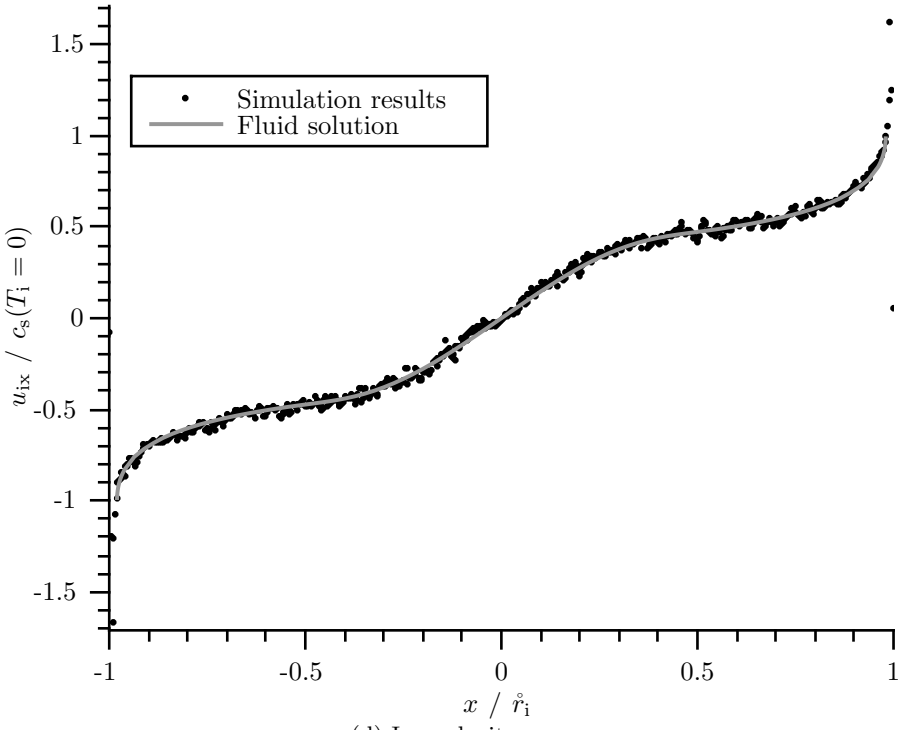

(d) Ion velocity u_{ix}.

Figure 7.13: (continued) Comparison of profiles from numerical integration of fluid equations with hybrid simulation results with $B_{\mathrm{x}} = 0$, $B_{\mathrm{y}} = 1$, $\widehat{\nu}_{\mathrm{ie}} = 1$, $s_{\mathrm{n}} = A f_{\mathrm{rcd}}(x)$, $\mathbf{s}_{\mathrm{p}} = s_{\mathrm{n}}\mathbf{u}$. For the fluid solution the following boundary conditions were used $n_0 = 1.31$, $u_{\mathrm{ix0}} = 10^{-6}$, $u_{\mathrm{iz0l}} = 0.082$, $u_{\mathrm{iz0r}} = -0.021$, $(n_{\mathrm{i}} u_{\mathrm{ix}})_1 = 0.4862$.

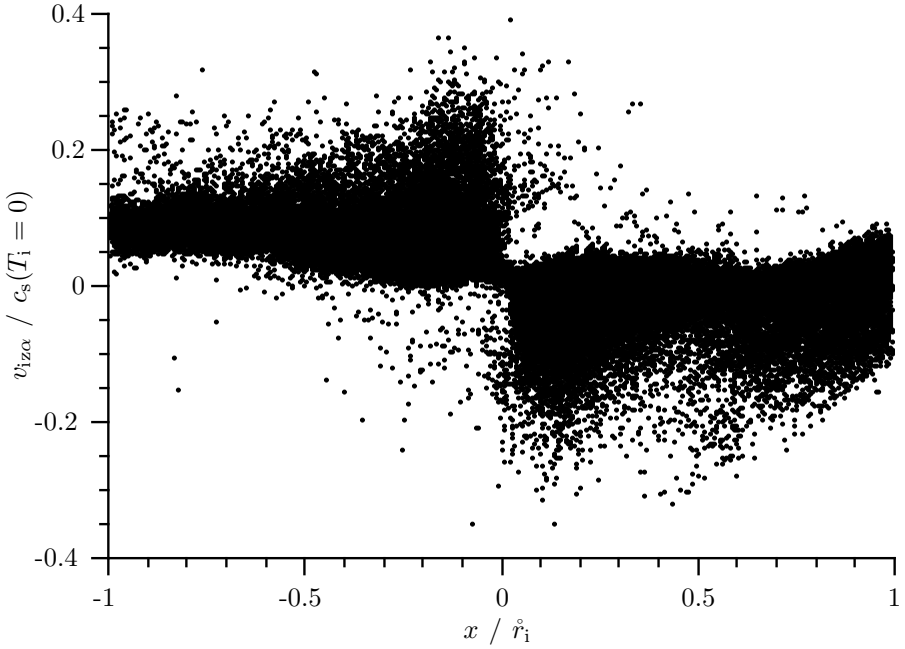

(e) Particle velocities v_{iz}.

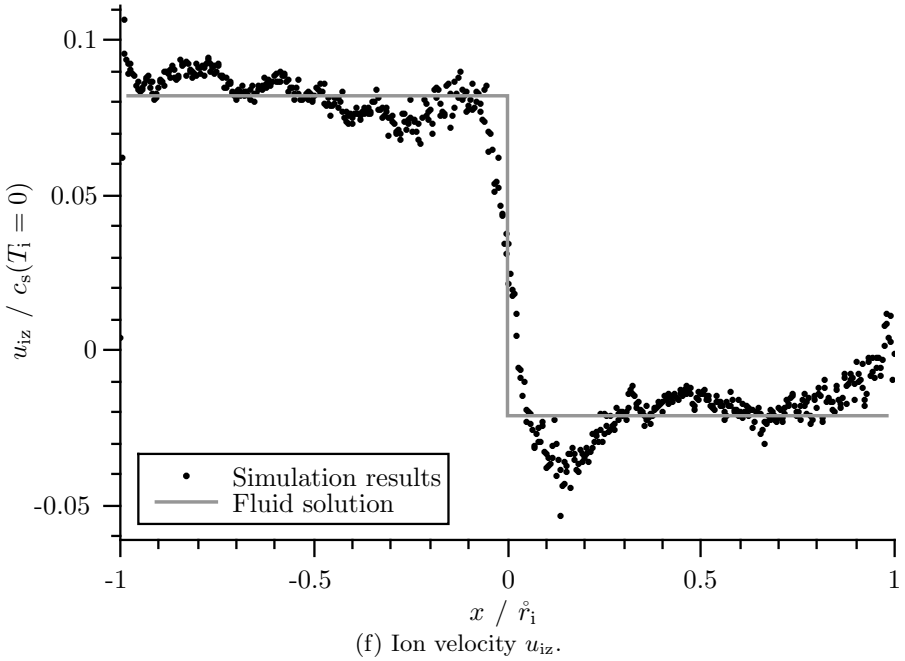

(f) Ion velocity u_{iz}.

Figure 7.13: (continued) Comparison of profiles from numerical integration of fluid equations with hybrid simulation results with $B_{\mathrm{x}} = 0$, $B_{\mathrm{y}} = 1$, $\widehat{\nu}_{\mathrm{ie}} = 1$, $s_{\mathrm{n}} = Af_{\mathrm{rcd}}(x)$, $\mathbf{s}_{\mathrm{p}} = s_{\mathrm{n}}\mathbf{u}$. For the fluid solution the following boundary conditions were used $n_0 = 1.31$, $u_{\mathrm{ix0}} = 10^{-6}$, $u_{\mathrm{iz0l}} = 0.082$, $u_{\mathrm{iz0r}} = -0.021$, $(n_{\mathrm{i}}u_{\mathrm{ix}})_1 = 0.4862$.

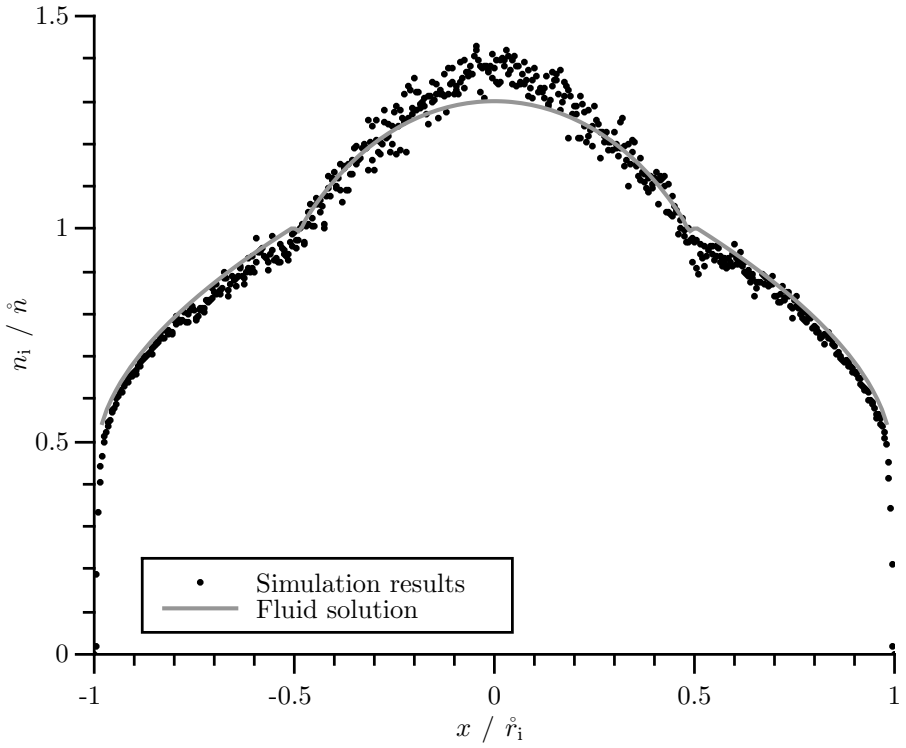

(a) Ion density n_i.

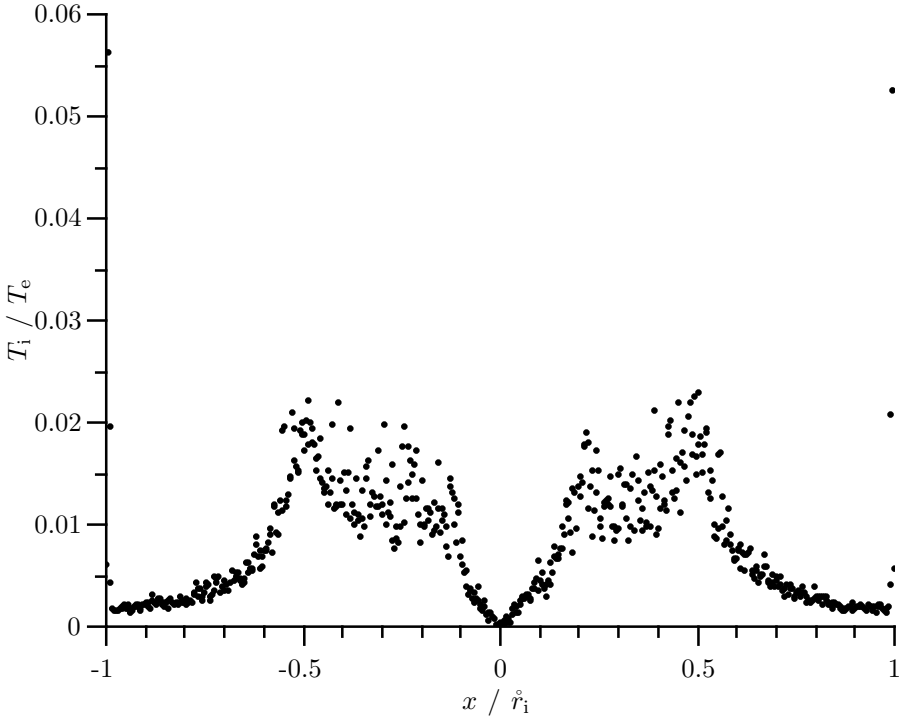

(b) Ion temperature T_i normalized on constant electron temperature T_e.

Figure 7.14: Comparison of profiles from numerical integration of fluid equations with hybrid simulation results with $B_\mathrm{x} = 0,\ B_\mathrm{y} = 1,\ \widehat{\nu}_\mathrm{ie} = 1,\ s_\mathrm{n} = Af_\mathrm{cd}(x),\ \mathbf{s}_\mathrm{p} = 0$. For the fluid solution the following boundary conditions were used $n_0 = 1.3,\ u_\mathrm{ix0} = 10^{-6},\ u_\mathrm{iz0} = 0,\ (n_\mathrm{i}u_\mathrm{ix})_1 = 0.4661$.

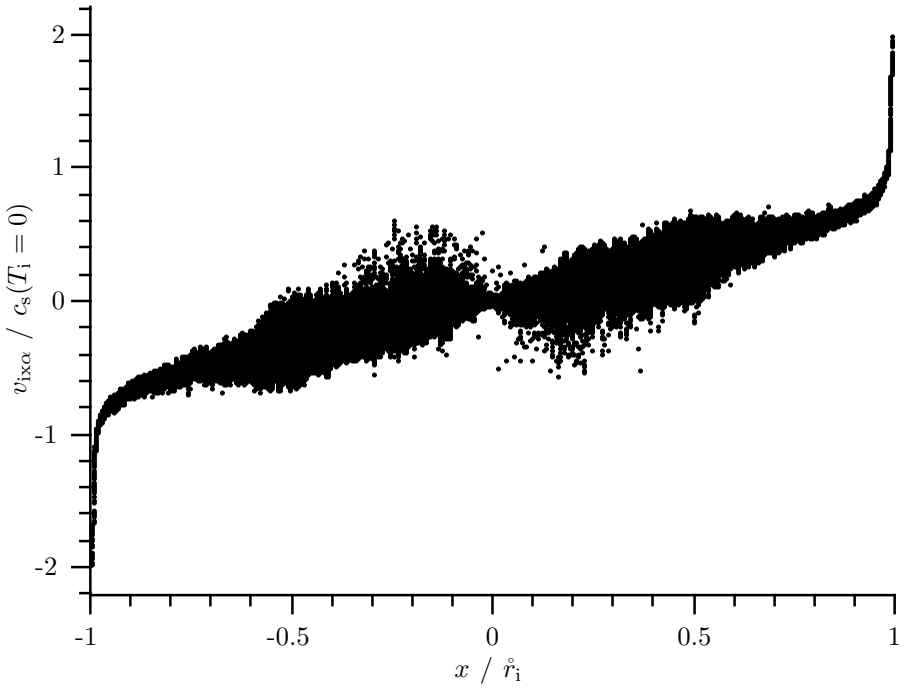

(c) Particle velocities v_{ix}.

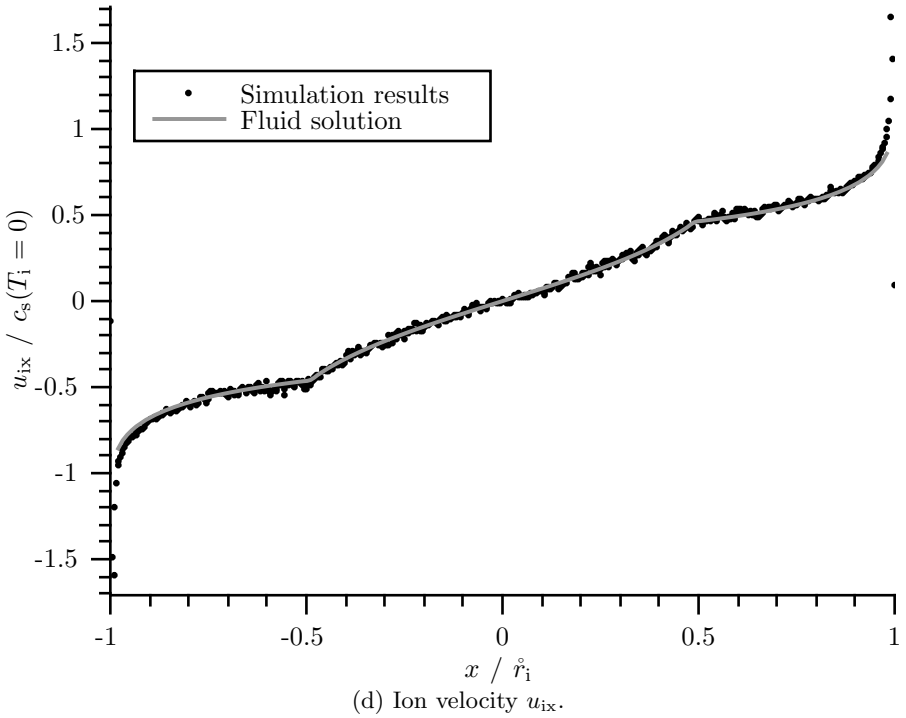

(d) Ion velocity u_{ix}.

Figure 7.14: (continued) Comparison of profiles from numerical integration of fluid equations with hybrid simulation results with $B_{\mathrm{x}} = 0,\ B_{\mathrm{y}} = 1,\ \widehat{\nu}_{\mathrm{ie}} = 1,\ s_{\mathrm{n}} = Af_{\mathrm{cd}}(x),\ \mathbf{s}_{\mathrm{p}} = 0$. For the fluid solution the following boundary conditions were used $n_0 = 1.3,\ u_{\mathrm{ix0}} = 10^{-6},\ u_{\mathrm{iz0}} = 0,\ (n_{\mathrm{i}}u_{\mathrm{ix}})_1 = 0.4661$.

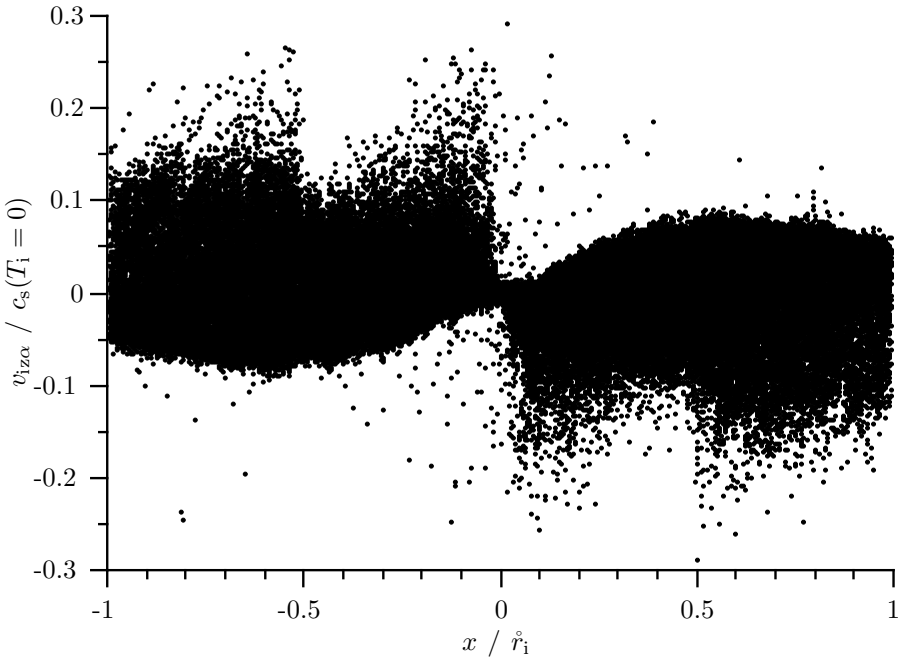

(e) Particle velocities v_{iz}.

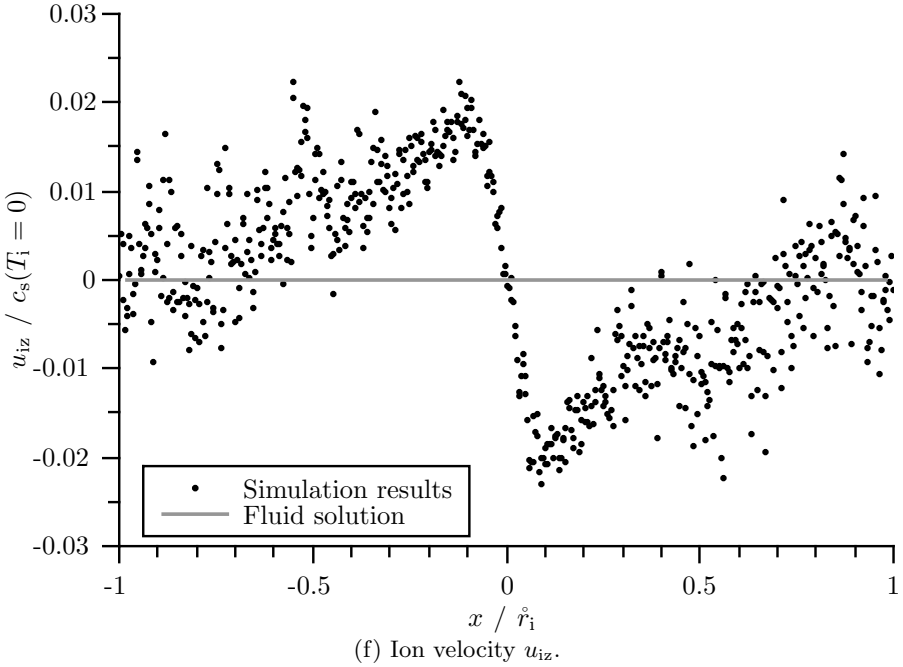

(f) Ion velocity u_{iz}.

Figure 7.14: (continued) Comparison of profiles from numerical integration of fluid equations with hybrid simulation results with $B_{\mathrm{x}} = 0,\ B_{\mathrm{y}} = 1,\ \widehat{\nu}_{\mathrm{ie}} = 1,\ s_{\mathrm{n}} = Af_{\mathrm{cd}}(x),\ \mathbf{s}_{\mathrm{p}} = 0$. For the fluid solution the following boundary conditions were used $n_0 = 1.3,\ u_{\mathrm{ix0}} = 10^{-6},\ u_{\mathrm{iz0}} = 0,\ (n_{\mathrm{i}}u_{\mathrm{ix}})_1 = 0.4661$.

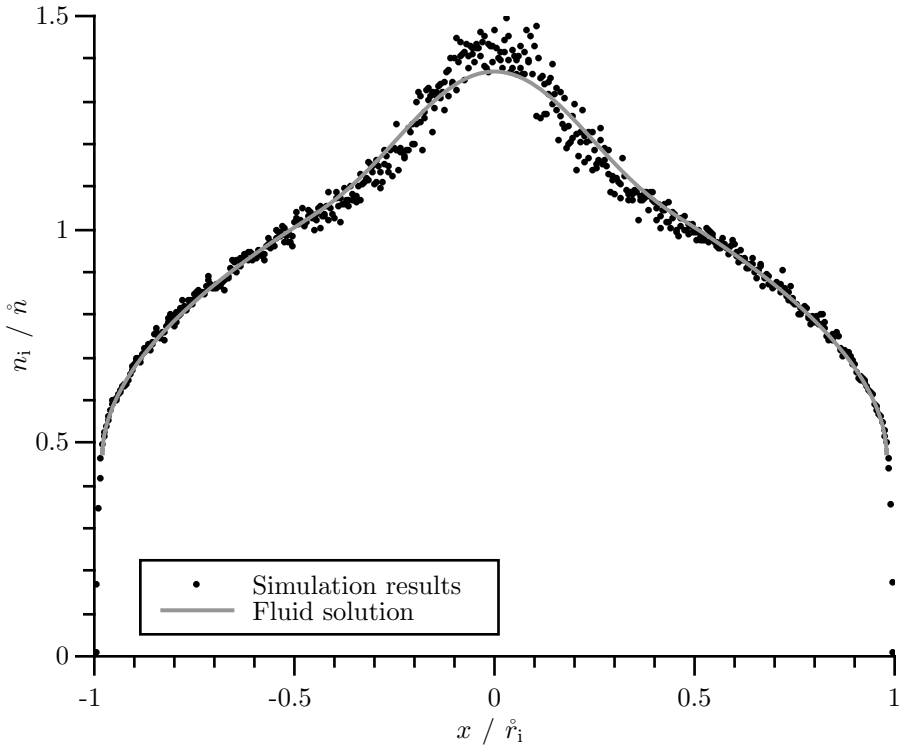

(a) Ion density n_i.

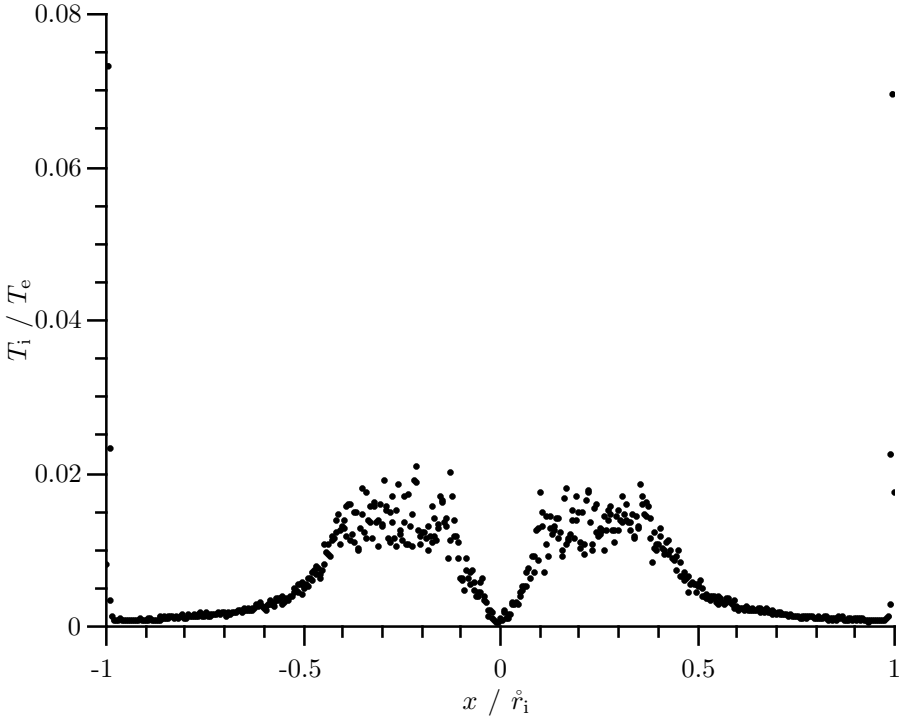

(b) Ion temperature T_i normalized on constant electron temperature T_e.

Figure 7.15: Comparison of profiles from numerical integration of fluid equations with hybrid simulation results with $B_\mathrm{x} = 0,\ B_\mathrm{y} = 1,\ \widehat{\nu}_\mathrm{ie} = 1,\ s_\mathrm{n} = Af_\mathrm{rcd}(x),\ \mathbf{s}_\mathrm{p} = 0$. For the fluid solution the following boundary conditions were used $n_0 = 1.37,\ u_\mathrm{ix0} = 10^{-6},\ u_\mathrm{iz0} = 0,\ (n_\mathrm{i}u_\mathrm{ix})_1 = 0.4708$.

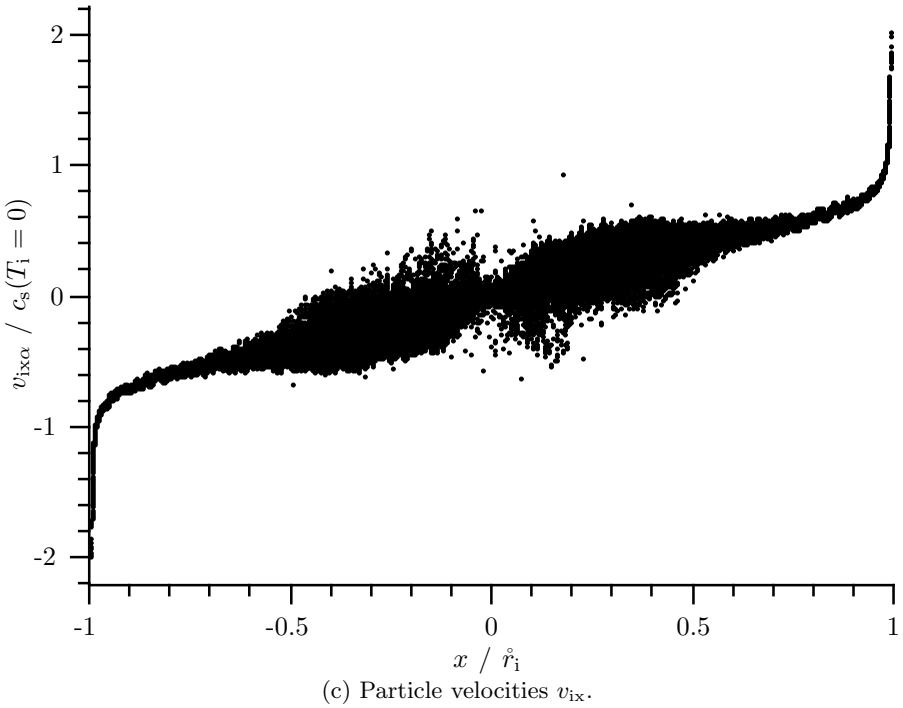

(c) Particle velocities v_{ix}.

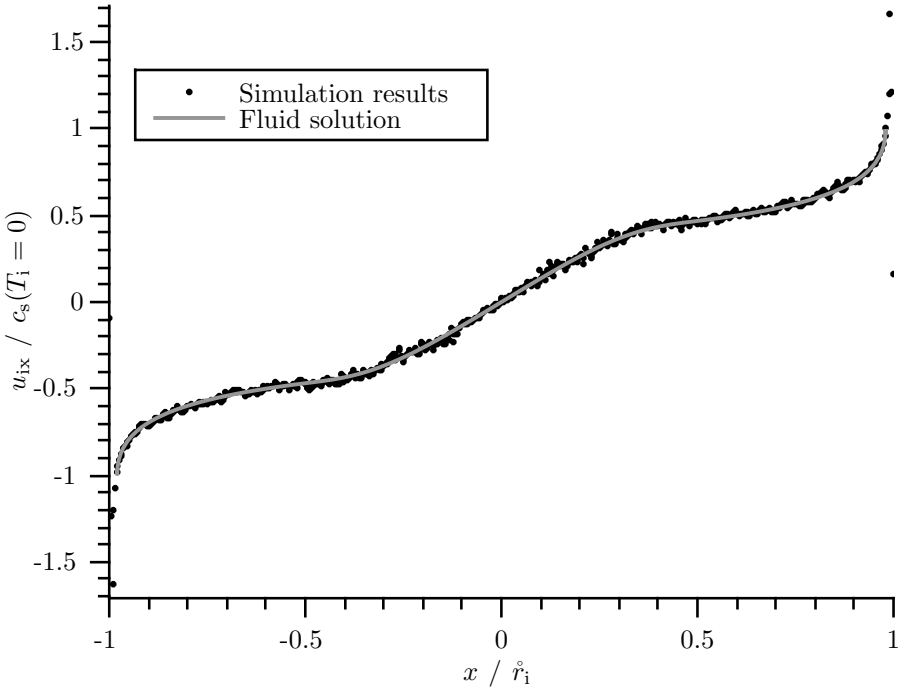

(d) Ion velocity u_{ix}.

Figure 7.15: (continued) Comparison of profiles from numerical integration of fluid equations with hybrid simulation results with $B_{\mathrm{x}} = 0,\ B_{\mathrm{y}} = 1,\ \widehat{\nu}_{\mathrm{ie}} = 1,\ s_{\mathrm{n}} = Af_{\mathrm{rcd}}(x),\ \mathbf{s}_{\mathrm{p}} = 0$. For the fluid solution the following boundary conditions were used $n_0 = 1.37,\ u_{\mathrm{ix0}} = 10^{-6},\ u_{\mathrm{iz0}} = 0,\ (n_{\mathrm{i}}u_{\mathrm{ix}})_1 = 0.4708$.

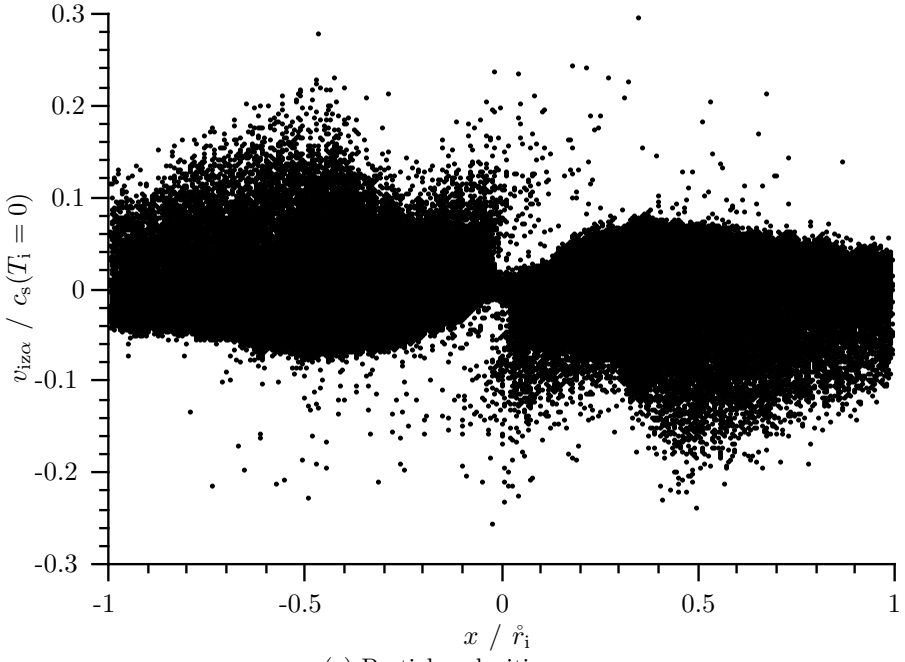

(e) Particle velocities v_{iz}.

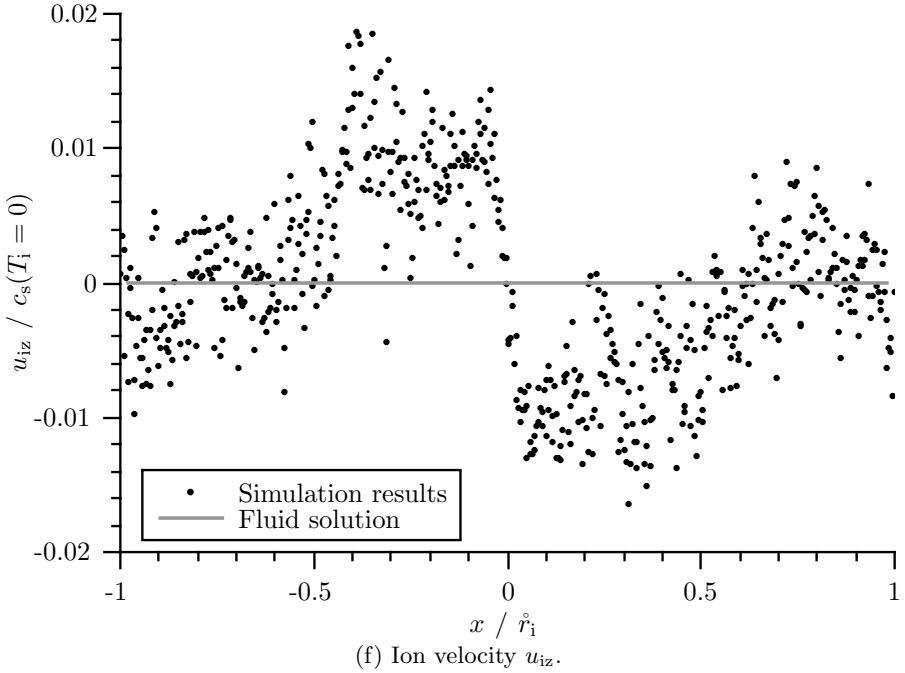

(f) Ion velocity u_{iz}.

Figure 7.15: (continued) Comparison of profiles from numerical integration of fluid equations with hybrid simulation results with $B_{\mathrm{x}} = 0,\ B_{\mathrm{y}} = 1,\ \widehat{\nu}_{\mathrm{ie}} = 1,\ s_{\mathrm{n}} = Af_{\mathrm{rcd}}(x),\ \mathbf{s}_{\mathrm{p}} = 0$. For the fluid solution the following boundary conditions were used $n_0 = 1.37,\ u_{\mathrm{ix0}} = 10^{-6},\ u_{\mathrm{iz0}} = 0,\ (n_{\mathrm{i}}u_{\mathrm{ix}})_1 = 0.4708$.

7.3 Considering an arbitrary magnetic field

For this case the whole system of differential equations (4.10), (4.11) and (4.12), along with the electron velocities (4.13), (4.14) and (4.15) needs to be considered. Due to complexity by the high coupling of the equations, an analytical approach to solve them is waived here. Instead the numerical results are directly provided with the simulation results in the following section.

7.3.1 Hybrid simulation results

To investigate the effect of the x–component of the magnetic field B_x, it will be varied in the following considerations. To be more precise, the absolute value of the magnetic field B is kept constant, while its impact angle α on the wall surface is varied.

$$B_\mathrm{x} = B\cos(\alpha) \qquad\qquad B_\mathrm{y} = B\sin(\alpha)$$

In the following, simulation results are presented with a constant ionization source density $s_\mathrm{n} = Af_\mathrm{cd}$, because no additional characteristics have been identified with the smooth cosine–shaped one, even with a magnetic parallel to the walls. The impact angle α as well as the magnetic field strength B will be altered, while ionization from a comoving neutral gas background is considered. For comparison simulations are repeated with ionization from a resting neutral gas background just for one case of the above chosen magnetic fields.

Again apart from differently shaped profiles and the previously presented deviations from the fluid solutions, the hybrid simulation results coincide as expected with those of the numerical integration of the fluid equations for the weakly magnetized cases in Fig. 7.16 to 7.19.

For strongly magnetized plasmas, the simulation run with a small impact angle α, whose results are displayed in Fig. 7.20, resembles the fluid solution as anticipated. The simulation results for a high impact angle α, displayed in Fig. 7.21, appear very noisy, but still describe the fluid results. Interestingly the shapes of the average velocity in z–direction u_iz are similar for both the hybrid and fluid results here, although they do not look intuitive at all.

Table 7.3: Overview of the set of parameters for the presented results in the case of an arbitrary magnetic field.

B	α	$\widehat{\nu}_{\mathrm{ie}}$	s_{n}	$\mathbf{s}_{\mathrm{p}}$	Figure
1	5°	1	Af_{cd}	$s_{\mathrm{n}}\mathbf{u}$	7.16
1	45°	1	Af_{cd}	$s_{\mathrm{n}}\mathbf{u}$	7.17
1	5°	1	Af_{cd}	0	7.18
1	45°	1	Af_{cd}	0	7.19
10	5°	1	Af_{cd}	$s_{\mathrm{n}}\mathbf{u}$	7.20
10	45°	1	Af_{cd}	$s_{\mathrm{n}}\mathbf{u}$	7.21

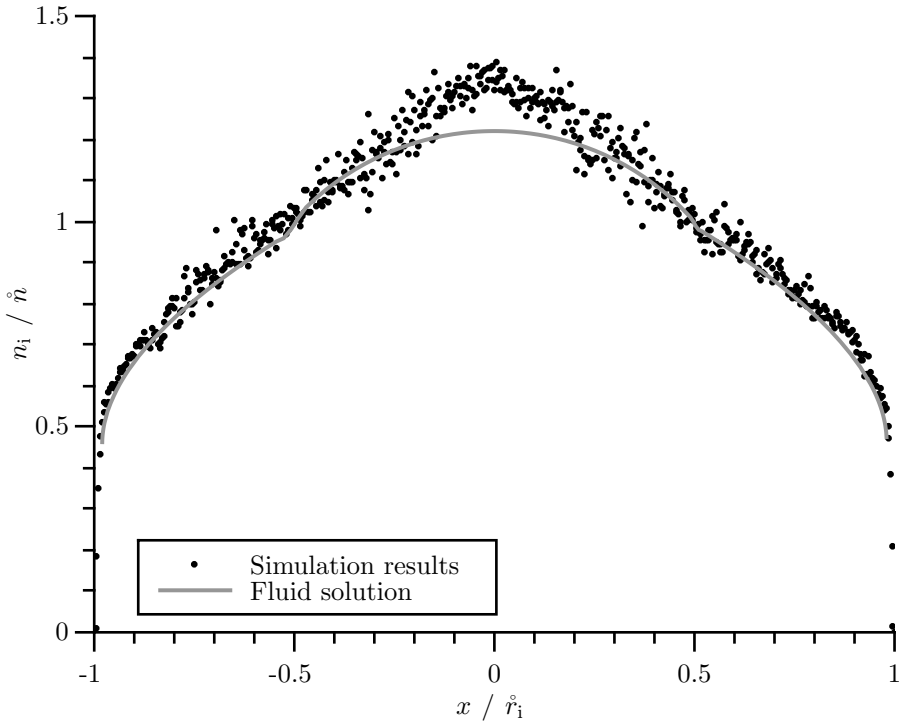

(a) Ion density n_i.

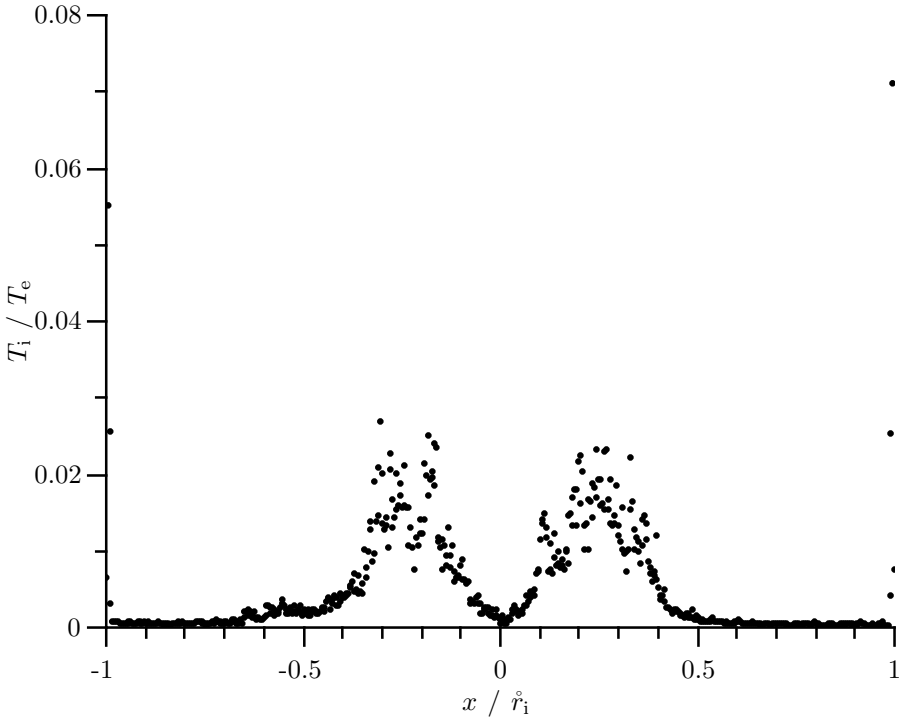

(b) Ion temperature T_i normalized on constant electron temperature T_e.

Figure 7.16: Comparison of profiles from numerical integration of fluid equations with hybrid simulation results with $B = 1$, $\alpha = 5°$, $\widehat{\nu}_\mathrm{ie} = 1$, $s_\mathrm{n} = Af_\mathrm{cd}(x)$, $\mathbf{s}_\mathrm{p} = s_\mathrm{n}\mathbf{u}$. For the fluid solution the following boundary conditions were used $n_0 = 1.22$, $u_\mathrm{ix0} = 10^{-6}$, $u_\mathrm{iy0} = 0$, $u_\mathrm{iz0l} = 0.058$, $(n_\mathrm{i}u_\mathrm{ix})_\mathrm{1l} = -0.4589$, $u_\mathrm{iz0r} = -0.12$, $(n_\mathrm{i}u_\mathrm{ix})_\mathrm{1r} = 0.4648$.

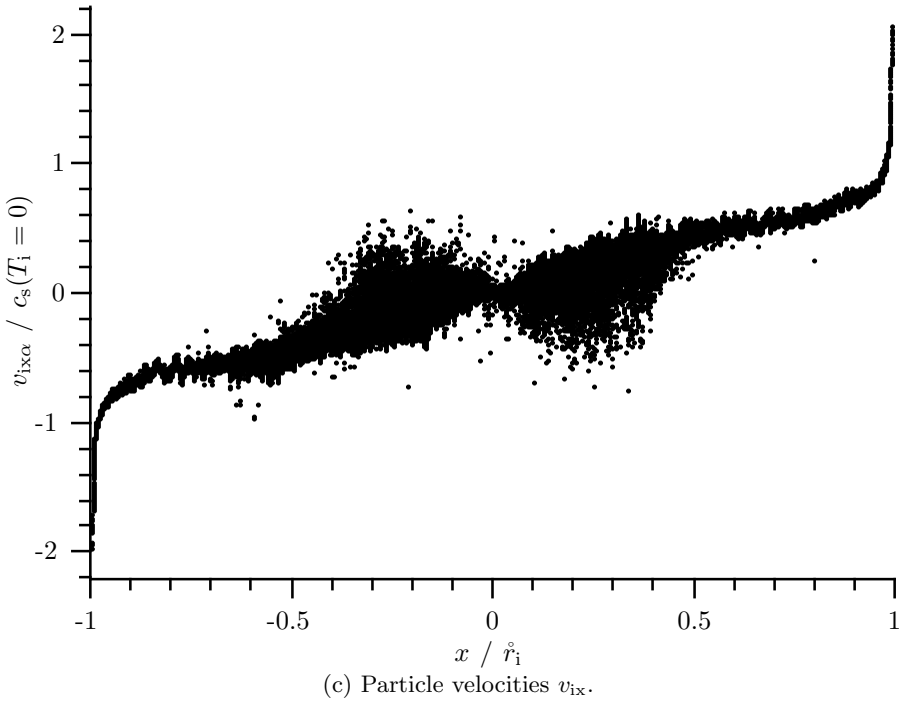

(c) Particle velocities v_{ix}.

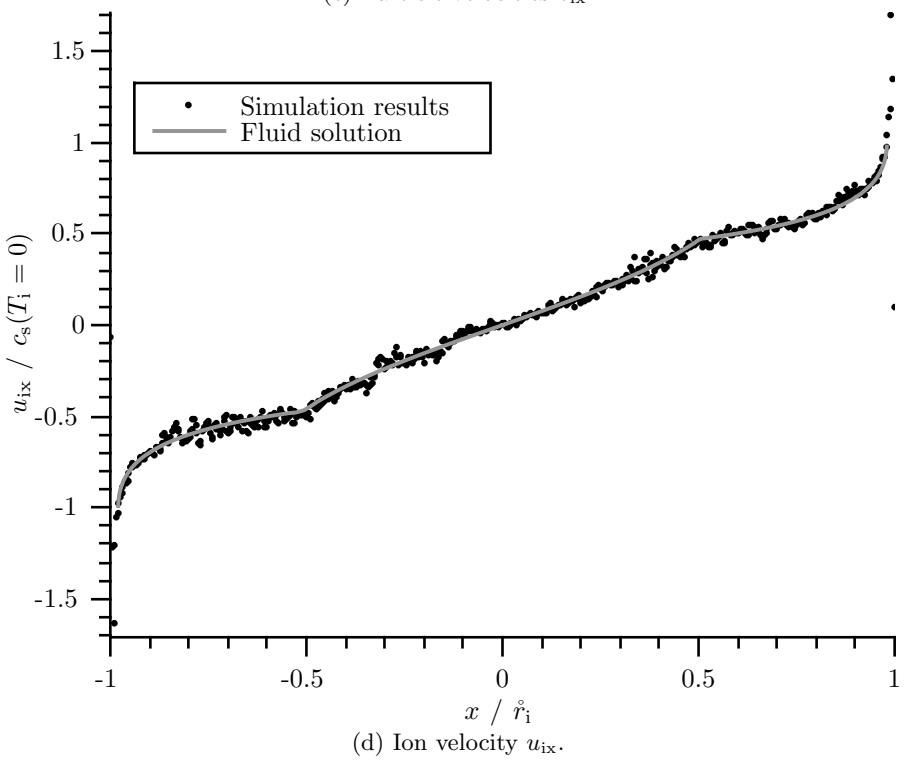

(d) Ion velocity u_{ix}.

Figure 7.16: (continued) Comparison of profiles from numerical integration of fluid equations with hybrid simulation results with $B = 1$, $\alpha = 5°$, $\widehat{\nu}_{\mathrm{ie}} = 1$, $s_{\mathrm{n}} = Af_{\mathrm{cd}}(x)$, $\mathbf{s}_{\mathrm{p}} = s_{\mathrm{n}}\mathbf{u}$. For the fluid solution the following boundary conditions were used $n_0 = 1.22$, $u_{\mathrm{ix0}} = 10^{-6}$, $u_{\mathrm{iy0}} = 0$, $u_{\mathrm{iz0l}} = 0.058$, $(n_{\mathrm{i}}u_{\mathrm{ix}})_{1\mathrm{l}} = -0.4589$, $u_{\mathrm{iz0r}} = -0.12$, $(n_{\mathrm{i}}u_{\mathrm{ix}})_{1\mathrm{r}} = 0.4648$.

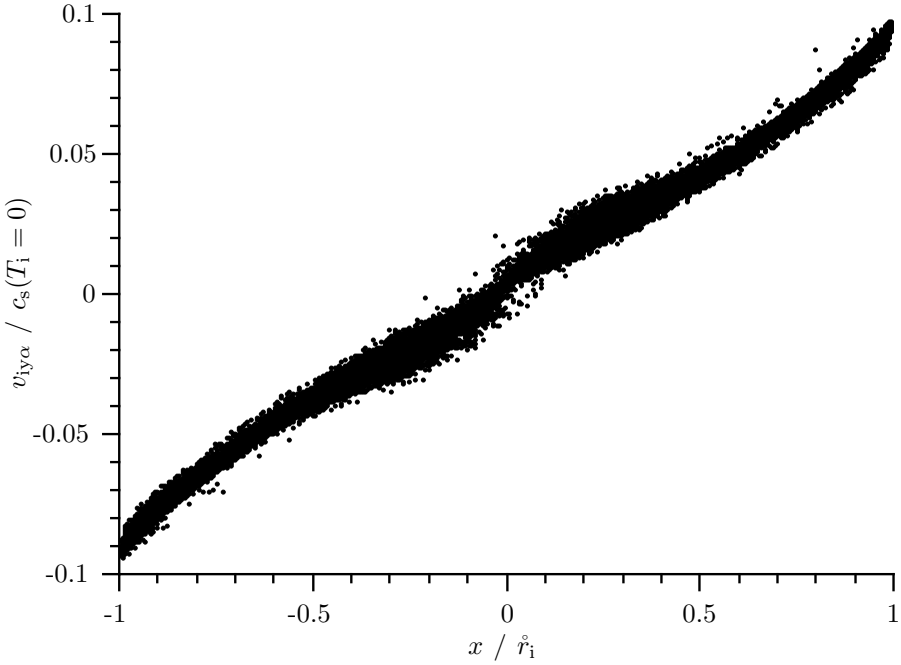

(e) Particle velocities v_{iz}.

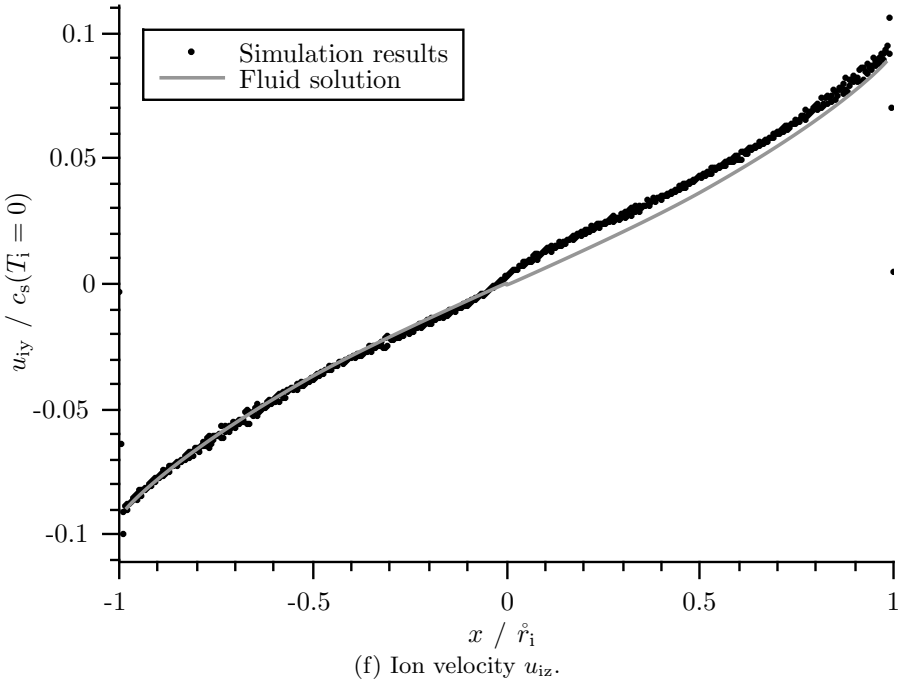

(f) Ion velocity u_{iz}.

Figure 7.16: (continued) Comparison of profiles from numerical integration of fluid equations with hybrid simulation results with $B = 1$, $\alpha = 5°$, $\widehat{\nu}_{\mathrm{ie}} = 1$, $s_{\mathrm{n}} = Af_{\mathrm{cd}}(x)$, $\mathbf{s}_{\mathrm{p}} = s_{\mathrm{n}}\mathbf{u}$. For the fluid solution the following boundary conditions were used $n_0 = 1.22$, $u_{\mathrm{ix0}} = 10^{-6}$, $u_{\mathrm{iy0}} = 0$, $u_{\mathrm{iz0l}} = 0.058$, $(n_{\mathrm{i}}u_{\mathrm{ix}})_{1\mathrm{l}} = -0.4589$, $u_{\mathrm{iz0r}} = -0.12$, $(n_{\mathrm{i}}u_{\mathrm{ix}})_{1\mathrm{r}} = 0.4648$.

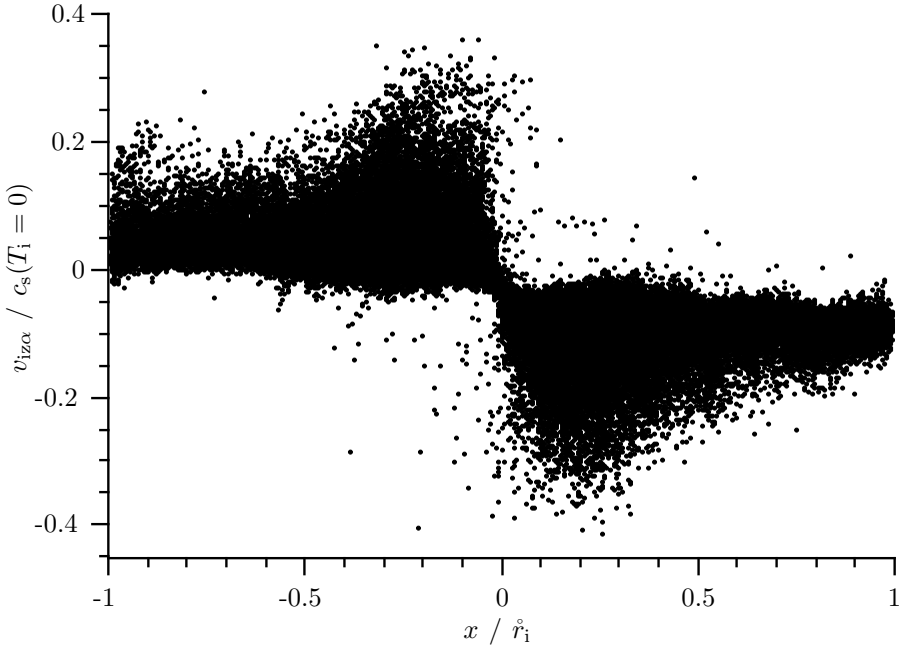

(g) Particle velocities v_{iz}.

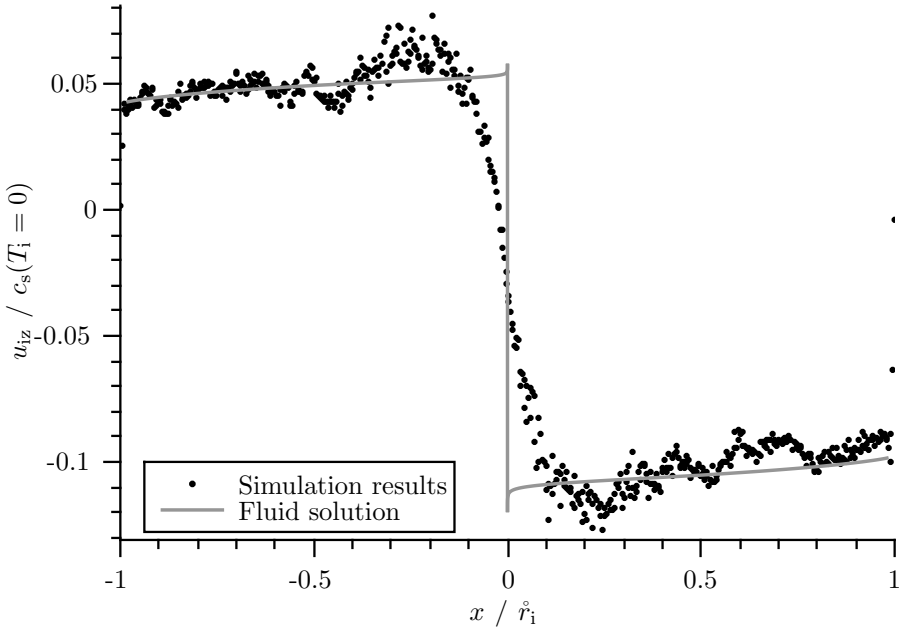

(h) Ion velocity u_{iz}.

Figure 7.16: (continued) Comparison of profiles from numerical integration of fluid equations with hybrid simulation results with $B = 1$, $\alpha = 5°$, $\widehat{\nu}_{\mathrm{ie}} = 1$, $s_{\mathrm{n}} = Af_{\mathrm{cd}}(x)$, $\mathbf{s}_{\mathrm{p}} = s_{\mathrm{n}}\mathbf{u}$. For the fluid solution the following boundary conditions were used $n_0 = 1.22$, $u_{\mathrm{ix0}} = 10^{-6}$, $u_{\mathrm{iy0}} = 0$, $u_{\mathrm{iz0l}} = 0.058$, $(n_{\mathrm{i}}u_{\mathrm{ix}})_{1\mathrm{l}} = -0.4589$, $u_{\mathrm{iz0r}} = -0.12$, $(n_{\mathrm{i}}u_{\mathrm{ix}})_{1\mathrm{r}} = 0.4648$.

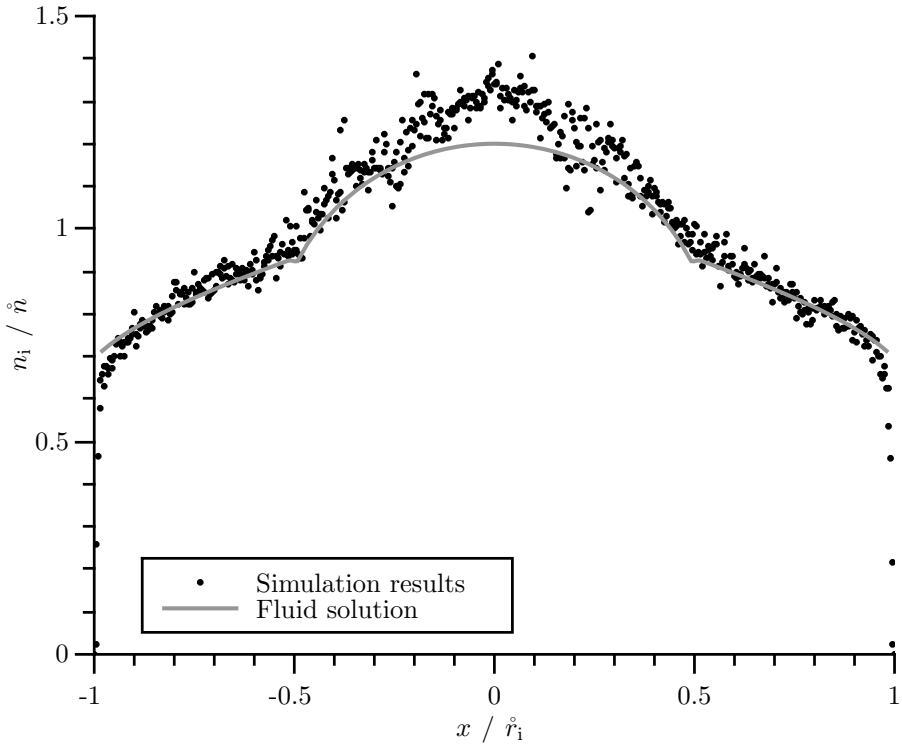

(a) Ion density n_i.

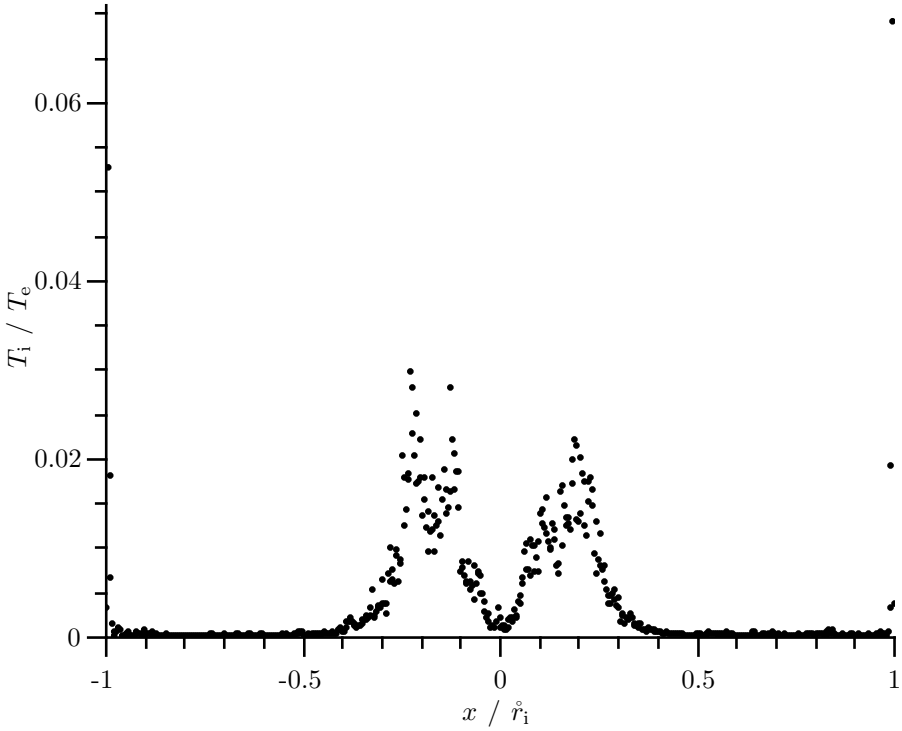

(b) Ion temperature T_i normalized on constant electron temperature T_e.

Figure 7.17: Comparison of profiles from numerical integration of fluid equations with hybrid simulation results with $B = 1,\ \alpha = 45°,\ \widehat{\nu}_\mathrm{ie} = 1,\ s_\mathrm{n} = Af_\mathrm{cd}(x),\ \mathbf{s}_\mathrm{p} = s_\mathrm{n}\mathbf{u}$. For the fluid solution the following boundary conditions were used $n_0 = 1.24,\ u_\mathrm{ix0} = 10^{-6},\ u_\mathrm{iy0} = 0,\ u_\mathrm{iz0} = 0,\ (n_\mathrm{i}u_\mathrm{ix})_1 = 0.6269$.

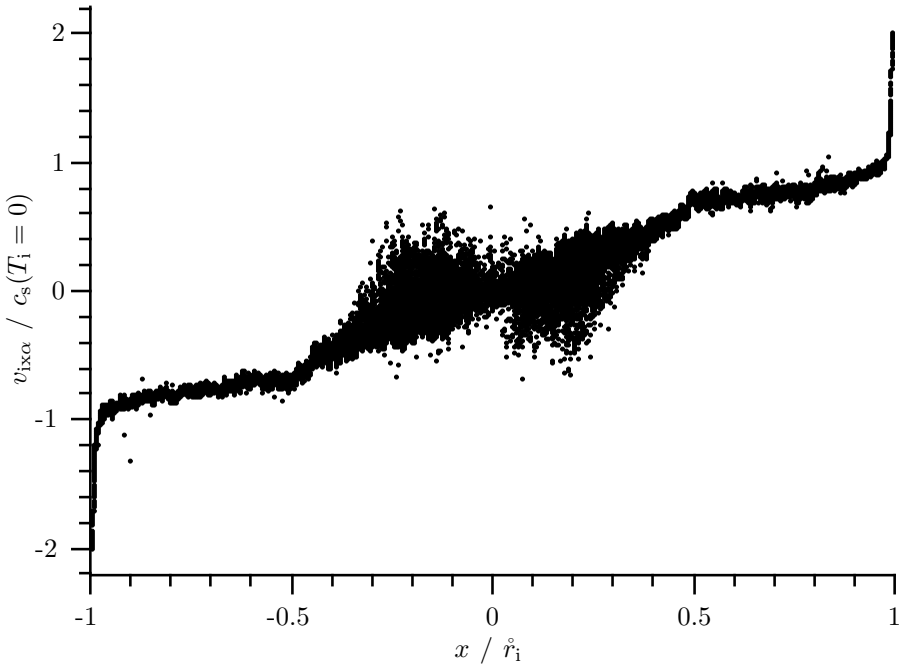

(c) Particle velocities v_{ix}.

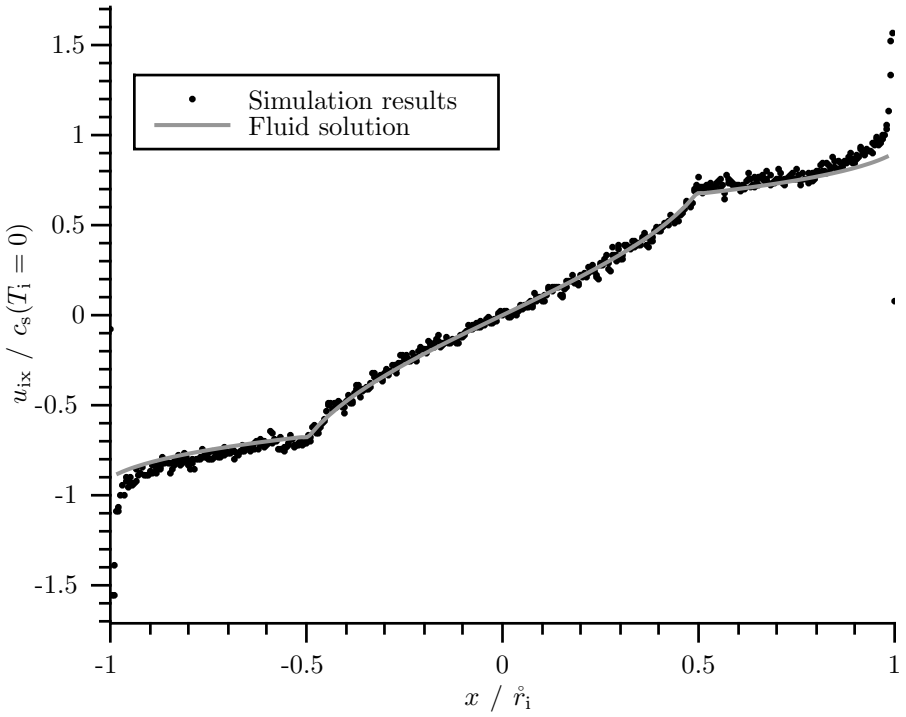

(d) Ion velocity u_{ix}.

Figure 7.17: (continued) Comparison of profiles from numerical integration of fluid equations with hybrid simulation results with $B = 1$, $\alpha = 45°$, $\widehat{\nu}_{\mathrm{ie}} = 1$, $s_{\mathrm{n}} = Af_{\mathrm{cd}}(x)$, $\mathbf{s}_{\mathrm{p}} = s_{\mathrm{n}}\mathbf{u}$. For the fluid solution the following boundary conditions were used $n_0 = 1.24$, $u_{\mathrm{ix0}} = 10^{-6}$, $u_{\mathrm{iy0}} = 0$, $u_{\mathrm{iz0}} = 0$, $(n_{\mathrm{i}}u_{\mathrm{ix}})_1 = 0.6269$.

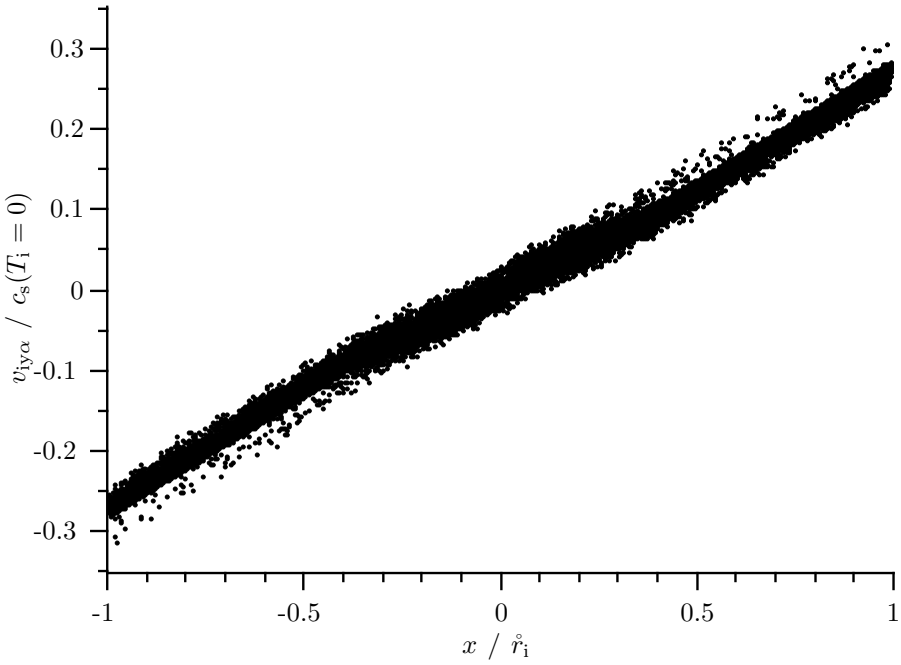

(e) Particle velocities v_{iz}.

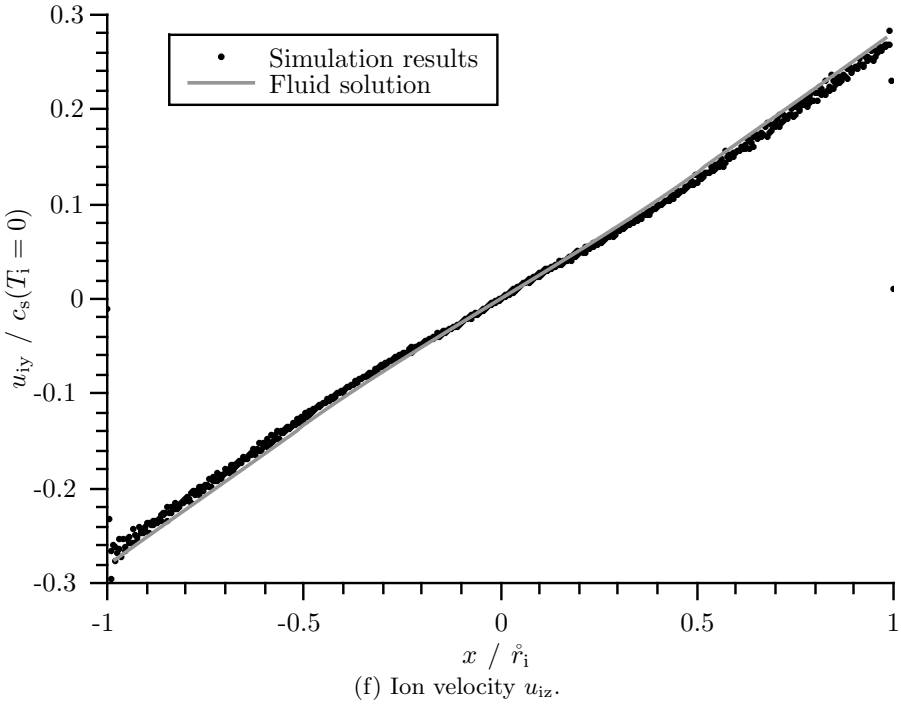

(f) Ion velocity u_{iz}.

Figure 7.17: (continued) Comparison of profiles from numerical integration of fluid equations with hybrid simulation results with $B = 1$, $\alpha = 45°$, $\widehat{\nu}_{\mathrm{ie}} = 1$, $s_{\mathrm{n}} = Af_{\mathrm{cd}}(x)$, $\mathbf{s}_{\mathrm{p}} = s_{\mathrm{n}}\mathbf{u}$. For the fluid solution the following boundary conditions were used $n_0 = 1.24$, $u_{\mathrm{ix0}} = 10^{-6}$, $u_{\mathrm{iy0}} = 0$, $u_{\mathrm{iz0}} = 0$, $(n_{\mathrm{i}}u_{\mathrm{ix}})_1 = 0.6269$.

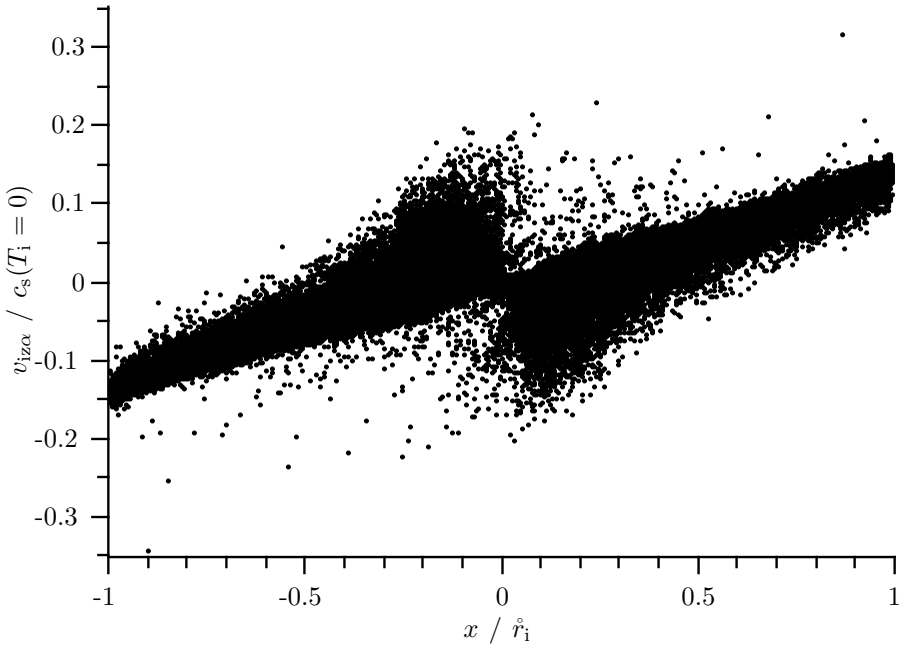

(g) Particle velocities v_{iz}.

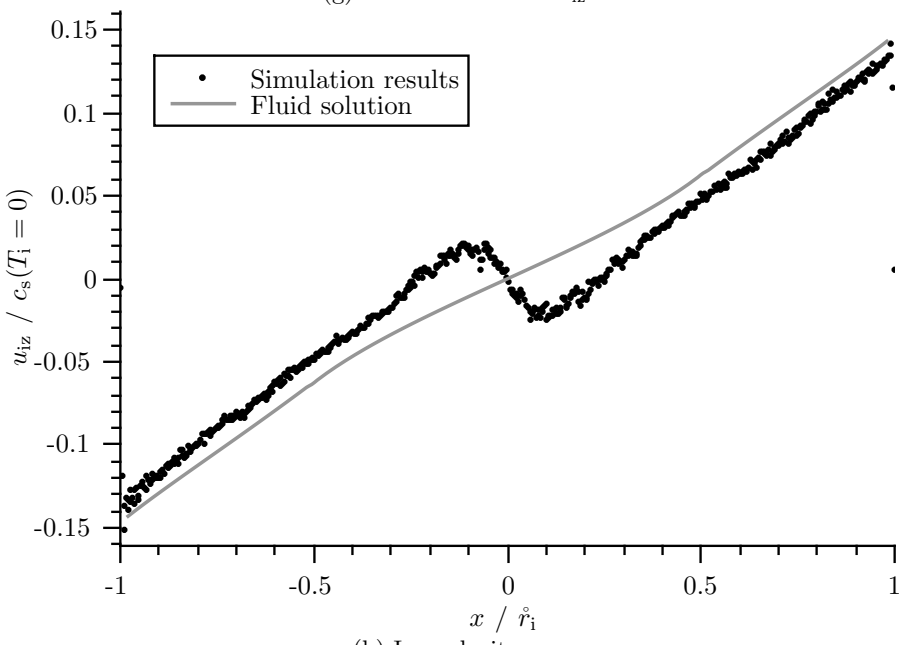

(h) Ion velocity u_{iz}.

Figure 7.17: (continued) Comparison of profiles from numerical integration of fluid equations with hybrid simulation results with $B = 1$, $\alpha = 45°$, $\widehat{\nu}_{\mathrm{ie}} = 1$, $s_{\mathrm{n}} = Af_{\mathrm{cd}}(x)$, $\mathbf{s}_{\mathrm{p}} = s_{\mathrm{n}}\mathbf{u}$. For the fluid solution the following boundary conditions were used $n_0 = 1.24$, $u_{\mathrm{ix0}} = 10^{-6}$, $u_{\mathrm{iy0}} = 0$, $u_{\mathrm{iz0}} = 0$, $(n_{\mathrm{i}}u_{\mathrm{ix}})_1 = 0.6269$.

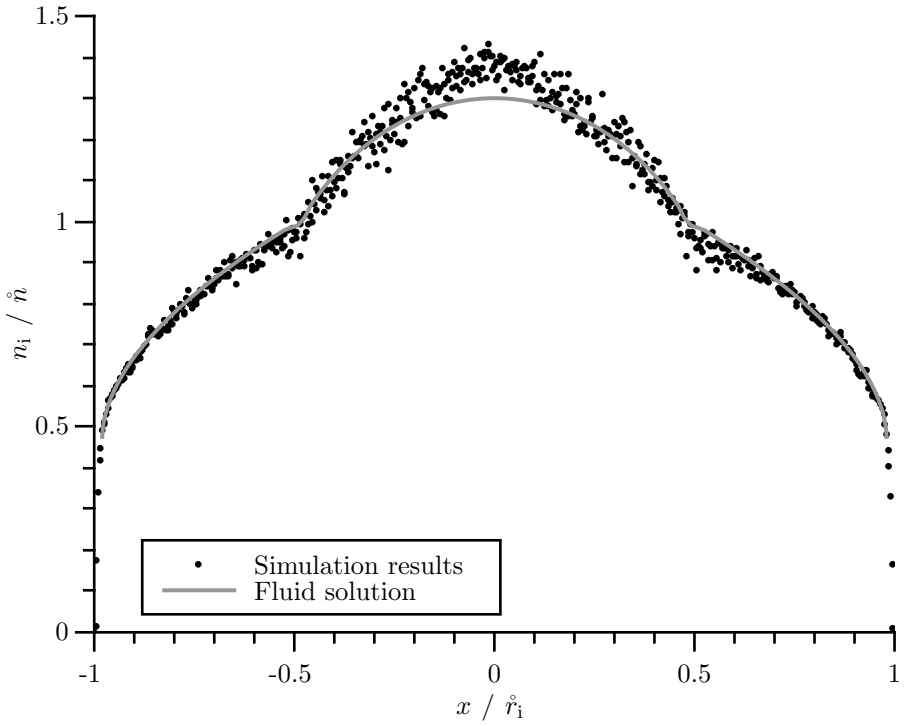

(a) Ion density n_i.

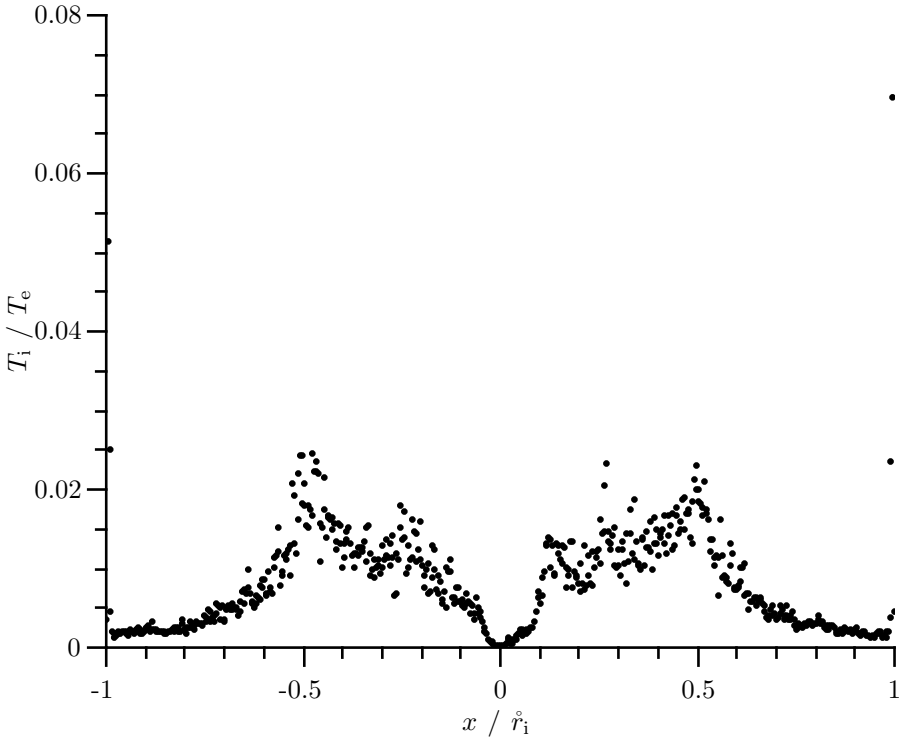

(b) Ion temperature T_i normalized on constant electron temperature T_e.

Figure 7.18: Comparison of profiles from numerical integration of fluid equations with hybrid simulation results with $B = 1,\ \alpha = 5°,\ \widehat{\nu}_\mathrm{ie} = 1,\ s_\mathrm{n} = Af_\mathrm{cd}(x),\ \mathbf{s}_\mathrm{p} = 0$. For the fluid solution the following boundary conditions were used $n_0 = 1.3,\ u_\mathrm{ix0} = 10^{-6},\ u_\mathrm{iy0} = 0,\ u_\mathrm{iz0} = 0,\ (n_\mathrm{i}u_\mathrm{ix})_1 = 0.4684$.

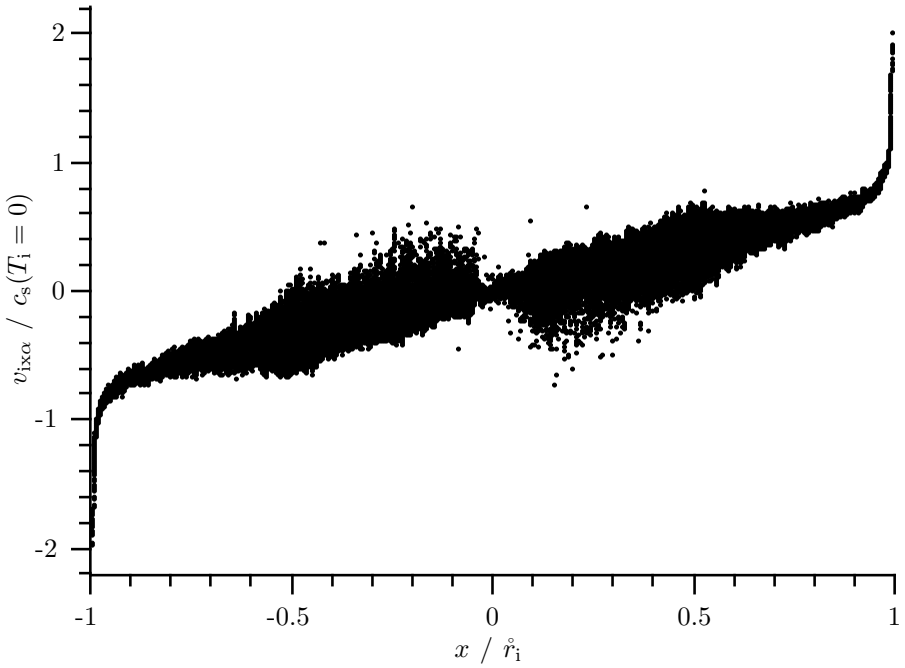

(c) Particle velocities v_{ix}.

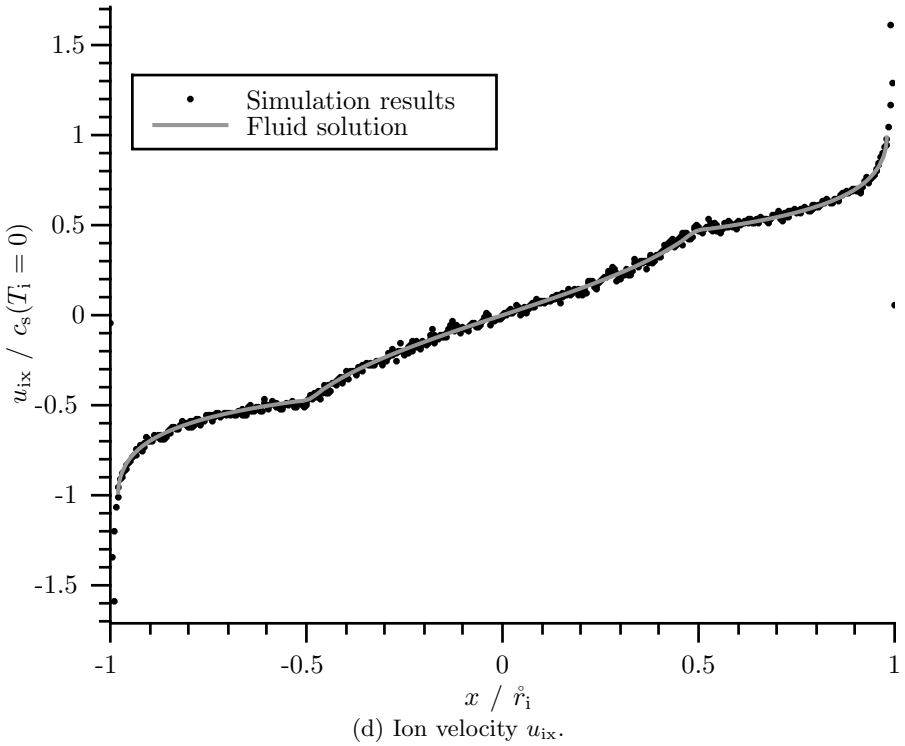

(d) Ion velocity u_{ix}.

Figure 7.18: (continued) Comparison of profiles from numerical integration of fluid equations with hybrid simulation results with $B = 1,\ \alpha = 5°,\ \widehat{\nu}_{\mathrm{ie}} = 1,\ s_{\mathrm{n}} = Af_{\mathrm{cd}}(x),\ \mathbf{s}_{\mathrm{p}} = 0$. For the fluid solution the following boundary conditions were used $n_0 = 1.3,\ u_{\mathrm{ix0}} = 10^{-6},\ u_{\mathrm{iy0}} = 0,\ u_{\mathrm{iz0}} = 0,\ (n_{\mathrm{i}}u_{\mathrm{ix}})_1 = 0.4684$.

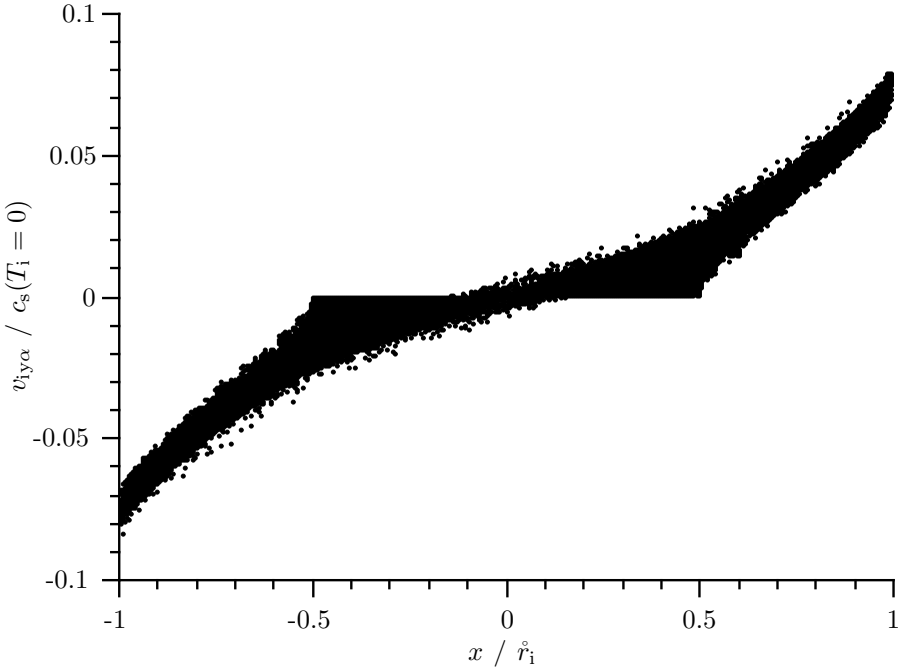

(e) Particle velocities v_{iz}.

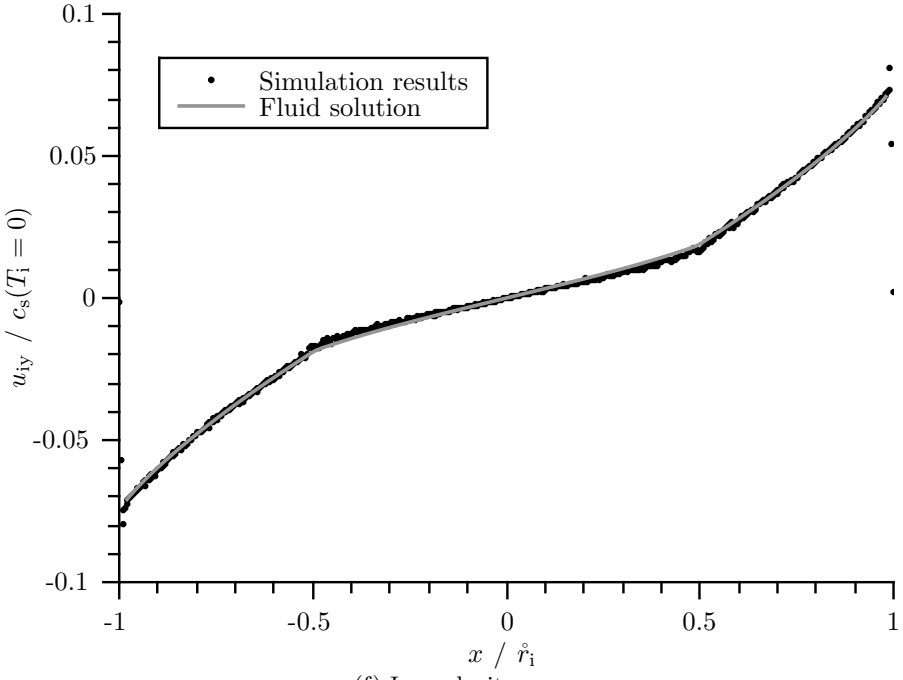

(f) Ion velocity u_{iz}.

Figure 7.18: (continued) Comparison of profiles from numerical integration of fluid equations with hybrid simulation results with $B = 1,\ \alpha = 5°,\ \widehat{\nu}_{\mathrm{ie}} = 1,\ s_{\mathrm{n}} = Af_{\mathrm{cd}}(x),\ \mathbf{s}_{\mathrm{p}} = 0$. For the fluid solution the following boundary conditions were used $n_0 = 1.3,\ u_{\mathrm{ix0}} = 10^{-6},\ u_{\mathrm{iy0}} = 0,\ u_{\mathrm{iz0}} = 0,\ (n_{\mathrm{i}}u_{\mathrm{ix}})_1 = 0.4684$.

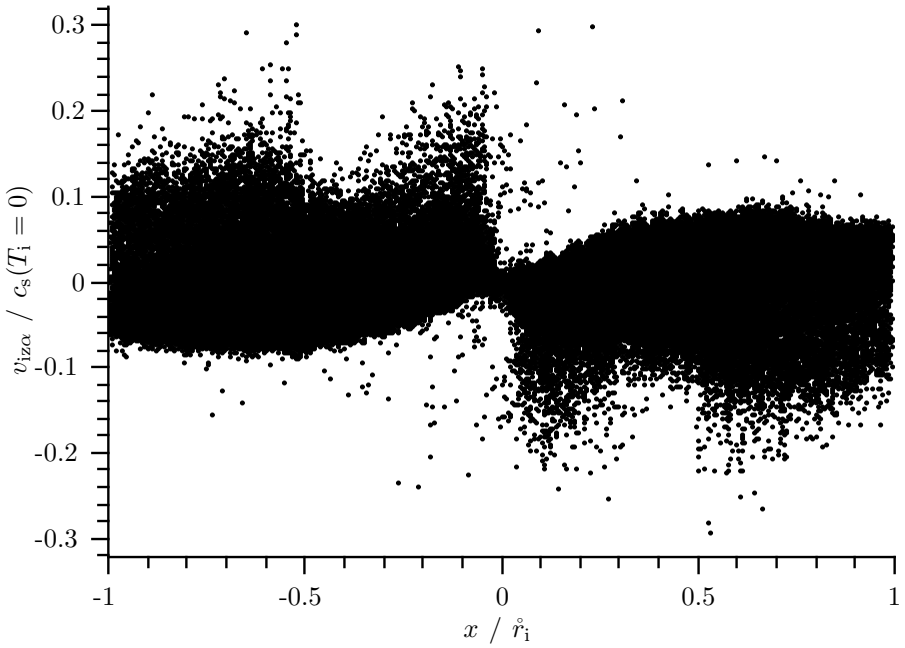

(g) Particle velocities v_{iz}.

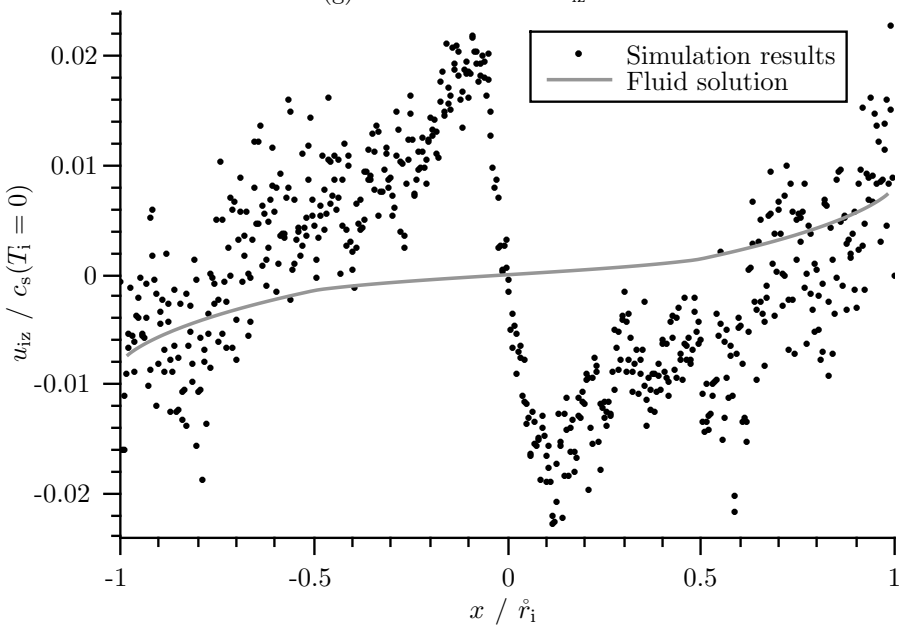

(h) Ion velocity u_{iz}.

Figure 7.18: (continued) Comparison of profiles from numerical integration of fluid equations with hybrid simulation results with $B = 1,\ \alpha = 5°,\ \widehat{\nu}_{ie} = 1,\ s_n = Af_{cd}(x),\ \mathbf{s}_p = 0$. For the fluid solution the following boundary conditions were used $n_0 = 1.3,\ u_{ix0} = 10^{-6},\ u_{iy0} = 0,\ u_{iz0} = 0,\ (n_i u_{ix})_1 = 0.4684$.

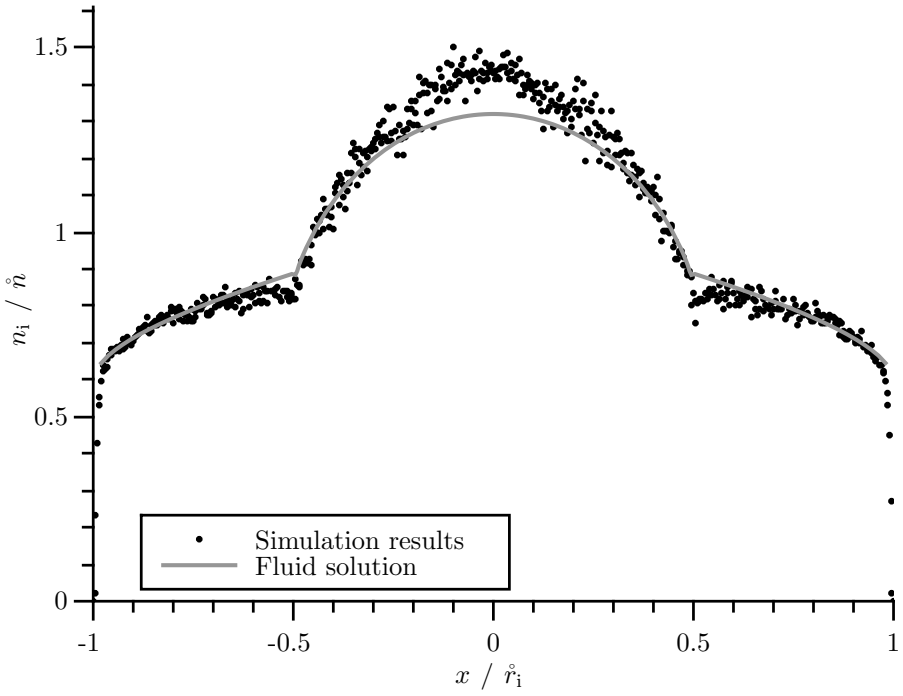

(a) Ion density n_i.

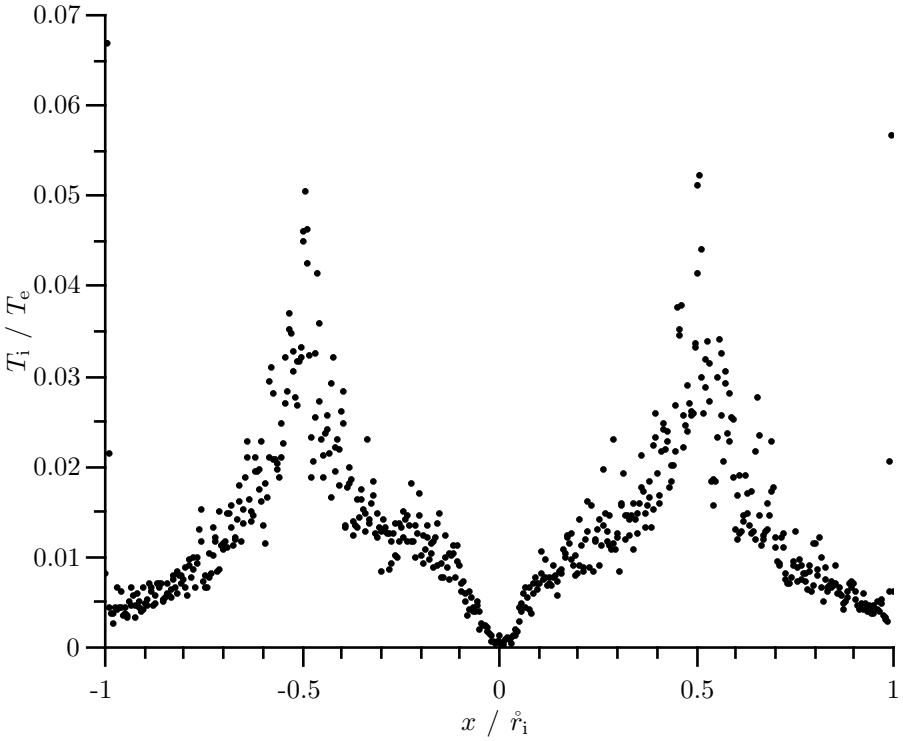

(b) Ion temperature T_i normalized on constant electron temperature T_e.

Figure 7.19: Comparison of profiles from numerical integration of fluid equations with hybrid simulation results with $B = 1,\ \alpha = 45°,\ \widehat{\nu}_\mathrm{ie} = 1,\ s_\mathrm{n} = Af_\mathrm{cd}(x),\ \mathbf{s}_\mathrm{p} = 0$. For the fluid solution the following boundary conditions were used $n_0 = 1.32,\ u_\mathrm{ix0} = 10^{-6},\ u_\mathrm{iy0} = 0,\ u_\mathrm{iz0} = 0,\ (n_\mathrm{i}u_\mathrm{ix})_1 = 0.5967$.

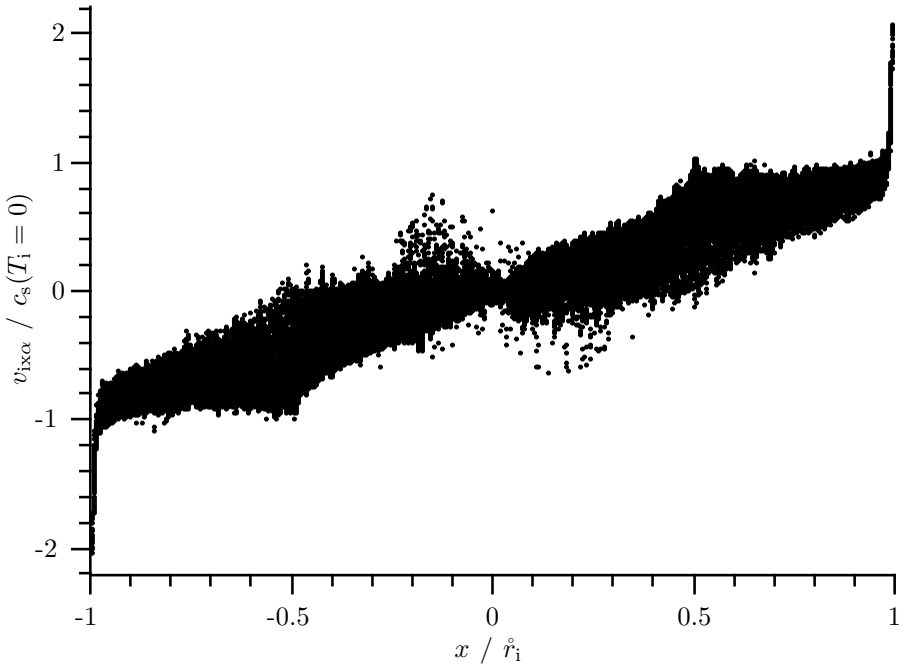

(c) Particle velocities v_{ix}.

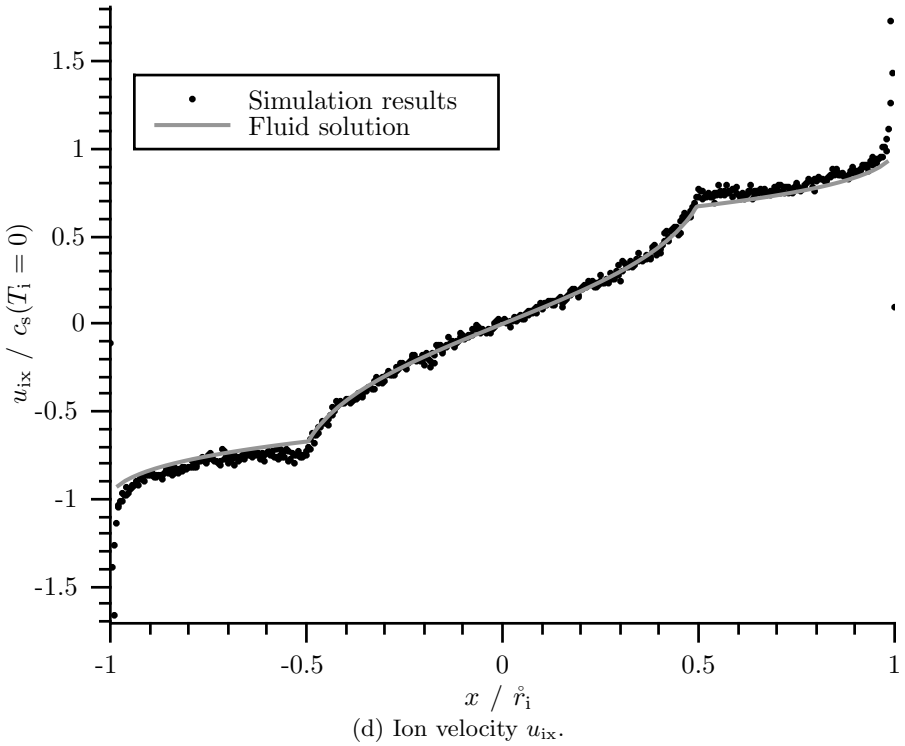

(d) Ion velocity u_{ix}.

Figure 7.19: (continued) Comparison of profiles from numerical integration of fluid equations with hybrid simulation results with $B = 1,\ \alpha = 45°,\ \widehat{\nu}_{ie} = 1,\ s_n = Af_{cd}(x),\ \mathbf{s}_p = 0$. For the fluid solution the following boundary conditions were used $n_0 = 1.32,\ u_{ix0} = 10^{-6},\ u_{iy0} = 0,\ u_{iz0} = 0,\ (n_i u_{ix})_1 = 0.5967$.

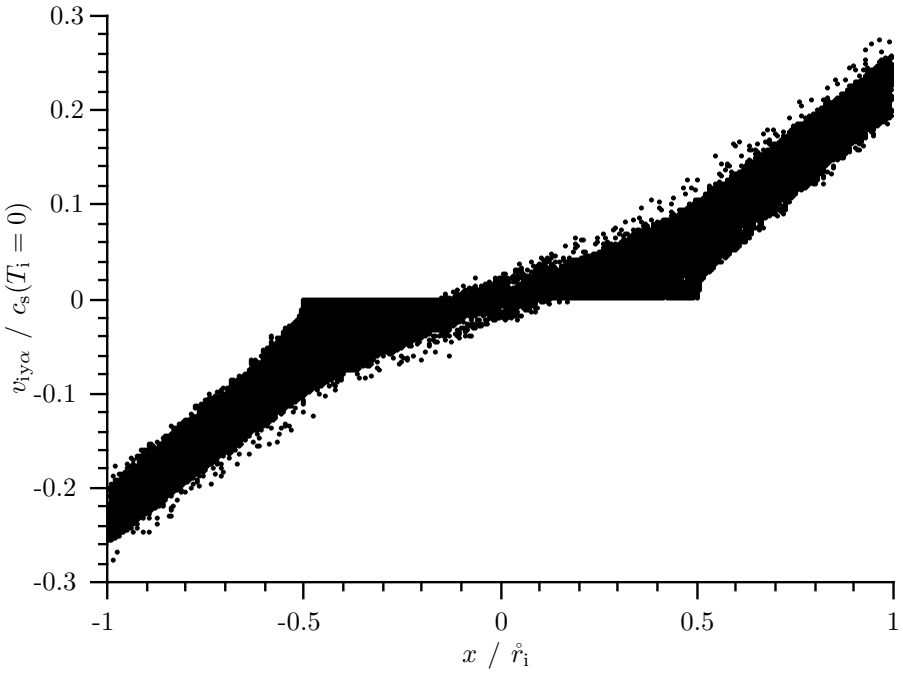

(e) Particle velocities v_{iz}.

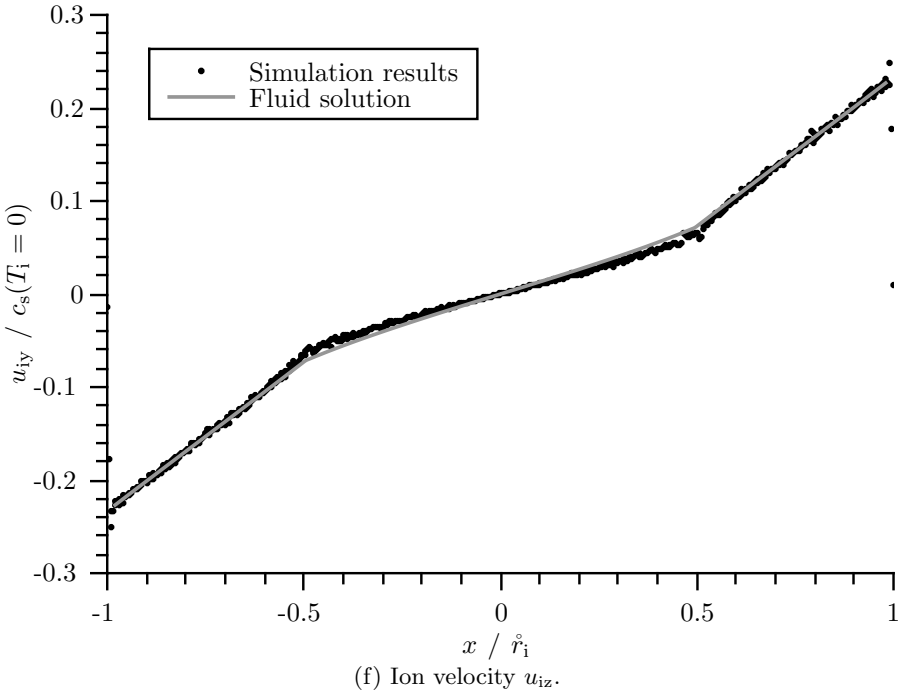

(f) Ion velocity u_{iz}.

Figure 7.19: (continued) Comparison of profiles from numerical integration of fluid equations with hybrid simulation results with $B = 1,\ \alpha = 45°,\ \widehat{\nu}_{\mathrm{ie}} = 1,\ s_{\mathrm{n}} = Af_{\mathrm{cd}}(x),\ \mathbf{s}_{\mathrm{p}} = 0$. For the fluid solution the following boundary conditions were used $n_0 = 1.32,\ u_{\mathrm{ix0}} = 10^{-6},\ u_{\mathrm{iy0}} = 0,\ u_{\mathrm{iz0}} = 0,\ (n_{\mathrm{i}}u_{\mathrm{ix}})_1 = 0.5967$.

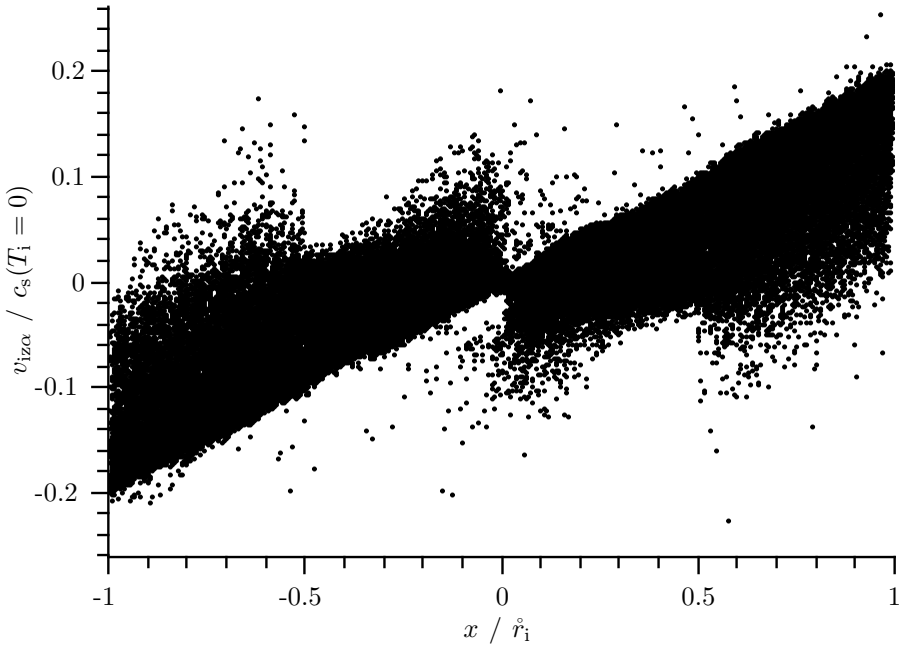

(g) Particle velocities v_{iz}.

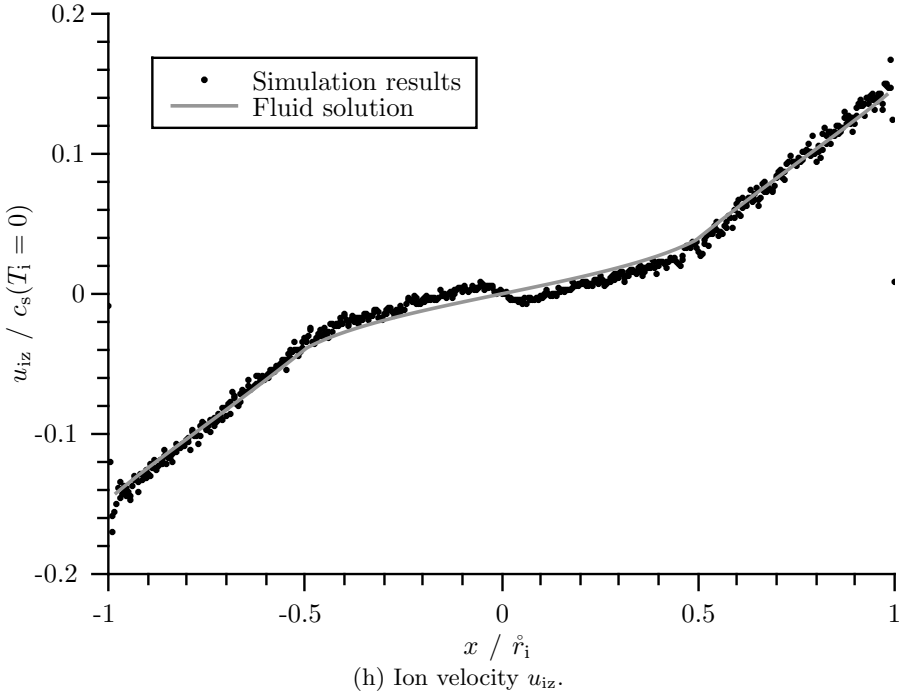

(h) Ion velocity u_{iz}.

Figure 7.19: (continued) Comparison of profiles from numerical integration of fluid equations with hybrid simulation results with $B = 1,\ \alpha = 45°,\ \widehat{\nu}_{\mathrm{ie}} = 1,\ s_{\mathrm{n}} = Af_{\mathrm{cd}}(x),\ \mathbf{s}_{\mathrm{p}} = 0$. For the fluid solution the following boundary conditions were used $n_0 = 1.32,\ u_{\mathrm{ix0}} = 10^{-6},\ u_{\mathrm{iy0}} = 0,\ u_{\mathrm{iz0}} = 0,\ (n_{\mathrm{i}}u_{\mathrm{ix}})_1 = 0.5967$.

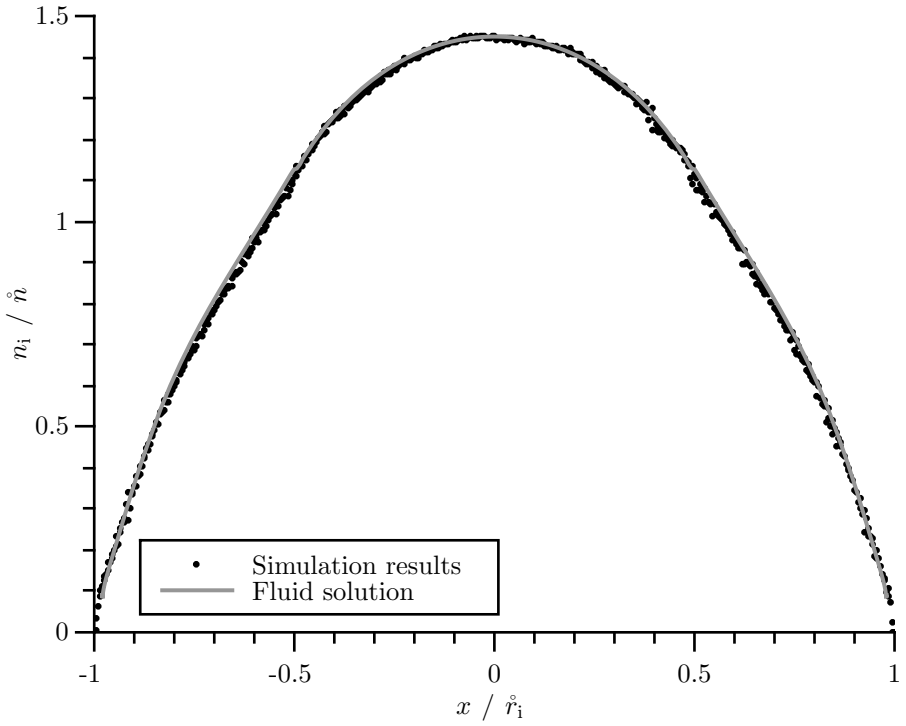

(a) Ion density n_i.

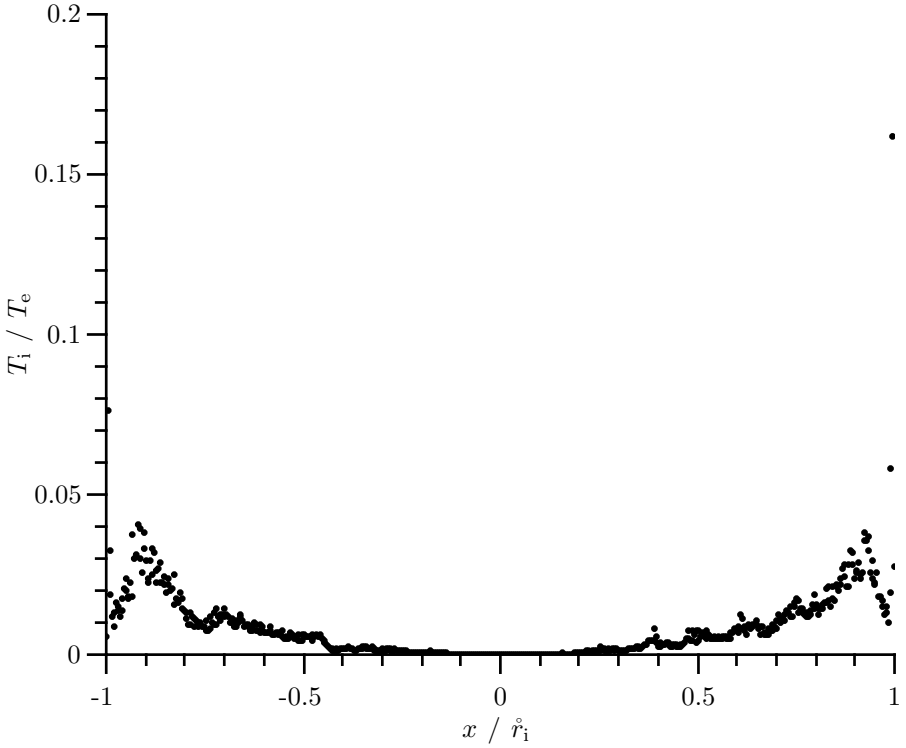

(b) Ion temperature T_i normalized on constant electron temperature T_e.

Figure 7.20: Comparison of profiles from numerical integration of fluid equations with hybrid simulation results with $B = 10,\ \alpha = 5°,\ \widehat{\nu}_\mathrm{ie} = 1,\ s_\mathrm{n} = Af_\mathrm{cd}(x),\ \mathbf{s}_\mathrm{p} = s_\mathrm{n}\mathbf{u}$. For the fluid solution the following boundary conditions were used $n_0 = 1.45,\ u_\mathrm{ix0} = 10^{-6},\ u_\mathrm{iy0} = 0,\ u_\mathrm{iz0} = 0,\ (n_\mathrm{i}u_\mathrm{ix})_1 = 0.08468$.

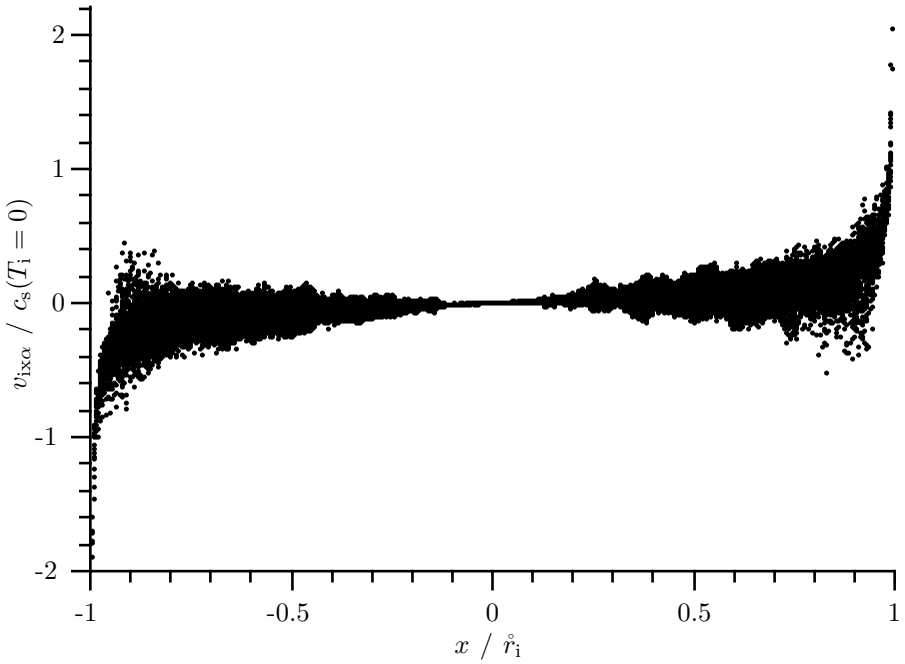

(c) Particle velocities v_{ix}.

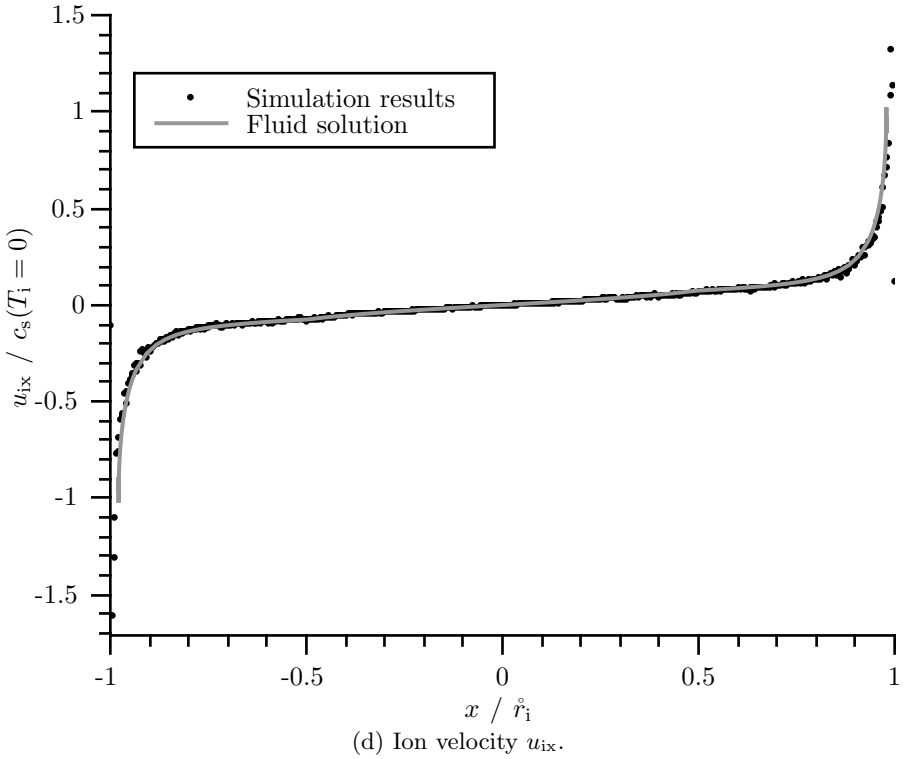

(d) Ion velocity u_{ix}.

Figure 7.20: (continued) Comparison of profiles from numerical integration of fluid equations with hybrid simulation results with $B = 10$, $\alpha = 5°$, $\widehat{\nu}_{\mathrm{ie}} = 1$, $s_{\mathrm{n}} = Af_{\mathrm{cd}}(x)$, $\mathbf{s}_{\mathrm{p}} = s_{\mathrm{n}}\mathbf{u}$. For the fluid solution the following boundary conditions were used $n_0 = 1.45$, $u_{\mathrm{ix0}} = 10^{-6}$, $u_{\mathrm{iy0}} = 0$, $u_{\mathrm{iz0}} = 0$, $(n_{\mathrm{i}}u_{\mathrm{ix}})_1 = 0.08468$.

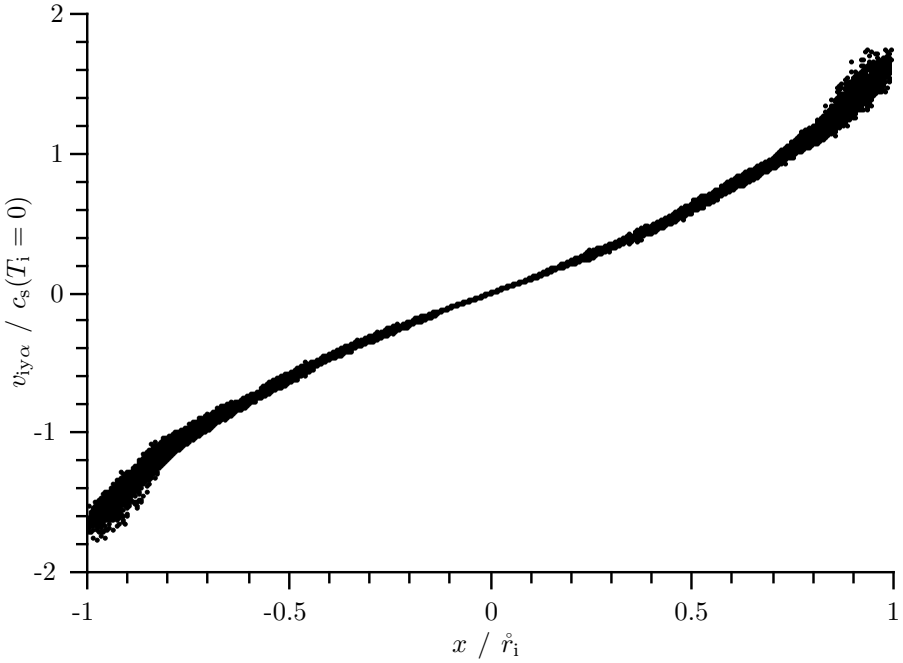

(e) Particle velocities v_{iz}.

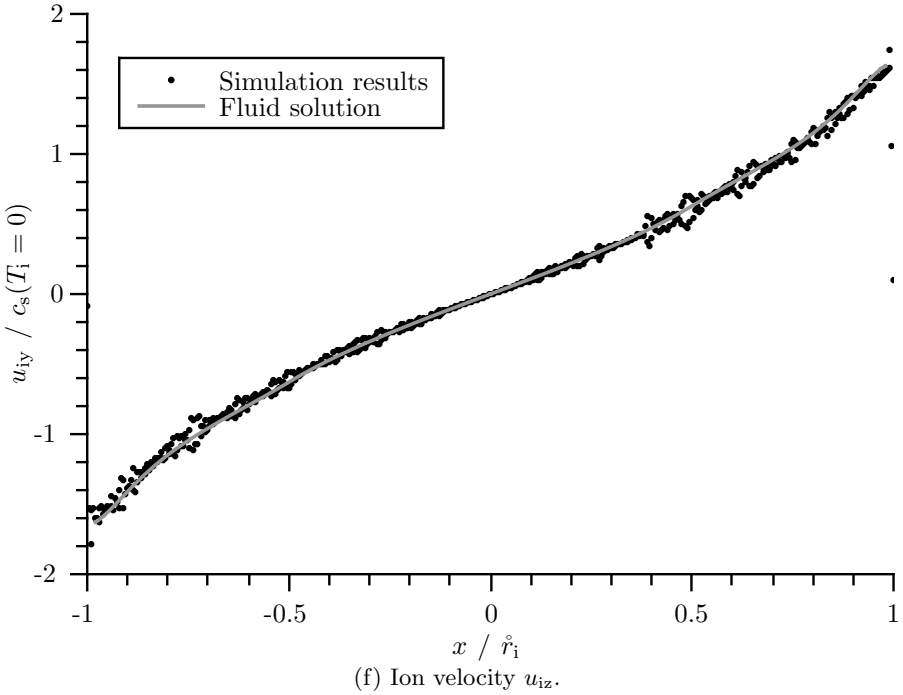

(f) Ion velocity u_{iz}.

Figure 7.20: (continued) Comparison of profiles from numerical integration of fluid equations with hybrid simulation results with $B = 10$, $\alpha = 5°$, $\widehat{\nu}_{\mathrm{ie}} = 1$, $s_{\mathrm{n}} = Af_{\mathrm{cd}}(x)$, $\mathbf{s}_{\mathrm{p}} = s_{\mathrm{n}}\mathbf{u}$. For the fluid solution the following boundary conditions were used $n_0 = 1.45$, $u_{\mathrm{ix0}} = 10^{-6}$, $u_{\mathrm{iy0}} = 0$, $u_{\mathrm{iz0}} = 0$, $(n_{\mathrm{i}}u_{\mathrm{ix}})_1 = 0.08468$.

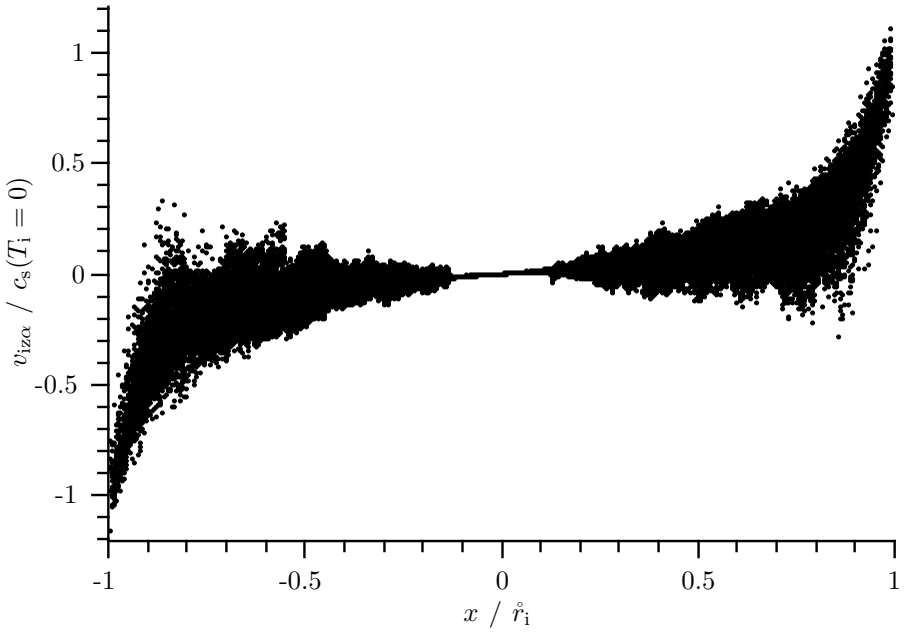

(g) Particle velocities v_{iz}.

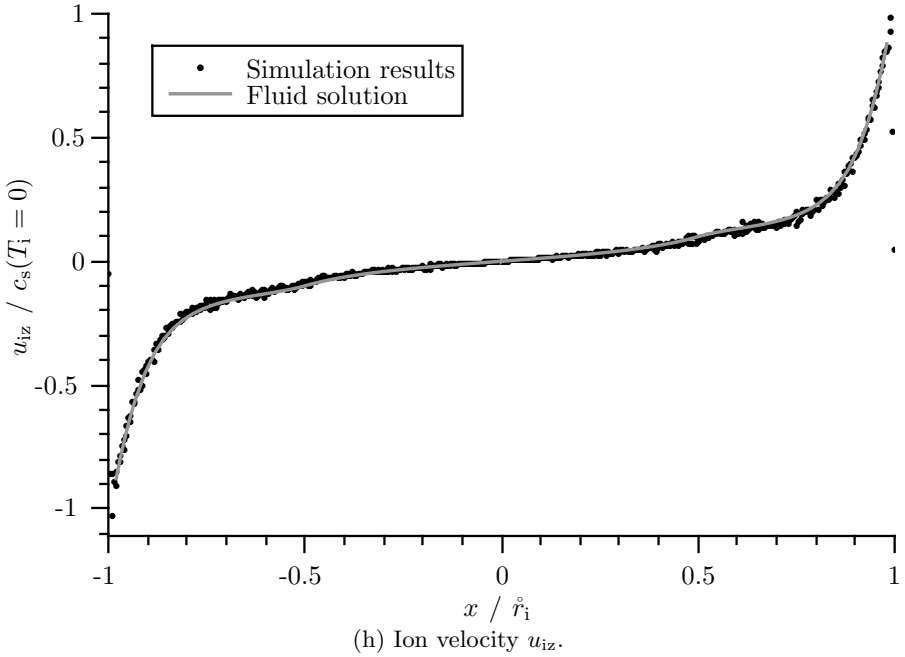

(h) Ion velocity u_{iz}.

Figure 7.20: (continued) Comparison of profiles from numerical integration of fluid equations with hybrid simulation results with $B = 10$, $\alpha = 5°$, $\widehat{\nu}_{ie} = 1$, $s_n = Af_{cd}(x)$, $\mathbf{s}_p = s_n\mathbf{u}$. For the fluid solution the following boundary conditions were used $n_0 = 1.45$, $u_{ix0} = 10^{-6}$, $u_{iy0} = 0$, $u_{iz0} = 0$, $(n_i u_{ix})_1 = 0.08468$.

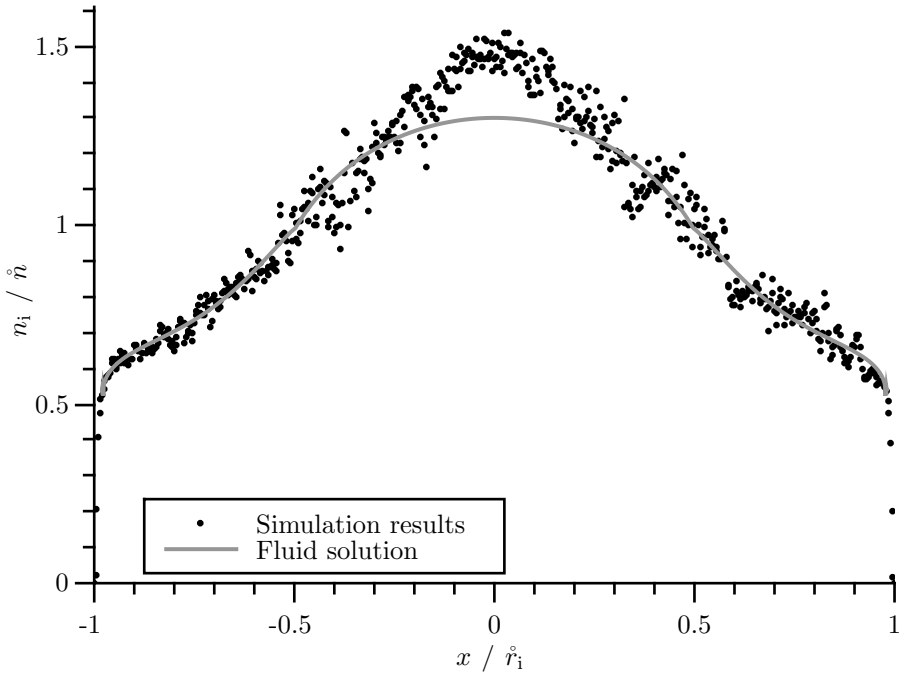

(a) Ion density n_i.

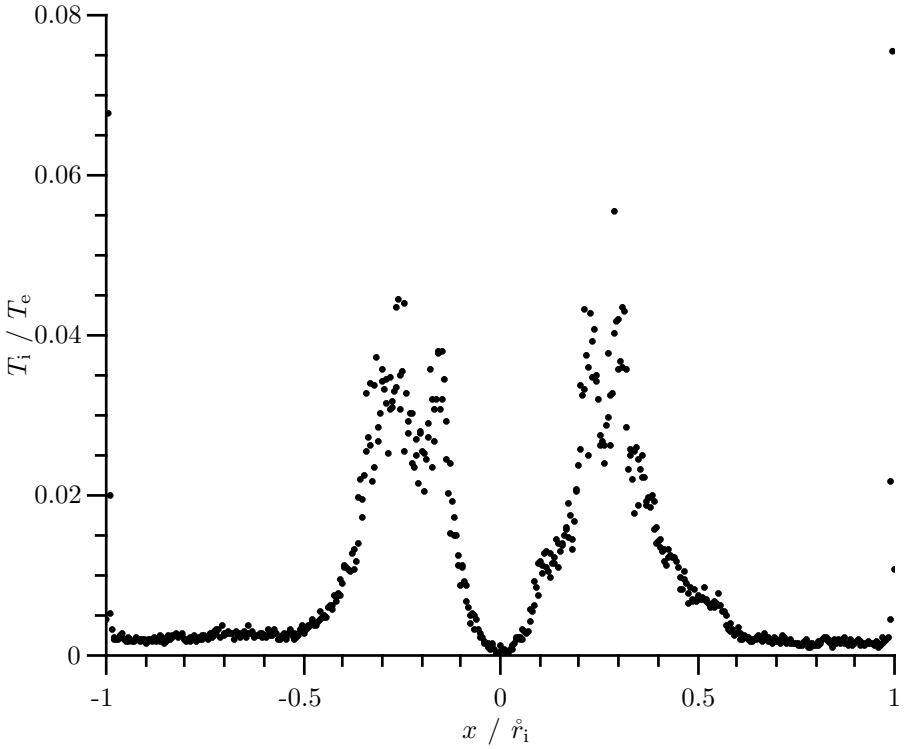

(b) Ion temperature T_i normalized on constant electron temperature T_e.

Figure 7.21: Comparison of profiles from numerical integration of fluid equations with hybrid simulation results with $B = 10,\ \alpha = 45°,\ \widehat{\nu}_\mathrm{ie} = 1,\ s_\mathrm{n} = Af_\mathrm{cd}(x),\ \mathbf{s}_\mathrm{p} = s_\mathrm{n}\mathbf{u}$. For the fluid solution the following boundary conditions were used $n_0 = 1.3,\ u_\mathrm{ix0} = 10^{-6},\ u_\mathrm{iy0} = 0,\ u_\mathrm{iz0} = 0,\ (n_\mathrm{i}u_\mathrm{ix})_1 = 0.5419$.

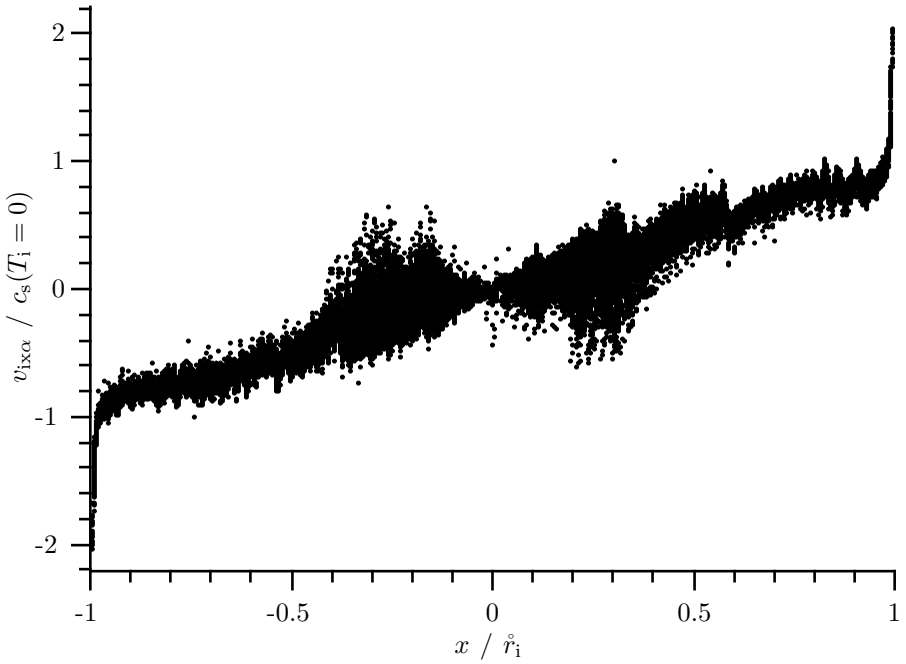

(c) Particle velocities v_{ix}.

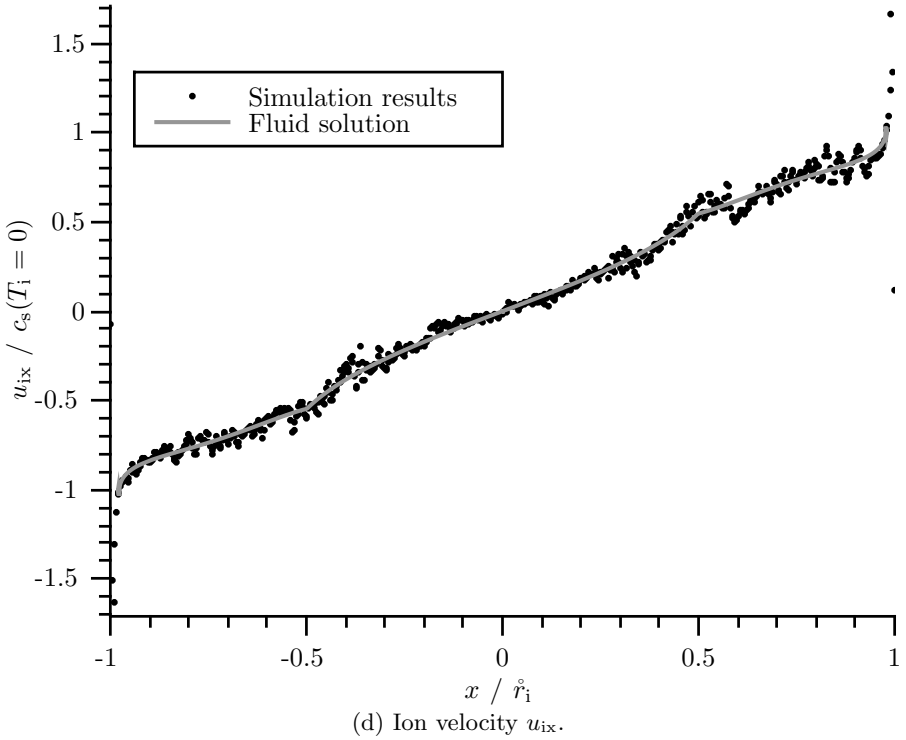

(d) Ion velocity u_{ix}.

Figure 7.21: (continued) Comparison of profiles from numerical integration of fluid equations with hybrid simulation results with $B = 10$, $\alpha = 45°$, $\widehat{\nu}_{\mathrm{ie}} = 1$, $s_{\mathrm{n}} = Af_{\mathrm{cd}}(x)$, $\mathbf{s}_{\mathrm{p}} = s_{\mathrm{n}}\mathbf{u}$. For the fluid solution the following boundary conditions were used $n_0 = 1.3$, $u_{\mathrm{ix0}} = 10^{-6}$, $u_{\mathrm{iy0}} = 0$, $u_{\mathrm{iz0}} = 0$, $(n_{\mathrm{i}}u_{\mathrm{ix}})_1 = 0.5419$.

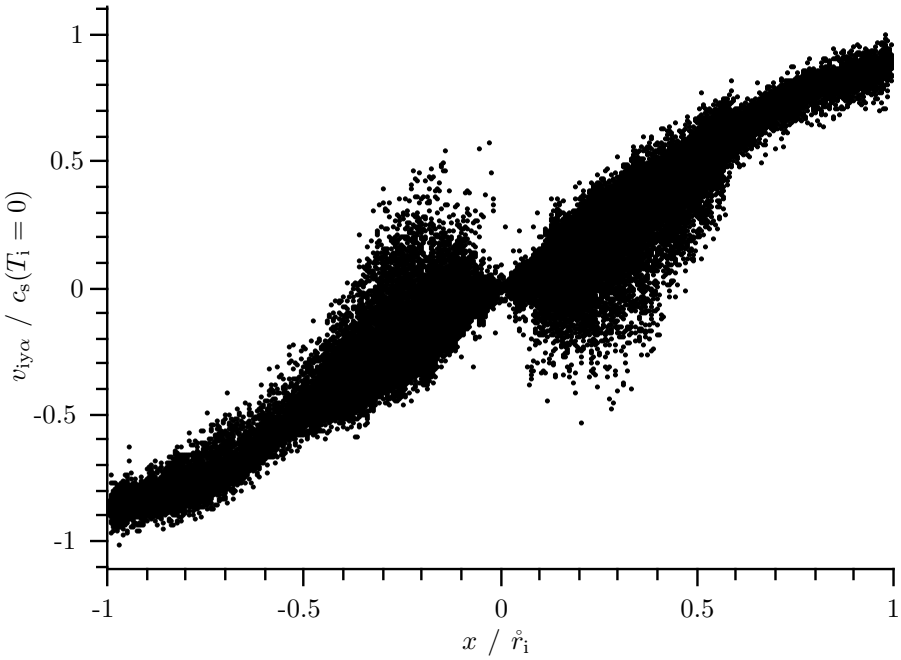

(e) Particle velocities v_{iz}.

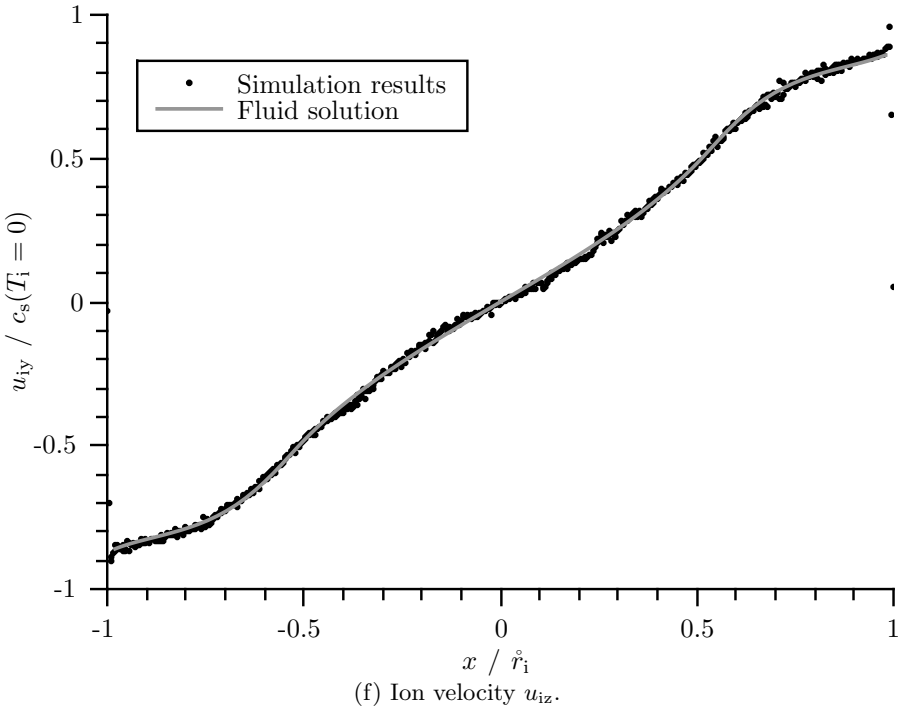

(f) Ion velocity u_{iz}.

Figure 7.21: (continued) Comparison of profiles from numerical integration of fluid equations with hybrid simulation results with $B = 10$, $\alpha = 45°$, $\widehat{\nu}_{\mathrm{ie}} = 1$, $s_{\mathrm{n}} = Af_{\mathrm{cd}}(x)$, $\mathbf{s}_{\mathrm{p}} = s_{\mathrm{n}}\mathbf{u}$. For the fluid solution the following boundary conditions were used $n_0 = 1.3$, $u_{\mathrm{ix0}} = 10^{-6}$, $u_{\mathrm{iy0}} = 0$, $u_{\mathrm{iz0}} = 0$, $(n_{\mathrm{i}}u_{\mathrm{ix}})_1 = 0.5419$.

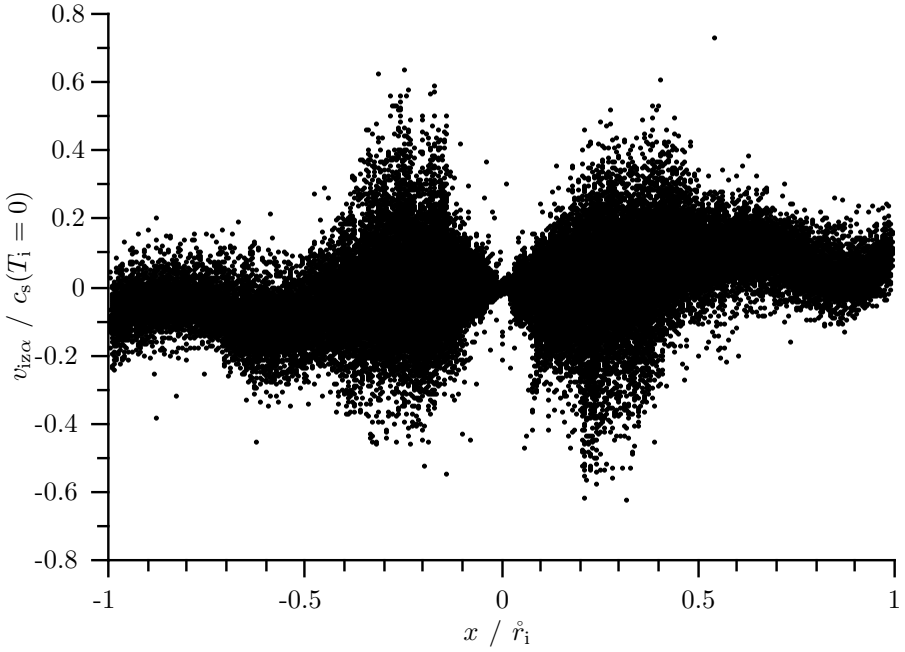

(g) Particle velocities v_{iz}.

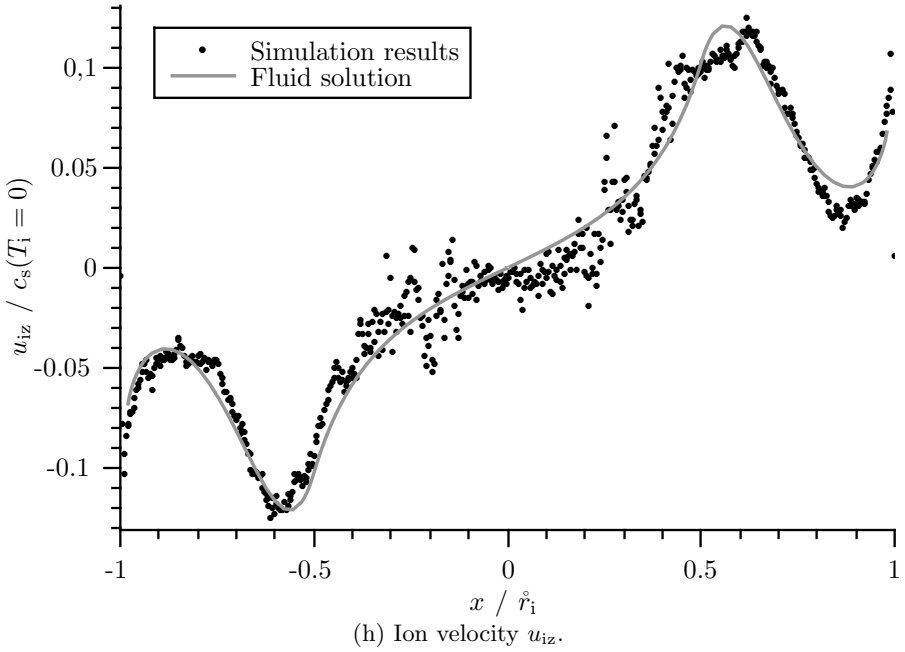

(h) Ion velocity u_{iz}.

Figure 7.21: (continued) Comparison of profiles from numerical integration of fluid equations with hybrid simulation results with $B = 10$, $\alpha = 45°$, $\widehat{\nu}_{\mathrm{ie}} = 1$, $s_{\mathrm{n}} = Af_{\mathrm{cd}}(x)$, $\mathbf{s}_{\mathrm{p}} = s_{\mathrm{n}}\mathbf{u}$. For the fluid solution the following boundary conditions were used $n_0 = 1.3$, $u_{\mathrm{ix0}} = 10^{-6}$, $u_{\mathrm{iy0}} = 0$, $u_{\mathrm{iz0}} = 0$, $(n_{\mathrm{i}}u_{\mathrm{ix}})_1 = 0.5419$.

Chapter 8

Summary and outlook

Regarding plasma–wall–interactions, a new type of interpretation in terms of jump conditions has been delivered, which provides an alternative to the Bohm theory. Interestingly both explanations lead to the same result of ions passing the sheath border with their sound velocity c_s, though the approach with jump conditions provides a more natural access to the problem and requires less assumptions in derivation.

To further investigate the new findings in simulation, a simple one–dimensional model of a plasma discharge, surrounded by totally absorbing walls, was introduced. It has been enhanced by an ionization source such that the system is able to reach a stationary state.

Simulations have been performed with many different configurations of magnetic fields and ionization source densities. Differences between numerical solutions of the fluid equations and hybrid simulation results are observable in many cases. Kinetic effects such as ion gyro motion and heating of ions, especially caused by ionization, as well as anisotropic effects need to be considered to properly represent plasmas as presented in the model, particularly in the domain center for weakly magnetized plasmas and when considering a neutral gas background. For strongly magnetized plasmas, the simulation results for the z–component of the average ion velocity u_iz get noisy for a magnetic field parallel to the walls and for large impact angles α of the magnetic field, whereas they appear smooth for small impact angles α.

Since this thesis provides elementary investigations and results, they are ready to be applied on different problem statements in simulation, especially on the PSI–2 experiment for which this thesis was originally intended. For this purpose the presented wall model needs to be transferred to three– or rather to two–dimensional simulations under consideration of cylindrical symmetry. In addition its characteristics need to be specified more precisely rather than considering basic plasma processes in general.

A common observation in the mentioned experiment is the rotation of the produced plasma pillar. It may be checked whether this is reproducible in hybrid simulations, and if so, which role kinetic effects are playing. The presented simulation results for the z–component of the ion velocities already hint at this effect. The plasma generator of the JULE–PSI experiment, scheduled as an enhancement of PSI–2, will provide a cathode plate instead of a hallow cathode which can be adopted easily in simulation, so that it will be able to handle the next generation of the experiment.

Acknowledgments

In the end, I would like to thank all members of the institute for theoretical physics I (TP1) for the nice working atmosphere and the provision of accommodations and computational resources to complete this thesis. Furthermore I would like to acknowledge Prof. Dr. Deltef Reiter and Prof. Dr. Bernhard Unterberg from Forschungszentrum Jülich for the proposal of the topic in terms of the PSI–2 experiment. A very special thanks is due to Dr. Jürgen Dreher for his advise and the many hours he sacrificed in the assistance and thus in the realization of this project.

References

[AGB05] B. Alterkop, S. Goldsmith, and R. L. Boxman. Presheath in fully ionized collisional plasma in a magnetic field. *Contributions to Plasma Physics*, 45(7):485–493, October 2005. doi:10.1002/ctpp.200510054.

[ASP10] Eduardo Ahedo, Robert Santos, and Félix I. Parra. Fulfillment of the kinetic Bohm criterion in a quasineutral particle–in–cell model. *Physics of Plasmas*, 17(7):073507, July 2010. doi:10.1063/1.3456516.

[Beh84] Jürgen Behnel. *Kinetische Analyse der Plasmarandschicht bei einem wandparallelen Magnetfeld*. PhD thesis, Ruhr–Universität Bochum, 1984.

[BL85] C. K. Birdsall and A. B. Langdon. *Plasma physics via computer simulation*. McGraw–Hill, New York, 1985. URL: http://www.taylorandfrancis.com/books/details/9780750310253/ [cited 2015-04-12].

[Boh49] David Bohm. Minimum ionic kinetic energy for a stable sheath. In A. Guthrie and R. K. Wakerling, editors, *The characteristics of electrical discharges in magnetic fields*, volume I–5 of *the national nuclear energy series*, chapter 3, pages 77–86. McGraw–Hill book company, inc., 1st edition, 1949.

[Bor70] Jay P. Boris. Relativistic plasma simulation – optimization of a hybrid code. In *Proceedings of the Fourth Conference on the Numerical Simulation of Plasmas*, pages 3–67, Washington, D. C., November 1970. Naval Research Laboratory. URL: http://www.dtic.mil/dtic/tr/fulltext/u2/a023511.pdf [cited 2015-04-12].

[BS03] T. J. M. Boyd and J. J. Sanderson. *The physics of plasmas*. Cambridge university press, 2003. doi:10.1017/CBO9780511755750.

[Cho82] Roland Chodura. Plasma–wall transition in an oblique magnetic field. *Physics of Fluids*, 25(9):1628–1633, September 1982. doi:10.1063/1.863955.

[Cho85] Roland Chodura. Plasma flow in the sheath and the presheath of a scrape–off layer. Technical Report IPP 5/1, Max–Planck–Institut für Plasmaphysik, Garching, February 1985. URL: http://edoc.mpg.de/442096 [cited 2015-04-12].

[Cho88] Roland Chodura. Basic problems in edge plasma modelling. *Contributions to Plasma Physics*, 28(4–5):303–312, 1988. doi:10.1002/ctpp.2150280405.

[FD78] C. M. Ferreira and J. L. Delcroix. Theory of the hollow cathode arc. *Journal of Applied Physics*, 49(4):2380–2395, April 1978. doi:10.1063/1.325126.

[Feh13] Marc Fehling. Entwicklung und Validierung eines dreidimensionalen, parallelen Hybrid Codes zur Simulation von Plasmen. Bachelor's thesis, Ruhr–Universität Bochum, 2013.

[FL] FlareLab. URL: http://flarelab.ruhr-uni-bochum.de/ [cited 2015-04-12].

[HFM93] D. L. Holland, B. D. Fried, and G. J. Morales. Sheath structure in a magnetized plasma. *Physics of Fluids B: Plasma Physics*, 5(6):1723–1737, June 1993. doi:10.1063/1.860806.

[KBL+01] S. Klose, W. Bohmeyer, M. Laux, H. Meyer, G. Fussmann, and the PSI-team. Investigation of ion drift waves in the PSI–2 using Langmuir–probes. *Contributions to Plasma Physics*, 41(5):467–472, September 2001. doi:10.1002/1521-3986(200109)41:5<467::AID-CTPP467>3.0.CO;2-X.

[KL00] Alexander Kurganov and Doron Levy. A third–order semidiscrete central scheme for conservation laws and convection–diffusion equations. *SIAM Journal on Scientific Computing*, 22(4):1461–1488, 2000. doi:10.1137/S1064827599360236.

[Kre11] Arkadi Kreter. PSI–2 — the pilot experiment of the JULE–PSI project, September 2011. URL: http://www.pwi-ia.org/pmif/talks/2011-09-19/PMIF_2011-09-19_Kreter.pptx [cited 2015-04-12].

[Lap] Giovanni Lapenta. Particle in cell methods with application to simulations in space weather. URL: https://perswww.kuleuven.be/~u0052182/pic/book.pdf [cited 2015-04-12].

[LJMS98] Martin Lampe, Glenn Joyce, Wallace M. Manheimer, and Steven P. Slinker. Quasi–neutral particle simulation of magnetized plasma discharges: General formalism and application to ECR discharges. *IEEE Transactions on Plasma Science*, 26(6):1592–1609, December 1998. doi:10.1109/27.747877.

[LL05] Michael A. Lieberman and Allan J. Lichtenberg. *Principles of plasma discharges and materials processing*. Wiley–Interscience, New Jersey, second edition, 2005. doi:10.1002/0471724254.

[Mat94] Alan P. Matthews. Current advance method and cyclic leapfrog for 2D multispecies hybrid plasma simulations. *Journal of Computational Physics*, 112(1):102–116, May 1994. doi:10.1006/jcph.1994.1084.

[Mey98] Hendrik Meyer. *Analyse der Plasmarotation in einer linearen Magnetfeldkonfiguration*. PhD thesis, Humboldt–Universität zu Berlin, 1998. URL: http://edoc.mpg.de/668807 [cited 2015-04-12].

[NFM98] D. Naujoks, G. Fussmann, and H. Meyer. I(U)–characteristics of the plasma generator PSI–1: Experiment and theory. *Contributions to Plasma Physics*, 38(S1):127–133, 1998. doi:10.1002/ctpp.19980380125.

[PSI] Plasma–wall interaction in linear plasma devices — new challenges. URL: http://www.fz-juelich.de/iek/iek-4/EN/Research/02_Linear_plasma_devices/_node.html [cited 2015-04-12].

[Rie91] Karl-Ulrich Riemann. The Bohm criterion and sheath formation. *Journal of Physics D: Applied Physics*, 24(4):493–518, April 1991. doi:10.1088/0022-3727/24/4/001.

[Rie94] Karl-Ulrich Riemann. Theory of the collisional presheath in an oblique magnetic field. *Physics of Plasmas*, 1(3):552–558, March 1994. doi:10.1063/1.870800.

[Rin10] Horst Rinne. *Location–scale distributions: Linear estimation and probability plotting using Matlab*. Justus–Liebig–Universität Giessen, 2010. URL: http://geb.uni-giessen.de/geb/volltexte/2010/7607/ [cited 2015-04-12].

[Yee66] Kane Yee. Numerical solution of initial boundary value problems involving Maxwell's equations in isotropic media. *IEEE Transactions on Antennas and Propagation*, 14(3):302–307, May 1966. doi:10.1109/TAP.1966.1138693.